

Ultrafast quantum dynamics of doped superfluid helium nano-droplets

François Coppens

February 2018

Acknowledgements

We would like to thank Antonio Muñoz, Jordi Ortín, Humphrey Maris and Andrey Vilesov for useful discussions and exchanges. We would also like to thank Nicolas Renon and Emmanuel Courcelle of CALMIP who greatly improved the performance of our code. This work has been performed under Grants No. FIS2014-52285-C2-1-P from DGI, Spain, and 2014SGR401 from Generalitat de Catalunya. Manuel Barranco thanks the Université Fédérale Toulouse Midi-Pyrénées for financial support through the “Chaires d’Attractivité 2014” Programme IMDYNHE. The dynamic simulations presented in this work have been carried out thanks to the HPC resources of CALMIP supercomputing center (Grant P1039).

Contents

Title page	i
Acknowledgements	iii
Contents	v
List of Publications	vii
1 Introduction	1
1.1 A brief history of superfluidity	1
1.2 Some key concepts	4
1.2.1 Bose-Einstein condensation and long-range order . .	4
1.2.2 Bogolyubov's approximation and the order parameter	6
1.2.3 Landau's criterion for superfluidity	8
1.2.4 Rotation and vorticity in superfluids	10
1.3 Helium droplets	12
2 The DFT method for heavy impurities	17
2.1 The Kohn-Sham approach	18
2.1.1 Time-dependent DFT	20
2.2 The Orsay-Trento Density Functional	21
2.2.1 The Solid-OT Density Functional	23
2.3 Static calculations	24
2.3.1 Producing vortical states	25
2.4 Dynamic calculations	26
2.4.1 The DIM model	26
2.4.2 Including spin-orbit coupling	28
I Photo-excitation dynamics of alkalis	33
3 Alkali-doped nanodroplets	35

3.1	Experimental setup	36
4	Results	39
4.1	Imaging Excited-State Dynamics	39
4.2	Desorption dynamics of RbHe exciplexes	47
4.3	Supervised work: potassium-doped nanodroplets	61
II	Head-on collisions and capture by quantised vortices	63
5	Quantised vortices in droplets	65
6	Head-on collisions of Xe and Cs	69
6.1	Introduction	69
6.2	Results	70
7	Capture by quantised vortices	77
7.1	Introduction	77
7.2	Results	79
7.2.1	Xe capture by vortex-free droplets	79
7.2.2	Helium droplets hosting vortex lines	86
7.2.3	Dynamics of Xe and Ar capture by vortex lines	89
7.2.4	Vortex arrays in ${}^4\text{He}$ droplets doped with Ar atoms .	92
8	Conclusions & Outlook	105
8.1	Head-on collisions	105
8.2	Capture	105
A	Angular velocity and angular momentum	107
	Bibliography	111

List of Publications

M. Martinez, Master's thesis, Université Toulouse III Paul Sabatier (2017), URL https://github.com/bcntls2016/M2Report-M_Martinez/blob/master/report/report.pdf.

F. Coppens, A. Leal, M. Barranco, N. Halberstadt, and M. Pi, Journal of Low Temperature Physics **187**, 439 (2017), ISSN 1573-7357, <https://doi.org/10.1007/s10909-016-1690-x>, URL <https://doi.org/10.1007/s10909-016-1690-x>.

F. Coppens, F. Ancilotto, M. Barranco, N. Halberstadt, and M. Pi, Phys. Chem. Chem. Phys. **19**, 24805 (2017), URL <http://dx.doi.org/10.1039/C7CP03307A>.

J. von Vangerow, F. Coppens, A. Leal, M. Pi, M. Barranco, N. Halberstadt, F. Stienkemeier, and M. Mudrich, The Journal of Physical Chemistry Letters **8**, 307 (2017), pMID: 27996261, <http://dx.doi.org/10.1021/acs.jpclett.6b02598>, URL <http://dx.doi.org/10.1021/acs.jpclett.6b02598>.

F. Ancilotto, M. Barranco, F. Coppens, J. Eloranta, N. Halberstadt, A. Hernando, D. Mateo, and M. Pi, International Reviews in Physical Chemistry **36**, 621 (2017), <http://dx.doi.org/10.1080/0144235X.2017.1351672>, URL <http://dx.doi.org/10.1080/0144235X.2017.1351672>.

F. Coppens, J. von Vangerow, M. Barranco, N. Halberstadt, F. Stienkemeier, M. Pi, and M. Mudrich, Phys. Chem. Chem. Phys. pp. – (2018), URL <http://dx.doi.org/10.1039/C8CP00482J>.

Chapter 1

Introduction

Superfluids are liquids and gases with remarkable properties. In particular, superfluid helium can flow through a capillary without friction due to its extremely small viscosity (at least 1500 times smaller than normal liquid helium^[1]), or creep up the wall of a container, seemingly defying the force of gravity^[2] ("Rollin creeping"). Its thermal conductivity is about 3×10^6 times higher than that of liquid helium I or about 200 times higher than that of copper at room temperature^[3]. It therefore earned the title of "best heat conducting substance we know" by Willem and his daughter Anna Keesom and dubbed "*supra-heat-conducting*"^[3]. Later it was understood why^[4-7] and it turns out that heat doesn't diffuse through the medium as in normal liquids, but rather it travels through the medium in waves (second sound). This makes it an ideal coolant e.g. to stabilise the superconducting magnets in CERN's Large Hadron Collider^[8]. Helium is also the only known substance that stays liquid at zero temperature and low pressures and both its angular momentum and vorticity are quantised, making it the first observed macroscopic quantum substance. Helium-4 becomes superfluid below the λ -point, named so by William H. Keesom in 1936 who measured a singularity in the specific heat at $T_\lambda = 2.2\text{ K}$ ^[3].

1.1 A brief history of superfluidity

HELIUM was the last gas to be liquefied and was done so by Heike Kamerlingh Onnes in 1908^[11,12]. In 1932 John McLennan saw that liquid helium stopped boiling below $\approx 2.2\text{ K}$ ^[13] and later that year Willem Keesom and his daughter Anna observed, while measuring the temperature dependence of the specific heat, a singularity around the same temperature^[9]. They called it the " λ -temperature", T_λ , because of the

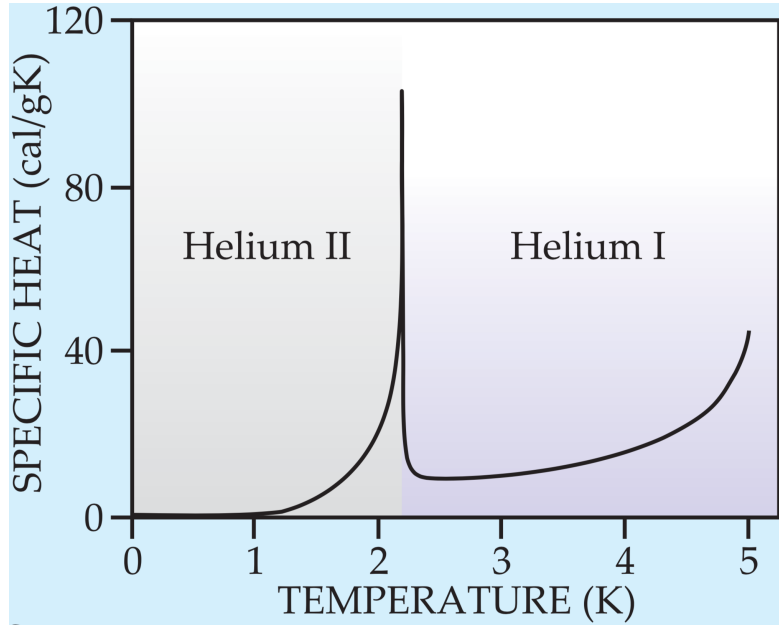


Figure 1.1: The specific heat of ${}^4\text{He}$ as a function of the temperature. There is a clearly visible singularity around 2.2 K and the graph itself has the distinct λ -like shape that inspired^[9] Willem and Anna Keesom to call the temperature at which the singularity occurs the “ λ -point”. (Illustration courtesy of R.J. Donnelly^[10])

shape of the temperature dependence of the specific heat resembling the Greek letter λ (see Figure 1.1). A few years later in 1935 Burton measured a sharp decrease in the viscosity of liquid helium below T_λ ^[14]. Around the same time Fritz London was already thinking about macroscopic wave functions and why helium does not freeze at $T = 0\text{ K}$ under atmospheric pressure^[15]. London and Simon concluded that it was caused by the zero point motion of the helium atoms and their associated kinetic energy that is comparable to their Van der Waals energy, effectively preventing liquid helium to solidify^[16,17]. The year after, in 1936, Willem and Anna Keesom measured an abnormally high heat conductance below T_λ ^[3]. This was confirmed roughly one year later by J.F. Allen *et al.*^[18] and it was understood that the high thermal conductance was the reason for the helium to stop boiling whenever the temperature drops below T_λ . It was in 1937, when Kapitza tried to determine the viscosity of the laminar flow, that he measured a viscosity that was about 10^4 times smaller than that of hydrogen gas^[1]. It was then that Kaptiza who, by analogy with superconductors, first

coined the word “superfluid”^[1] to describe the special state that helium enters below the λ -point where it can flow, seemingly without friction. Allen and Misener realised that superfluid helium is not just a liquid with a very low viscosity, but that its hydrodynamics was completely different from that of ordinary liquids^[19] and therefore required a completely new interpretation.

The start of this new interpretation was made by London^[20] in 1938 when he made a connection between the behaviour of superfluid helium and that of an ideal “Bose-Einstein” (BE) gas. Both his calculated value for $T_c = 3.09\text{ K}$ and the behaviour of the temperature dependence of the heat capacity for the ideal BE-gas were very similar to the measured ones for liquid helium below T_λ . He wrote to Nature that “it was difficult not to imagine a connection with “Bose-Einstein condensation” (BEC). Tisza expanded upon London’s ideas^[21] and considered a Helium II system of total N atoms to consist of two parts; a macroscopic “condensed” part n_0 , the superfluid component, in the ground state, and the remaining part $n = N - n_0$, the normal component, where the helium atoms are distributed over the excited states. Assuming this was correct the fraction n_0/N should decrease with increasing temperature according to the equation

$$\frac{n_0}{N} = 1 - \left(\frac{T}{T_0} \right)^s \quad \text{for } T < T_0 \quad (1.1)$$

where $s = 3/2$ for an ideal gas and should be taken larger, e.g. $s = 5$, for a real liquid with stronger interactions between the atoms.

This was the birth of the “two-fluid” model. With this model he derived two hydrodynamic equations for liquid helium below T_λ and discovered that within it, heat propagates in waves instead of diffusing through the medium, and calculated the velocity of these waves. He also explained why the viscosity is disappearing at low temperatures contrary to classical liquids where the viscosity increases^[4–7]. In 1941 Lev Landau reformulated Tisza’s theory on a more rigorous footing^[22,23]. He assumed, contrary to Tisza, that the normal component of the liquid was made-up of collective excitations instead of excited single atoms. He postulated that the liquid could exhibit two states of motion which he called “potential motion” that is irrotational ($\nabla \times \mathbf{v} = 0$), and “vortex motion” that is rotational ($\nabla \times \mathbf{v} \neq 0$). The corresponding energies of these two motions are discontinuously separated by an energy gap Δ . In case of potential internal motion the excitations are quanta of longitudinal (sound) waves, i.e., phonons. The

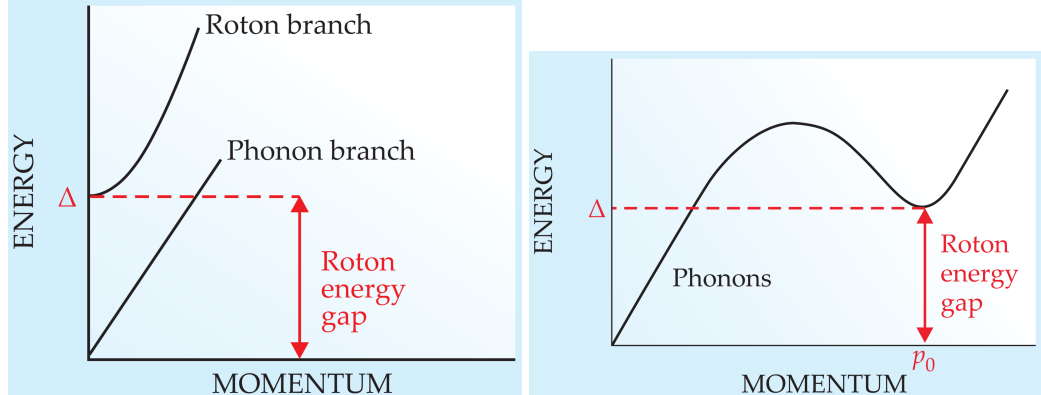


Figure 1.2: Left: Lev Landau’s 1941 energy dispersion curve^[22] for the excitations in liquid helium below T_λ . It exhibits a phonon- and a roton branch. The slope of the linear phonon branch corresponds to the velocity of sound. Right: Lev Landau’s 1947 modified dispersion curve. The roton-branch is no longer a separate excitation branch but rather an extension of the phonon-branch. (Illustration courtesy of R.J. Donnelly^[10])

excitations of the vortex-spectrum could be called “rotons” (see Figure 1.2).

A theoretical demonstration, explicitly showing that phonons and rottons are collective excitations of the liquid, came in the form of a 1947 paper by Nikolay Bogolyubov^[24]. The intimate relationship between superfluidity and BEC was not universally accepted until 1995 when Cornell and Wieman in Colorado and Ketterle at MIT discovered BEC in rubidium quantum gases^[25,26].

1.2 Some key concepts

In this section I will briefly introduce some key ideas that are used throughout the thesis and that are needed to fully appreciate the discussed material. Also references to more complete and more in-depth treatments will be provided for the interested reader.

1.2.1 Bose-Einstein condensation and long-range order

The essential concept of Bose-Einstein (BE) condensation is the fact that at low temperatures, multiple bosons, unlike fermions, will occupy the same

quantum state. In theory there is no upper bound of how many bosons can occupy such a single state. It is then said that, with ever decreasing temperature, a macroscopic part of the total number of bosons will “condense” into the quantum state with the lowest energy.

Another important concept in BEC is the idea of long-range order. Let us start by introducing the one-body density matrix of a system of N bosons in a pure state $\Psi_k(\mathbf{r}_1, \mathbf{r}_2, \dots, \mathbf{r}_N)$

$$n_k^{(1)}(\mathbf{r}, \mathbf{r}') := N \int \Psi_k^*(\mathbf{r}, \mathbf{r}_2, \dots, \mathbf{r}_N) \Psi_k(\mathbf{r}', \mathbf{r}_2, \dots, \mathbf{r}_N) d\mathbf{r}_2 d\mathbf{r}_3 \dots d\mathbf{r}_N \quad (1.2)$$

where the integral is taken over the $N - 1$ coordinates $\mathbf{r}_2, \mathbf{r}_3, \dots, \mathbf{r}_N$. For a statistical mixture of quantum states one needs to take the weighted average over all the different Ψ_k -states. In thermodynamic equilibrium the states are Boltzmann weighted by their eigenvalues $\{E_k\}$

$$n^{(1)}(\mathbf{r}, \mathbf{r}') = \frac{1}{Q} \sum_k n_k^{(1)}(\mathbf{r}, \mathbf{r}') e^{-E_k/k_B T} \quad (1.3)$$

where Q is the partition function. For more general cases the one-body density matrix is defined

$$n^{(1)}(\mathbf{r}, \mathbf{r}') := \langle \hat{\Psi}^\dagger(\mathbf{r}) \hat{\Psi}(\mathbf{r}') \rangle \quad (1.4)$$

where $\hat{\Psi}^\dagger(\mathbf{r})/\hat{\Psi}(\mathbf{r})$ are field-operators creating/annihilating a boson at \mathbf{r} and the averaging $\langle \dots \rangle$ is taken over all states in the mixture. Once it is accepted that a macroscopic part of the total number of bosons can occupy a single quantum state it can be demonstrated that, while considering a uniform isotropic system of N bosons, the one-body density matrix (Eq. 1.2) tends to a constant value when the distance between \mathbf{r} and \mathbf{r}' goes to infinity. In the thermodynamic limit where $N, V \rightarrow \infty$ such that $n = N/V$ is kept fixed, the one-body density only depends on the modulus of the relative variable $\mathbf{s} := \mathbf{r} - \mathbf{r}'$ so that we can write it as the Fourier transform of the momentum distribution as

$$n^{(1)}(s) = \frac{1}{V} \int n^{(1)}(\mathbf{p}) \exp(i\mathbf{p} \cdot \mathbf{s}/\hbar) d\mathbf{p} \quad (1.5)$$

For a BEC system, the momentum distribution at small momenta is not smooth but has a sharp peak around $p = 0$ for the bosons that are in the ground state, while the remaining bosons are smoothly distributed over the excited states.

$$n(\mathbf{p}) = N_0 \delta(\mathbf{p}) + \tilde{n}(\mathbf{p}) \quad (1.6)$$

where \tilde{n} is a smoothly varying function of \mathbf{p} . When this expression is plugged into Eq. (1.5) and taking the limit where s goes to infinity

$$\lim_{s \rightarrow \infty} n^{(1)}(s) = \frac{N_0}{V}, \quad (1.7)$$

where $N_0/V := n_0 \leq 1$ is called the condensate fraction. It is called long-range order since it involves the off-diagonal elements of the one-body density matrix; the elements that are usually associated with the coherences.

A set of eigenvalues $\{n_i\}$ of the one-body density matrix can be defined through the following eigenvalue equation

$$\int n^{(1)}(\mathbf{r}, \mathbf{r}') \varphi_i(\mathbf{r}') d\mathbf{r}' = n_i \varphi_i(\mathbf{r}) \quad (1.8)$$

and its solutions $\{\varphi_i\}$ form a natural orthonormal basis set of single boson wave functions $\int \varphi_i^* \varphi_j d\mathbf{r} = \delta_{ij}$, with normalisation condition $\sum_i n_i = N$. This permits writing the one-body density matrix in a useful diagonalised form and recalling that BEC occurs when a single particle state φ_i is occupied in a macroscopic way, say when $n_{i=0} = N_0$, a number of order N , we separate the condensate part from the rest

$$n^{(1)}(\mathbf{r}, \mathbf{r}') = N_0 \varphi_0^*(\mathbf{r}) \varphi_0(\mathbf{r}') + \sum_{i \neq 0} n_i \varphi_i^*(\mathbf{r}) \varphi_i(\mathbf{r}') \quad (1.9)$$

1.2.2 Bogolyubov's approximation and the order parameter

It is customary, given the importance of the condensate fraction N_0 in a BEC, to write the field operator of a N -body boson system as the sum of the condensate part and the rest, just as the one-body density matrix

$$\hat{\Psi}(\mathbf{r}) = \varphi_0(\mathbf{r}) \hat{a}_0 + \sum_{i \neq 0} \varphi_i(\mathbf{r}) \hat{a}_i \quad (1.10)$$

where the \hat{a}_i and \hat{a}_j^\dagger are annihilation and creation operator of a particle in state φ_i and obey the usual bosonic commutation relations

$$[\hat{a}_i, \hat{a}_j^\dagger] = \delta_{ij}, \quad [\hat{a}_i, \hat{a}_j] = 0 = [\hat{a}_i^\dagger, \hat{a}_j^\dagger] \quad (1.11)$$

Using Eq. (1.10) in Eq. (1.2) and comparing it to Eq. (1.9) one finds the expectation value of $\langle \hat{a}_j^\dagger \hat{a}_i \rangle = \delta_{ij} n_i$. Now, the Bogolyubov approximation

essentially replaces the operators \hat{a}_0 and \hat{a}_0^\dagger with the *c*-number¹ $\sqrt{N_0}$. This is equivalent to ignoring the non-commutative nature of the operators due to the macroscopic occupation of the state φ_0 , when $N_0 = \langle \hat{a}_0^\dagger \hat{a}_0 \rangle \gg 1$. We then rewrite the field operator as the sum of a classical field for the condensed component and quantum field for the non-condensed component

$$\hat{\Psi}(\mathbf{r}) = \Psi_0(\mathbf{r}) + \delta\hat{\Psi}(\mathbf{r}), \quad (1.12)$$

where $\delta\hat{\Psi}(\mathbf{r}) = \sum_{i \neq 0} \varphi_i(\mathbf{r}) \hat{a}_i$ and $\Psi_0(\mathbf{r}) = \sqrt{N_0} \varphi_0(\mathbf{r})$. At $T = 0$ the whole system is condensed and one can ignore $\delta\hat{\Psi}$ altogether; the field operator becomes a normal function of space Ψ_0 .

The classical field Ψ_0 is called the *effective-* or *macroscopic* wave function of the condensate and it behaves like an order parameter in the sense that it varies continuously between a maximum value \sqrt{N} , that is proportional to the total number particles in the system, at $T = 0$, and vanishes at the superfluid-normal fluid phase transition temperature T_λ . It is a complex quantity characterised by a real-valued modulus and phase S :

$$\Psi_0(\mathbf{r}) = \left| \sqrt{N_0} \varphi_0(\mathbf{r}) \right| e^{iS(\mathbf{r})} \quad (1.13)$$

The modulus determines the number-density of the condensate, while the phase S plays an important role in the coherence and properties of the superfluid. As we will see in Section 1.2.4, S plays the role of a velocity potential.

Using an order parameter as defined here is equivalent to using the many-body wave function

$$\Phi(\mathbf{r}_1, \mathbf{r}_2, \dots, \mathbf{r}_N) = \prod_{i=1}^N \varphi_0(\mathbf{r}_i), \quad (1.14)$$

with a density operator $\hat{\rho}(\mathbf{r}) := \sum_{i=1}^N \delta(\mathbf{r} - \mathbf{r}_i)$ (see Section 2). One way to see why this wave function plays the role of an order parameter is to look at its time dependence. For normal wave functions the time dependence is determined by the eigenvalues E_i of the Hamiltonian of the system

$$\Psi(\mathbf{r}, t) = \psi(\mathbf{r}) e^{-iE_i t/\hbar} \quad (1.15)$$

¹The term *c*-number is old nomenclature for a classical number, which can be real or complex, to distinguish them from quantum numbers, or *q*-numbers, that are represented by operators.

But in this case, the time dependence is determined by the chemical potential $\mu = E(N) - E(N-1) \approx \partial E / \partial N$

$$\Psi_0(\mathbf{r}, t) = \Psi_0(\mathbf{r}) e^{-i\mu t/\hbar} \quad (1.16)$$

Another aspect of Ψ_0 being an order parameter and not a true many-body wave function is that two solutions Ψ_a and Ψ_b of the non-linear droplet Hamiltonian corresponding to two different values of the chemical potential μ_a and μ_b are not necessarily orthogonal, i.e. $0 \leq N^{-1} \int \Psi_a^* \Psi_b d\mathbf{r} < 1$. However, in dilute gases it is possible to construct a many-body wave function from the order parameter that regains its orthonormality in the thermodynamic limit

$$\Phi_0(\mathbf{r}_1, \mathbf{r}_2, \dots, \mathbf{r}_N) = \left(\frac{1}{\sqrt{N}} \Psi_0(\mathbf{r}_1) \right) \left(\frac{1}{\sqrt{N}} \Psi_0(\mathbf{r}_2) \right) \cdots \left(\frac{1}{\sqrt{N}} \Psi_0(\mathbf{r}_N) \right) \quad (1.17)$$

1.2.3 Landau's criterion for superfluidity

For a gas or liquid to be able to become superfluid Landau postulated that the energy dispersion relation needs to fulfil certain requirements. Specifically for a fluid to flow without dissipation, i.e. a super-flow, the velocity field needs to fulfil the following inequality:

$$v < v_c = \min_{\mathbf{p}} \frac{\epsilon(\mathbf{p})}{p} \quad (1.18)$$

For an ideal Bose gas $\epsilon(\mathbf{p}) = \frac{p^2}{2m}$. In this case

$$v_c = \min_{\mathbf{p}} \frac{\epsilon(\mathbf{p})}{p} \quad (1.19)$$

$$= \min_{\mathbf{p}} \frac{p}{2m} \quad (1.20)$$

$$= 0 \quad (1.21)$$

Apparently ideal Bose-gases cannot become superfluid.

But if we allow for some weak interactions between the bosons the energy dispersion relation is given by

$$\epsilon(\mathbf{p}) = \sqrt{\frac{gn}{m} p^2 + \left(\frac{p^2}{2m} \right)^2}, \quad (1.22)$$

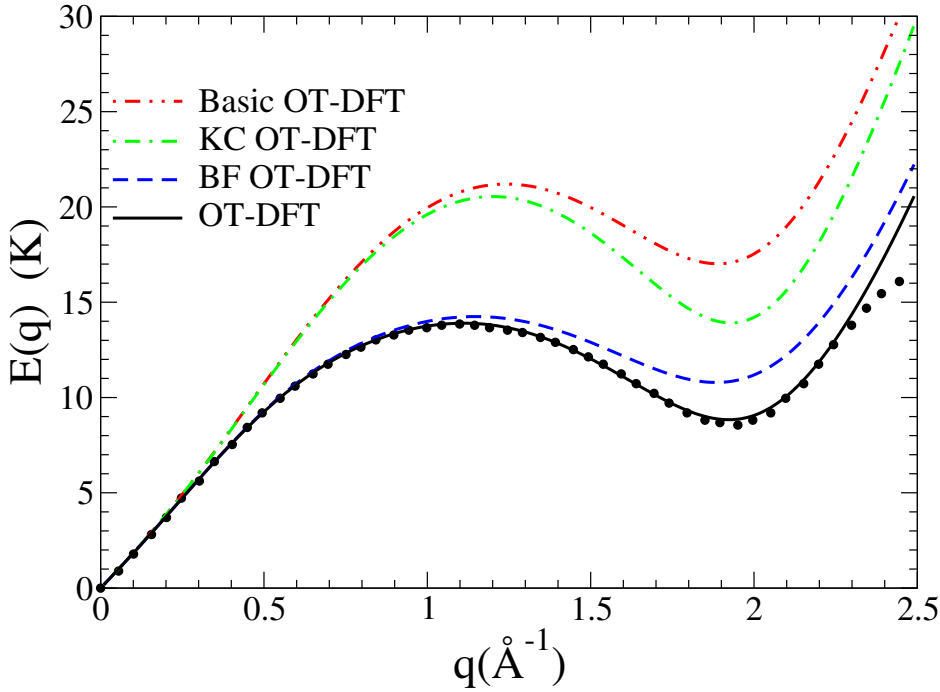


Figure 1.3: Dispersion relation for elementary excitations in liquid ${}^4\text{He}$ calculated as in^[27]. ‘Basic’ indicates the OT-DFT without the non-local kinetic energy correlation (KC) nor the back-flow (BF) terms; KC OT-DFT adds to the basic OT-DFT the KC term; BF OT-DFT adds to the basic OT-DFT the BF term. The dots are the experimental data from^[28]. The Landau velocity $v_L = E(q)/(\hbar q)|_{min}$ obtained for each functional is 60.3 m/s (OT-DFT); 75.1 m/s (BF OT-DFT); 94.4 m/s (KC OT-DFT); 118 m/s (basic OT-DFT); and 57.5 (experiment).

Bogolyubov’s dispersion law for elementary excitations (1947). And thus

$$v_c = \min_p \sqrt{\frac{gn}{m} + \frac{p^2}{4m^2}} \quad (1.23)$$

$$= \sqrt{\frac{gn}{m}} \quad (1.24)$$

$$= c, \quad (1.25)$$

the speed of sound. Here $g = \frac{4\pi\hbar^2 a}{m}$, and a the s -wave scattering length. The weakly interacting Bose gases can become superfluid.

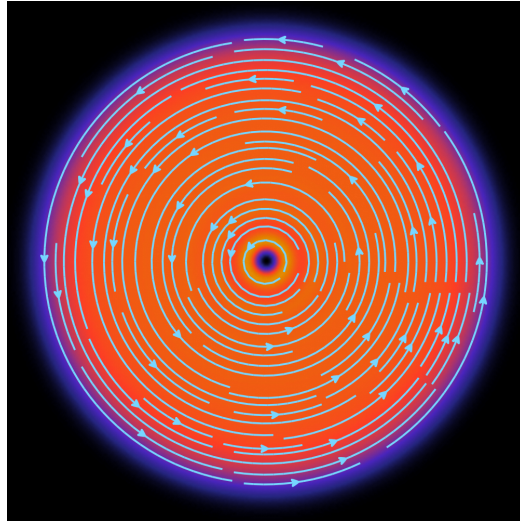


Figure 1.4: Cross section of a ${}^4\text{He}$ droplet through a symmetry plane. The droplet is made of 1000 atoms. Superimposed in cyan are the streamlines of the velocity field \mathbf{v}_s for $s = 1$. They are concentric circles, centred around the vortex core along the z -axis. The colour scale encodes for the density $\rho(r)$. The radius of the droplet is about 22 Å.

Liquid helium below the λ -point has a similar energy dispersion relation (see Figure 1.3) hence reinforcing the notion that superfluidity and Bose–Einstein condensation are two intimately related concepts. The experimental value of the speed of sound is ~ 57.5 m/s.

1.2.4 Rotation and vorticity in superfluids

Starting from time-dependent Euler-Lagrange (EL) equation (Eq. 2.12, see Chapter 2) for the time-evolution of the order parameter Ψ (Eq. 1.13, dropping the ground-state subscript and allowing φ and S to vary in time)

$$i\hbar \frac{\partial}{\partial t} \Psi(\mathbf{r}, t) = \left[-\frac{\hbar^2}{2m} \nabla^2 + \frac{\delta \mathcal{E}_c}{\delta \rho} \right] \Psi(\mathbf{r}, t) \quad (1.26)$$

one left-multiplies it with the complex conjugate of the order parameter Ψ^* and then subtract the complex conjugate of the whole expression on both sides. After some algebra and defining $\rho(\mathbf{r}, t) := N|\varphi(\mathbf{r}, t)|^2$, one arrives at

the continuity equation

$$\frac{\partial \rho}{\partial t} + \nabla \cdot \mathbf{j} = 0, \quad (1.27)$$

with

$$\mathbf{j}(\mathbf{r}, t) := -\frac{i\hbar}{2m} [\Psi^*(\mathbf{r}, t) \nabla \Psi(\mathbf{r}, t) - \Psi(\mathbf{r}, t) \nabla \Psi^*(\mathbf{r}, t)] \quad (1.28)$$

$$= \rho(\mathbf{r}, t) \frac{\hbar}{m} \nabla S(\mathbf{r}, t) \quad (1.29)$$

From Eq. (1.27) it follows that the atomic number density is a conserved quantity.

We can identify the collective velocity \mathbf{v}_s of the superfluid through the relation

$$\mathbf{v}_s(\mathbf{r}, t) = \mathbf{j}/\rho = \frac{\hbar}{m} \nabla S(\mathbf{r}, t) \quad (1.30)$$

and we see that the rotation of the velocity field of the superfluid $\nabla \times \mathbf{v}_s = 0$, i.e. the fluid is said to be *irrotational*; a typical property of superfluids. Conversely, taking the curl $\nabla \times \mathbf{j} = \frac{\hbar}{m} \nabla \rho \times \nabla S$ we see that this is merely a restatement of the fact that one needs a gas or liquid with a non-uniform density and a non-zero phase for it to be able to support vortices.

Let us consider the illustrative example of a line vortex through the origin along the z -axis. As will be demonstrated in Section 2.3.1, this is a stationary state of the droplet Hamiltonian and therefore its time dependence is just a multiplicative factor. In cylindrical coordinates (r, φ, z) such a vortex solution has the form

$$\Psi_s(\mathbf{r}) = \sqrt{\rho(r)} e^{is\varphi}, \quad (1.31)$$

with s an integer. This is an eigenfunction of the angular momentum operator \hat{L}_z with eigenvalue

$$\hat{L}_z \Psi_s(\mathbf{r}) = \frac{\hbar}{i} \frac{\partial}{\partial \varphi} \Psi_s(\mathbf{r}) = \hbar s \Psi_s(\mathbf{r}) \quad (1.32)$$

and with expectation value

$$\langle \hat{L}_z \rangle = \langle \Psi_s | \hat{L}_z | \Psi_s \rangle \quad (1.33)$$

$$= \hbar s \left\langle \sqrt{N_0} \varphi_0 \middle| \sqrt{N_0} \varphi_0 \right\rangle \quad (1.34)$$

$$= N_0 \hbar s \quad (1.35)$$

The angular momentum is quantised and proportional to the number of bosons in the BEC fraction/superfluid. We can calculate the velocity field

$$\mathbf{v}_s = \frac{\hbar}{m} \nabla S = \frac{\hbar s}{m r} \hat{\phi} \quad (1.36)$$

The streamlines of \mathbf{v}_s are concentric circles, centred around the z -axis, lying in the xy -plane (see Figure 1.4). Contrary to rigid rotation fields which increase proportional to the distance from the z -axis r , the superfluid rotation field decreases proportional to distance from the z -axis $1/r$ and is singular in the origin. Calculating the circulation of the velocity field \mathbf{v}_s along a closed contour including the z -axis gives

$$\oint_{\partial\Sigma} \mathbf{v}_s \cdot d\mathbf{l} = \int_0^{2\pi} \frac{\hbar s}{m r} \hat{\phi} \cdot r d\varphi \hat{\phi} \quad (1.37)$$

$$= 2\pi s \frac{\hbar}{m} \quad (1.38)$$

There are two things to note here. Firstly, the circulation around a closed loop that encompasses the z -axis is quantised in units of \hbar/m for $s \in \mathbb{N}_{>0}$. Secondly, the value of the circulation of the velocity field does not depend on the chosen contour as long as it includes the location of the vortex. This means that all the vorticity is contained at the location where the velocity field is singular (the “core” of the vortex), at $r = 0$ along the z -axis.

Because of the pole in the velocity field, Stokes theorem will lead to the following contradiction

$$2\pi s \frac{\hbar}{m} = \oint_{\partial\Sigma} \mathbf{v}_s \cdot d\mathbf{l} = \iint_{\Sigma} \nabla \times \mathbf{v}_s \cdot d\Sigma = 0 \quad (1.39)$$

and can therefore not be applied. To emphasise that all the vorticity is concentrated around the vortex core one can write formally

$$\nabla \times \mathbf{v}_s = 2\pi s \frac{\hbar}{m} \delta^{(2)}(\mathbf{r}_\perp) \hat{\mathbf{z}}, \quad (1.40)$$

where $\delta^{(2)}$ is 2-dimensional Dirac-delta function and \mathbf{r}_\perp a vector in a plane perpendicular to the vortex line.

1.3 Helium droplets

UNTIL the 1980, most experimental and theoretical work was done on bulk systems, i.e. systems of the order of N_A number of atoms.

It was only in the last couple of decades that advancements in technology enabled experimentalists to create nanoscale sized superfluid helium droplets. From the early 1990's onwards, superfluid helium nano-droplets became an active field of study, both experimentally and theoretically.

Finite size effects Helium nanodroplets are considered ideal model systems to explore quantum hydrodynamics in self-contained, isolated superfluids. The main focus has been on the evolution of their properties with the number of atoms in the cluster, until the condensed matter limit is reached. Helium clusters are especially interesting in that quantum effects play a key role in determining their properties. In particular, given that a helium cluster is an ensemble of bosons at about 0.4 K [1, 2], manifestations of collective behaviour (such as superfluidity) are expected. On the other hand, it is not yet clear how the finite size of a cluster affects this non-classical (or degenerate) collective behaviour.

Non-classical ideas to explain, for example the capture of Cs atoms by large helium clusters, were introduced as early as 1986 [3], while recently, Toennies et al. [4] have measured the electronic spectrum of glyoxal molecules embedded in He clusters and found it consistent with a theoretical simulation computed using the phonon dispersion curve of superfluid bulk He II. The authors themselves, however, point out that at the average cluster size of 5500 He atoms reported in [4], the phonon dispersion curve is well in the bulk limit (see also [5, 6]); it is therefore not surprising that they find results consistent with the bulk case, especially for a molecule readily solvated inside the cluster, for which surface effects play a minor role. Therefore the influence on superfluidity of the He clusters size has not been detected so far.

Properties of He droplets are difficult to determine The helium-helium interaction is already weak in bulk liquid helium and in finite self-bound systems such as droplets it is even weaker, e.g. the binding energy per atom is < 7.17 K. Because of this helium droplets cool down very rapidly due to fast evaporation and therefore reaching their limiting temperature of about 0.38 K in microseconds. Pure helium droplets are neutral systems and their properties like their size, binding energy and excitation spectra, are not easy to determine experimentally and are usually obtained by indirect methods. This didn't stop the theoreticians describe doped ${}^4\text{He}_N$ droplets using a wide variety of approaches depending on

the size and character of the droplets ranging from Quantum Monte Carlo, Hypernetted-Chain/Euler-Lagrange, Variational Monte Carlo and many others.

He droplets will pickup any dopant A key property of helium droplets, in contrast to bulk helium, is their ability to pickup any kind of dopants with which they collide. Depending on the strength of the dopant-⁴He interaction and the surface tension of the droplet, a dimensionless parameter λ can be defined^[29] with a critical value $\lambda_0 \sim 1.9$. Below λ_0 impurities are bound to the surface of the droplet (e.g. the alkalies), and above get solvated into the droplet's interior. They can therefore be doped with almost any kind of atomic- or molecular species where they can form new complexes.

This enables a broad spectrum of possible experimental study. Due to the fact that helium droplets are ultra cold superfluid liquids, and therefore provide high mobility of any picked-up dopants, one can do high resolution spectroscopy studies. Having a fine control over the number of picked-up dopants[29] one can use droplets as a matrix for creating self-organising structures of polar molecules, or very cold metal clusters and study their Coulomb explosion.

From the perspective of the droplet it's possible to use the dopants as gentle probes to determine the superfluid properties of helium droplets that would be inaccessible with other methods. For two examples of this see [37-39], where a dopant is used to probe the superfluid character of small ⁴He droplets and [16,17] to see their limiting temperatures.

Quantised vortices in He droplets One of the most intriguing properties of superfluid helium droplets is the fact that they can host quantised vortices. Because of their ultra low temperature they are true quantum liquids and their vorticity and angular momentum are quantised. The existence of quantised vortices was anticipated because they have been created and observed in BECs made of dilute gases. However, the detection of quantised vortices is still experimentally challenging.

The last few decades A lot of work has been done on helium droplets the last few decades, both experimentally and theoretically. From the absorption spectra of alkali metal doped helium droplets, the study of

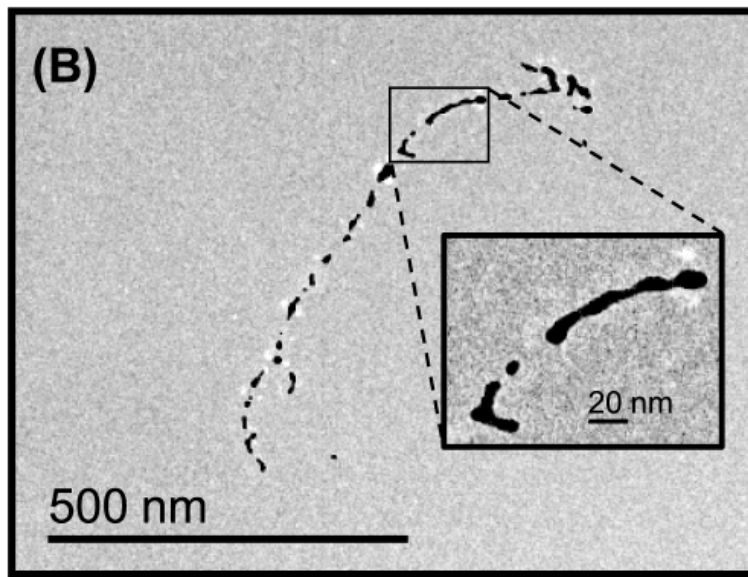


Figure 1.5: Electron-microscope image of an elongated track-shaped Ag-cluster after it is surface-deposited.

doped mixed ^3He - ^4He droplets, electrons in liquid helium, to the investigation of the critical Landau velocity inside small ^4He droplet. For a comprehensive overview of work done in the last two decades, the interested reader is referred to the review papers[JLTP.Vol142.Nos.1/2(2006), IRPC.Vol36No4.621-707(2017), IRPC.Vol33No3.301-339(2014)].

Chapter 2

The DFT method for heavy impurities

One Functional to rule them all,
One Functional to find them,
One Functional to bring them
all and in a droplet bind them in
the Realm of Physics where
Reason lies.

some guy from LCAR

From the theoretical point of view, superfluid helium must be considered as a high dimensional quantum system. Quantum Monte Carlo (QMC)^[30] and direct quantum mechanical^[31–33] calculations are the most accurate methods, but their computational demand quickly exceeds currently available computer resources when the number of helium atoms increases. Furthermore, QMC cannot describe dynamic evolution of superfluid helium in real time. To address these limitations, semi-empirical methods based on density functional theory (DFT) formalism have been introduced^[34–36]. DFT can be applied to much larger systems than QMC and allows for time-dependent formulation. As such, it offers a good compromise between accuracy and computational feasibility. The main drawback of DFT is that the exact energy functional is not known and must therefore be constructed in a semi-empirical manner. Moreover, doped helium droplets are limited to a mean-field description of the dopant-helium interaction. Nevertheless, DFT is the only method to date that can successfully reproduce results from a wide range of time-resolved experiments in superfluid helium, for realistic sizes compared to experimental conditions.

2.1 The Kohn-Sham approach

THE starting point for the density functional method is the Hohenberg-Kohn (HK) theorem^[37], which states that the ground-state energy E_v of an *interacting inhomogeneous* system in a static potential v can be written in as a unique functional of the one-body density ρ like

$$E_v[\rho] = \int v(\mathbf{r})\rho(\mathbf{r}) \, d\mathbf{r} + F[\rho] \quad (2.1)$$

where $F[\rho]$ is a universal functional—valid for *any* number of particles and *any* external potential v —of the one-body density, defined as

$$\rho(\mathbf{r}) := \langle \Phi | \hat{\rho}(\mathbf{r}) | \Phi \rangle = \left\langle \Phi \left| \sum_{i=1}^N \delta(\mathbf{r} - \mathbf{r}_i) \right| \Phi \right\rangle \quad (2.2)$$

and $\Phi(\mathbf{r}_1, \mathbf{r}_2, \dots, \mathbf{r}_N)$ is the many-body wave function of such a system. Furthermore, the functional $F[\rho]$ gives the ground state energy *if and only if* the input density is the true ground state density of the system.

Kohn and Sham (KS) later reformulated^[38] the theory by introducing an approximation scheme for the functional $F[\rho]$ that is analogous to Hartree's method, but also contains the major part of the correlation effects inherent in interacting many-body systems. The approximation starts by defining

$$F[\rho] := T[\rho] + E_c[\rho] \quad (2.3)$$

where $T[\rho]$ is now the kinetic energy of a fictitious system of *non-interacting* particles with density ρ and $E_c[\rho]$ is the correlation energy of an *interacting* system with the same density. For the kinetic part this allows us to write the total kinetic energy $T[\rho]$ as the sum over the individual kinetic energies T_i of the non-interacting particles

$$T = \sum_i T_i = -\frac{\hbar^2}{2m} \sum_i \langle \varphi_i | \nabla^2 | \varphi_i \rangle = -\frac{\hbar^2}{2m} \sum_i \int \varphi_i^*(\mathbf{r}) \nabla^2 \varphi_i(\mathbf{r}) \, d\mathbf{r}, \quad (2.4)$$

where the $\{\varphi_i\}$ are the Kohn-Sham single-particle orbitals corresponding to the many-body KS wave function $\Phi_{KS}(\mathbf{r}_1, \mathbf{r}_2, \dots, \mathbf{r}_N) = \prod_i \varphi_i(\mathbf{r}_i)$ and leading to the density (using definition Eq. 2.2) $\rho(\mathbf{r}) = \sum_i |\varphi_i(\mathbf{r})|^2$.

There is difference between the true kinetic energy of the interacting system and the fictitious one, due to the negligence of the correlations. This difference is being corrected and accounted for in the correlation energy $E_c[\rho]$.

Because the functional we used in this work is calibrated to produce the correct behaviour of bulk liquid helium at zero temperature $T = 0$ and zero pressure $P = 0$, we assume complete Bose-Einstein (BE) condensation of the helium. In this case all the helium atoms occupy the same single-particle KS-orbital φ_0 . Therefore the many-body wave function and the density simplifies further to

$$\Phi_{BEC}(\mathbf{r}_1, \mathbf{r}_2, \dots, \mathbf{r}_N) = \prod_i \varphi_0(\mathbf{r}_i) \quad (2.5)$$

and

$$\rho(\mathbf{r}) = N |\varphi_0(\mathbf{r})|^2 \quad (2.6)$$

respectively. As explained in Section 1.2.2, it is customary to define an effective wave function

$$\Psi(\mathbf{r}) := \sqrt{\rho(\mathbf{r})} = \sqrt{N} \varphi_0(\mathbf{r}) \quad (2.7)$$

for the condensate (see Eq. 1.12), which is sometimes called a *macroscopic wave function* or *order parameter*. We can now simplify the expression for the kinetic energy (Eq. 2.4)

$$T = -\frac{\hbar^2}{2m} N \int \varphi_0^*(\mathbf{r}) \nabla^2 \varphi_0(\mathbf{r}) d\mathbf{r} = \frac{\hbar^2}{2m} N \int |\nabla \varphi_0|^2 d\mathbf{r}, \quad (2.8)$$

where we used partial integration to get to the last step and imposed that the orbital φ_0 vanishes at the boundaries. With our definition Eq. (2.7) we can now write the kinetic energy as a functional of the density

$$T[\rho] = \frac{\hbar^2}{2m} \int |\nabla \sqrt{\rho}|^2 d\mathbf{r} \quad (2.9)$$

To summarise, we write the complete energy functional E_v as

$$E_v[\rho] = \int v(\mathbf{r}) \rho(\mathbf{r}) d\mathbf{r} + \frac{\hbar^2}{2m} \int |\nabla \sqrt{\rho}|^2 d\mathbf{r} + \int \mathcal{E}_c[\rho] d\mathbf{r} \quad (2.10)$$

where we defined the correlation energy density functional \mathcal{E}_c through

$$E_c[\rho] := \int \mathcal{E}_c[\rho] \, d\mathbf{r}. \quad (2.11)$$

The job now is to find an \mathcal{E}_c such that the desired physical properties of helium can be recovered. This is far from trivial but several of these density functionals are available now. The one used in this work is discussed in the next section.

2.1.1 Time-dependent DFT

To describe the time evolution of the system, the Runge-Gross theorem extends DFT to its time-dependent version TDDFT^[39]. The functional variation of the associated action (see Eq. (2.46) for an example) leads to the following time-dependent Euler-Lagrange (EL) equation

$$i\hbar \frac{\partial}{\partial t} \Psi(\mathbf{r}, t) = \left\{ -\frac{\hbar^2}{2m} \nabla^2 + \frac{\delta \mathcal{E}_c}{\delta \rho} \right\} \Psi(\mathbf{r}, t) := \mathcal{H}[\rho] \Psi(\mathbf{r}, t) \quad (2.12)$$

As long as we are in the thermodynamic regime the solutions $\Psi(\mathbf{r}, t)$ can be decomposed into the liquid density and associated velocity potential field (see Section 1.2.2, 1.2.4).

Considering only eigenstates $\Psi(\mathbf{r}, t) = \Psi_0(\mathbf{r}) e^{-i\mu t/\hbar}$ of the time independent Hamiltonian $\mathcal{H}[\rho]$ the time-dependent EL-equation reduces to a time independent one

$$\left\{ -\frac{\hbar^2}{2m} \nabla^2 + \frac{\delta \mathcal{E}_c}{\delta \rho} \right\} \Psi_0(\mathbf{r}) = \mu \Psi_0(\mathbf{r}) \quad (2.13)$$

with μ the chemical potential. Solving this equation by iteration will result in the ground state density $|\Psi_0|^2$ of the system. Within the HK-framework and the variation principle that was used to obtain these EL-equations, the nature of the minimisation is such that it gives the lowest energy for a given symmetry. This means that as long as the input state does not break the symmetry of the time-independent EL-equation, it minimises the energy of this state even if it does not lead to the ground state. This can be used to obtain a stationary vortex-line solution. With the inclusion of appropriate constraints in the energy functional the same procedure can be used to obtain helium densities with an array of vortex-lines.

Model parameters for the OT-DFT and solid functionals.					
ϵ_{LJ} (K)	σ (\AA)	h (\AA)	c_2 (K \AA ⁶)	c_3 (K \AA ⁹)	α_s (\AA ³)
10.22	2.556	2.190323	-2.41186×10^4	1.85850×10^6	54.31
ρ_{0s} (\AA ⁻³)	l (\AA)	C (Hartree)	β (\AA ³)	ρ_m (\AA ⁻³)	γ_{11}
0.04	1.	0.1	40.	0.37	-19.7544
γ_{12} (\AA ⁻²)	α_1 (\AA ⁻²)	γ_{21}	γ_{22} (\AA ⁻²)	α_2 (\AA ⁻²)	
12.5616	1.023	-0.2395	0.0312	0.14912	

2.2 The Orsay–Trento Density Functional

THE functional that is used in the work presented in this thesis is based on the Orsay-Trento (OT) functional^[40]. It uses a finite-range, non-local approach and it is, to date the most accurate model in the sense that it accurately reproduces bulk properties of liquid helium at $T = 0 = P$, written as

$$\begin{aligned} \mathcal{E}_c[\rho, \mathbf{v}] = & \frac{1}{2} \int \left\{ \rho(\mathbf{r}) V_{LJ}(|\mathbf{r} - \mathbf{r}'|) \rho(\mathbf{r}') \right. \\ & + \frac{1}{2} c_2 \rho(\mathbf{r}) [\bar{\rho}(\mathbf{r})]^2 + \frac{1}{3} c_3 \rho(\mathbf{r}) [\bar{\rho}(\mathbf{r})]^3 \Big\} d\mathbf{r}' \\ & - \frac{\hbar^2}{4m} \alpha_s \int F(|\mathbf{r} - \mathbf{r}'|) \left[1 - \frac{\tilde{\rho}(\mathbf{r})}{\rho_{0s}} \right] \nabla \rho(\mathbf{r}) \cdot \nabla \rho(\mathbf{r}') \left[1 - \frac{\tilde{\rho}(\mathbf{r}')}{\rho_{0s}} \right] d\mathbf{r}' \\ & - \frac{m}{4} \int V_J(|\mathbf{r} - \mathbf{r}'|) \rho(\mathbf{r}) \rho(\mathbf{r}') [\mathbf{v}(\mathbf{r}) - \mathbf{v}(\mathbf{r}')]^2 d\mathbf{r}' \end{aligned} \quad (2.14)$$

The first term corresponds to a classical Lennard-Jones type two-body interaction between the helium atoms. The interaction is screened at short distances where the interaction energy is of the same order as the correlation effects:

$$V_{LJ}(r) = \begin{cases} \epsilon_{LJ} \left[\left(\frac{\sigma}{r} \right)^{12} - \left(\frac{\sigma}{r} \right)^6 \right] & \text{if } r > h \\ 0 & \text{otherwise} \end{cases} \quad (2.15)$$

In the second line, the terms corresponding to c_2 and c_3 , correct for short range correlations when $r < h$. The weighted density $\bar{\rho}$ is the average

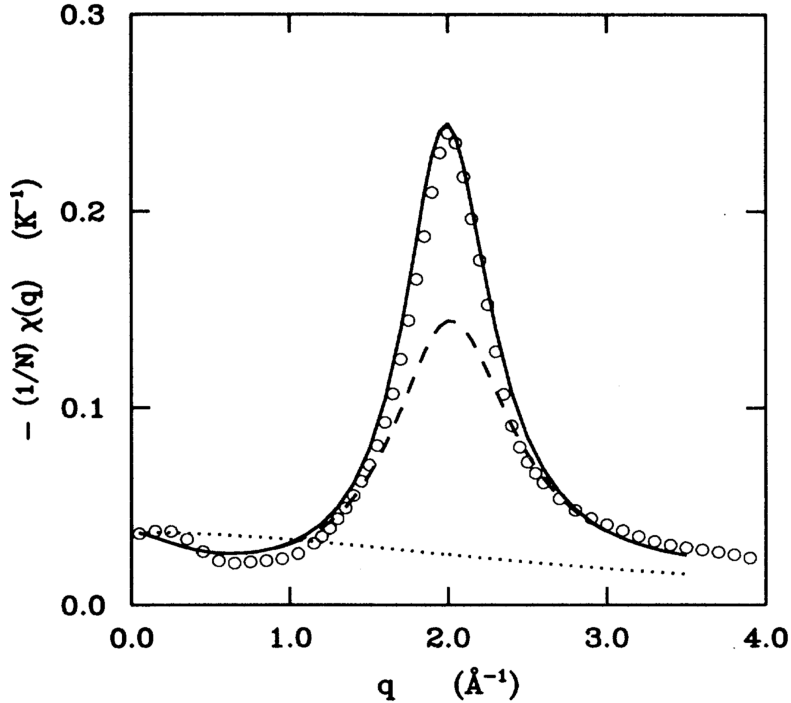


Figure 2.1: Static response function of liquid ^4He at zero pressure. Points: experimental data; dotted line: from functional of refs 15,16; dashed line: OP functional ref 1; solid line present functional.

density ρ over a sphere of radius h :

$$\bar{\rho}(\mathbf{r}) = \int \Pi_h(|\mathbf{r} - \mathbf{r}'|) \rho(\mathbf{r}') d\mathbf{r}', \quad (2.16)$$

with

$$\Pi_h(r) := \begin{cases} \frac{3}{4\pi h^3} & \text{if } r \leq h \\ 0 & \text{otherwise} \end{cases} \quad (2.17)$$

The third line is a non-local correction to the kinetic energy (KC). It partially accounts for the difference $\mathcal{T}[\rho] - T[\rho]$ mentioned in the previous section. The gradient-gradient interaction function F is a Gaussian kernel defined as

$$F(r) = \frac{1}{l^3 \sqrt{\pi^3}} e^{-r^2/l^2} \quad (2.18)$$

All the parameters are fixed to reproduce the peak of the static response function (see Fig.) in the bulk liquid. The factor $(1 - \tilde{\rho}/\rho_{0s})$ is included to match the pressure dependence of the static response function predicted by diffusion Monte Carlo calculations [ref 21 in OT paper]. The quantity $\tilde{\rho}(\mathbf{r})$ is another weighted density, calculated using F as a weight

$$\tilde{\rho}(\mathbf{r}) := \int F(|\mathbf{r} - \mathbf{r}'|) \rho(\mathbf{r}') d\mathbf{r}' \quad (2.19)$$

The density $\tilde{\rho}(\mathbf{r})$ is very close to the normal density $\rho(\mathbf{r})$ except in very inhomogeneous situations. For helium droplets one can safely use ρ instead of $\tilde{\rho}$.

Finally, in the last line in Eq. 2.14 is called the *back-flow* term and influences the dynamic response of the system. It plays the role of a non-local kinetic energy. Since the back-flow contains the factor $\mathbf{v} - \mathbf{v}'$, as defined in Eq. 1.30 the contribution will only be non-zero whenever the order parameter Ψ is complex-valued. Which means that in the time-independent case this will only affect the vortex states. The phenomenological effective current-current interaction $V_J(r)$ is calibrated so that it reproduces the experimental phonon-roton spectrum (see Fig. 1.3):

$$V_J(r) = (\gamma_{11} + \gamma_{12} r^2) e^{-\alpha_1 r^2} + (\gamma_{21} + \gamma_{22} r^2) e^{-\alpha_2 r^2} \quad (2.20)$$

All the parameters of the functional are given in Table 2.2.

2.2.1 The Solid-OT Density Functional

In the presence of highly inhomogeneous liquid densities, e.g. atomic impurities with a very strong He-X interaction, the OT-functional Eq. (2.14) becomes numerically unstable. To deal with this problem an additional cut-off can be used

$$\mathcal{E}^{\text{sol}} := C\rho(\mathbf{r}) \{1 + \tanh(\beta[\rho(\mathbf{r}) - \rho_m])\} \quad (2.21)$$

where the model parameters $\{C, \beta, \rho_m\}$ are specified in Table 2.2. Including this term in the OT-functional prevents excessive density build-up. \mathcal{E}_{sol} only starts to deviate from zero whenever the liquid density ρ is comparable to ρ_m or larger. Therefore, inclusion of this term in the functional does not alter the density distribution. This penalty term was originally developed to account for the liquid-solid phase transition of ${}^4\text{He}$ [61,62].

The functional that has been used to obtain the result presented in this work is what we call the “Solid-OT-DFT functional”. It consists of the first three terms of the original OT-functional Eq. (2.14), plus E^{sol}

$$\begin{aligned} \mathcal{E}_c^{\text{sol}}[\rho] = & \frac{1}{2} \int \left\{ \rho(\mathbf{r}) V_{LJ}(|\mathbf{r} - \mathbf{r}'|) \rho(\mathbf{r}') \right. \\ & + \frac{1}{2} c_2 \rho(\mathbf{r}) [\bar{\rho}(\mathbf{r})]^2 + \frac{1}{3} c_3 \rho(\mathbf{r}) [\bar{\rho}(\mathbf{r})]^3 \Big\} d\mathbf{r}' \\ & + C \rho(\mathbf{r}) \left\{ 1 + \tanh(\beta [\rho(\mathbf{r}) - \rho_m]) \right\} \end{aligned} \quad (2.22)$$

2.3 Static calculations

In the work presented here all the impurities are heavy compared to the mass of ${}^4\text{He}$, e.g. the mass of Rubidium is about 21 times larger than that of Helium, Xenon roughly 33 times and Argon about 10 times. Therefore we will treat the centre of mass motion of the impurities as classical. In the DFT derived EL-equations this will be modelled as an external field V_X

$$E[\rho] \rightarrow E[\rho] + \int \rho(\mathbf{r}) V_X(|\mathbf{r} - \mathbf{r}_I|) d\mathbf{r} \quad (2.23)$$

where X is the label of the used ${}^4\text{He}$ -impurity pair interaction and \mathbf{r}_I is the position of the impurity. Varying the modified functional to minimise the energy one now finds a new EL-equation in which the helium-impurity interaction is included:

$$\left\{ -\frac{\hbar^2}{2m_4} \nabla^2 + \frac{\delta \mathcal{E}_c}{\delta \rho} + V_X(|\mathbf{r} - \mathbf{r}_I|) \right\} \Psi(\mathbf{r}) = \mu \Psi(\mathbf{r}) \quad (2.24)$$

This equation is then solved in a self-consistent way by the Imaginary Time Method[ref 69] (ITM) in cartesian coordinates upon convergence. The calculations are performed in three dimensions without imposing any symmetries that are present in the external potential. All the quantities are discretised on evenly spaced cartesian grid with a grid constant that is typically of the order of 0.4. The differential operators are evaluated using a k -point finite difference method where most of the time $k = 13$ is sufficiently accurate. The integrals in the density-functional can be expressed as convolutions and can therefore be evaluated in momentum-space by exploiting the convolution theorem, using proprietary highly optimised parallel Fast Fourier Transform algorithms.

2.3.1 Producing vortical states

The helium density that minimises the energy of the vortical states Ψ_s (Eq. 1.31), introduced in Section 1.2.4 can be obtained by solving the same EL-equation as for a vortex-free droplet. This becomes more clear when we write Eq. (2.13) in cylindrical coordinates and then substitute Ψ_0 by Ψ_s :

$$\left\{ -\frac{\hbar^2}{2m} \left[\frac{1}{r} \frac{\partial}{\partial r} \left(r \frac{\partial}{\partial r} \right) - \frac{s^2}{r^2} \right] + \frac{\delta \mathcal{E}_c}{\delta \rho} \right\} \Psi_s(\mathbf{r}) = \mu \Psi_s(\mathbf{r}) \quad (2.25)$$

Written like this it is evident that the ground state Ψ_0 is just the special case for $s = 0$. Obtaining the solution using the ITM works as long as the solution has overlap with initial guess for the order parameter. Starting with a trial order parameter similar to Ψ_s will guarantee this. To do this we use the “imprinting” technique where we use the ground state density of a previously obtained vortex-free droplet and multiply it with a normalised complex factor

$$\Psi(\mathbf{r}) = \sqrt{\rho_0(\mathbf{r})} \times \frac{x + iy}{\sqrt{x^2 + y^2}} \quad (2.26)$$

where ρ_0 is the ground state density of the vortex-droplet. In cylindrical coordinates this factor is equivalent to the one in Eq. (1.31) for $s = 1$.

This changes for droplets with two or more vortices, where the cylindrical symmetry is broken and the solutions are no longer solutions of Eq. (2.25) nor eigenfunctions of the angular momentum operator. In this case the time-independent EL-equation has to be modified to include a rotational constraint

$$\mathcal{H} \rightarrow \mathcal{H} - \Omega \hat{L}_z \quad (2.27)$$

such that for a suitable choice of Ω the vortex-array solution becomes favourable to the ground state. Since these states are no longer eigenstates of the original time-dependent Hamiltonian, these states are no longer stationary and will start to rotate with frequency Ω . The initial guess for a droplet with n_v vortices can be produced using the same imprinting method as mentioned before

$$\Psi(\mathbf{r}) = \sqrt{\rho_0(\mathbf{r})} \times \prod_{j=1}^{n_v} \left[\frac{(x - x_j) + i(y - y_j)}{\sqrt{(x - x_j)^2 + (y - y_j)^2}} \right] \quad (2.28)$$

where ρ_0 is again the ground state density of the vortex-free droplet and (x_j, y_j) is the initial position of the j -th vortex-line parallel to the z -axis.

2.4 Dynamic calculations

FOR the dynamic evolution of atomic impurities excited from ns -states to $n's$ -states, we do not need to keep track of the evolution of the electronic state of the impurity since it keeps its spherically symmetric orbital. In this case we only need to describe the time evolution of the centre of mass coordinate of the impurity. As in the statics, because of the large atomic mass of the impurity compared to helium, the time evolution of the centre of mass coordinate of the impurity is treated classically. To obtain the correct energy for the whole droplet-impurity system the energy functional needs to be extended to include the impurities centre of mass motion and the impurity-helium interaction

$$E[\rho] \rightarrow E[\rho] + \frac{p_I^2}{2m_I} + \int \rho(\mathbf{r}) V_{X^*}(|\mathbf{r} - \mathbf{r}_I|) d\mathbf{r} \quad (2.29)$$

where p_I is the classical momentum of the impurity, m_I is the impurity mass and V_{X^*} is the $X-{}^4\text{He}$ pair potential for a ground-, excited- or ionised state. The equations of motion for the time evolution of the order parameter $\Psi(\mathbf{r}, t)$ and the centre of mass of the impurity $\ddot{\mathbf{r}}_I$ are

$$\begin{aligned} i\hbar \frac{\partial}{\partial t} \Psi &= \left[-\frac{\hbar^2}{2m_4} \nabla^2 + \frac{\delta \mathcal{E}_c}{\delta \rho} + V_{X^*}(|\mathbf{r} - \mathbf{r}_I|) \right] \Psi \\ m_I \ddot{\mathbf{r}}_I &= -\nabla_{\mathbf{r}_I} \left[\int \rho(\mathbf{r}) V_{X^*}(|\mathbf{r} - \mathbf{r}_I|) d\mathbf{r} \right] \\ &= - \int V_{X^*}(|\mathbf{r} - \mathbf{r}_I|) \nabla \rho(\mathbf{r}) d\mathbf{r} \end{aligned} \quad (2.30)$$

2.4.1 The DIM model

The situation becomes slightly more complicated for ns -states excited to $n'p$ -states (effective one-electron excited ${}^2\text{P}$ -states). Since the p-orbital is no longer spherically symmetric, we also need to include a description for the time evolution of the orientation of the p-orbital. To do this we use the diatomic model (DIM). The interaction between a helium atom (${}^1\text{S}_0$ -state) and the triple degenerate $L = 1$ electronic state of the impurity partially lifts the degeneracy so that the interaction can be decomposed into a Σ -state and a double degenerate Π -state (see Fig. 2.2). In the cylindrical symmetry of the DIM it is customary to use the molecular term symbol ${}^{2S+1}\Lambda_\Omega$ to label the levels. Here S is the total spin angular momentum (and $2S + 1$ the spin multiplicity), Λ is the modulus of the total orbital angular momentum

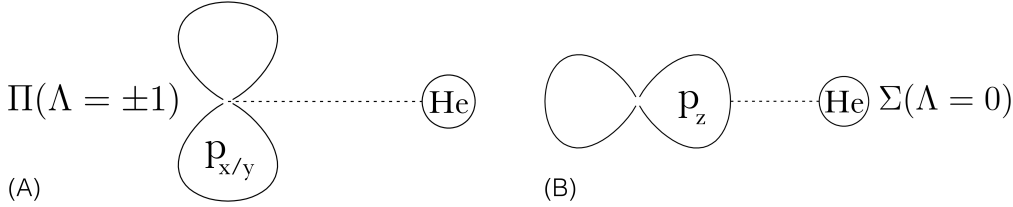


Figure 2.2: Level splitting of the p-orbitals in the presence of helium, that breaks the spherical symmetry. (A) A double degenerate $n'p_{x/y}$ -orbital and (B) a single $n'p_z$ -orbital. (Illustration courtesy of M. Martinez)

and Ω is the total angular momentum, all projected along the internuclear axis. Following the spectroscopic notation the orbitals corresponding to $\Lambda = 0, 1, 2, 3, \dots$ are labeled $\Sigma, \Pi, \Delta, \Phi, \dots$. The interaction between a helium atom and the impurity's electronic structure can be expressed in an uncoupled basis

$$|p_{im}\rangle \in \{|p_{xm}\rangle, |p_{ym}\rangle, |p_{zm}\rangle\} \quad (2.31)$$

of real one-electron p-orbitals oriented along the internuclear axis (see Fig. 2.3). The helium-impurity interaction matrix is given by

$$\begin{aligned} \mathcal{V}^{DIM}(r_m) &= V_\Pi(r_m)(|p_{xm}\rangle\langle p_{xm}| + |p_{ym}\rangle\langle p_{ym}|) + V_\Sigma(r_m)|p_{zm}\rangle\langle p_{zm}| \\ &= V_\Pi(r_m)(\mathbb{1}_3 - |p_{zm}\rangle\langle p_{zm}|) + V_\Sigma(r_m)|p_{zm}\rangle\langle p_{zm}| \\ &= V_\Pi(r_m)\mathbb{1}_3 + [V_\Sigma(r_m) - V_\Pi(r_m)]|p_{zm}\rangle\langle p_{zm}| \end{aligned} \quad (2.32)$$

where r_m is the modulus of the interatomic separation vector and V_Π and V_Σ are the Π and Σ impurity-He pair potentials in the absence of spin-orbit coupling. For a system consisting of N helium atoms the total interaction energy is calculated by summing over all the contributions of the N individual ${}^4\text{He}-\text{X}$ contributions ($\text{DIM}^{[?]}_I$)

$$\mathcal{U}^{DIM}(\mathbf{r}_I) = \sum_{m=1}^N \mathcal{V}^{DIM}(r_m) \quad (2.33)$$

It is more convenient to express the interaction in a basis common to all impurity-helium pairs, instead of a basis that depends on the particular impurity-helium pair chosen. To do this we apply a rotation $\mathcal{R}_m : \hat{\mathbf{z}}_m \mapsto \hat{\mathbf{z}} \propto \mathbf{r}_I$, so that the matrix corresponding to the m^{th} ${}^4\text{He}$ atom expressed in the common basis is given by

$$|p_{zm}\rangle\langle p_{zm}| = \mathcal{R}_m |p_z\rangle\langle p_z| \mathcal{R}_m^{-1} \quad (2.34)$$

It can be shown that the elements of this matrix in cartesian coordinates are of the form

$$\langle p_i | \mathcal{R}_m | p_z \rangle \langle p_z | \mathcal{R}_m^{-1} | p_j \rangle = \frac{r_{im} r_{jm}}{\|\mathbf{r}_m\|^2} \quad (2.35)$$

where $(i, j) \in \{x, y, z\}$. With these definitions we can write the matrix elements U_{ij}^{DIM} of the interaction energy \mathcal{U}^{DIM}

$$U_{ij}^{DIM}(\mathbf{r}_I) = \langle p_i | \mathcal{U}^{DIM} | p_j \rangle = \sum_{m=1}^N V_{ij}^{DIM}(r_m) \quad (2.36)$$

where

$$V_{ij}^{DIM}(r_m) := V_\Pi(r_m) \delta_{ij} + \left[V_\Sigma(r_m) - V_\Pi(r_m) \right] \frac{r_{im} r_{jm}}{\|\mathbf{r}_m\|^2} \quad (2.37)$$

are the matrix elements of \mathcal{V}^{DIM} expressed in the common basis. Since we are working with a continuous helium density $\rho(\mathbf{r})$ and not with discrete atoms the summation over N helium atoms in the previous expression is replaced by an integral over the density $\sum_m \rightarrow \int \rho(\mathbf{r}) d\mathbf{r}$ which finally gives for the matrix element U_{ij}^{DIM}

$$U_{ij}^{DIM}(\mathbf{r}_I) = \int \rho(\mathbf{r} + \mathbf{r}_I) V_{ij}^{DIM}(r) d\mathbf{r} \quad (2.38)$$

The eigenvalues $U_k^{np}(\mathbf{r}_I)$ of this real symmetric matrix define the potential energy curves (PECs) as a function of the distance between the surrounding helium and the impurity.

2.4.2 Including spin-orbit coupling

For the study of the alkali metal Rb in this work, the spin-orbit (SO) splitting of the energy levels is comparable to the splitting of the orbital angular momentum levels $\Lambda = 0$ and $\Lambda = \pm 1$ due to the interaction with the helium. Therefore the spin-orbit interaction needs to be included in the total interaction Hamiltonian.

The total Hamiltonian is given by the sum of the DIM-interaction and the SO-interaction $\mathcal{H} = \mathcal{U}^{DIM} + \mathcal{V}^{SO}$. The SO-matrix is defined

$$\mathcal{V}^{SO} = \frac{1}{2} A_{\ell s} (\mathbf{J}^2 - \mathbf{L}^2 - \mathbf{S}^2) \quad (2.39)$$

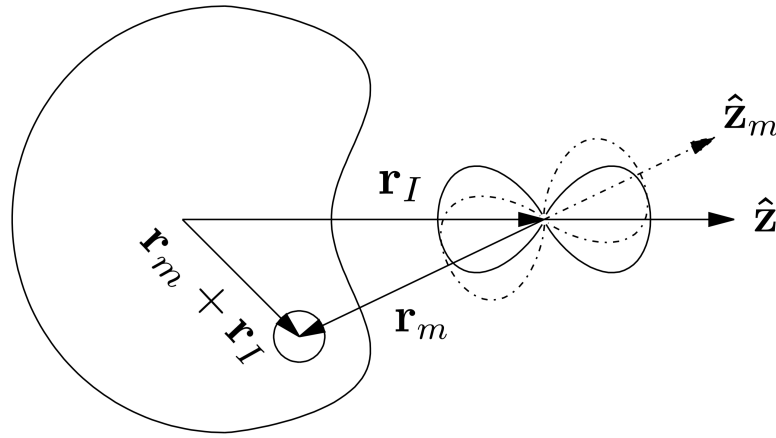


Figure 2.3: The set of axis defined in the DIM description (illustration courtesy of M. Martinez).

with $\mathbf{J} = \mathbf{L} + \mathbf{S}$. The coupling constant $A_{\ell s}$ is usually approximated by that of the free atom^[41]. We can extend the DIM basis Eq. (2.31) to include the projection of the electron spin $s = \{\uparrow, \downarrow\}$ corresponding to the quantum numbers $m_s = \{\frac{1}{2}, -\frac{1}{2}\}$:

$$|p_i, s\rangle \in \{|p_x, \uparrow\rangle, |p_x, \downarrow\rangle, |p_y, \uparrow\rangle, |p_y, \downarrow\rangle, |p_z, \uparrow\rangle, |p_z, \downarrow\rangle\}. \quad (2.40)$$

In this basis the \mathcal{V}^{SO} is given by

$$\mathcal{V}^{SO} = \frac{1}{2}A_{\ell s} \begin{pmatrix} 0 & 0 & -i & 0 & 0 & 1 \\ 0 & 0 & 0 & i & -1 & 0 \\ i & 0 & 0 & 0 & 0 & -i \\ 0 & -i & 0 & 0 & -i & 0 \\ 0 & -1 & 0 & i & 0 & 0 \\ 1 & 0 & i & 0 & 0 & 0 \end{pmatrix} \quad (2.41)$$

Kramers' theorem states that the two-fold degeneracy of the levels originating from total half-integer spin cannot be broken by electrostatic interactions^[42]. Therefore all the electronic eigenstates of \mathcal{H} are doubly degenerate. Diagonalisation of \mathcal{H} yields three doubly degenerate PECs between the impurity and surrounding helium.

The dynamic evolution of the electronic excited state of the impurity is described by introducing an additional degree of freedom, a 6-component vector $|\lambda\rangle$, which describes the coefficients of the electronic state in the

$\{|p_i, s\rangle\}$ basis

$$|\lambda(t)\rangle = \sum_{\substack{i=\{x,y,z\} \\ s=\{\uparrow,\downarrow\}}} \lambda_{is}(t) |p_i, s\rangle \quad (2.42)$$

such that $\|\langle\lambda|\lambda\rangle\|^2 = 1$. The complete set of variables required to describe the system consists of the complex valued effective wave function for helium $\Psi(\mathbf{r}, t)$ with $\rho(\mathbf{r}, t) = |\Psi(\mathbf{r}, t)|^2$, the impurity position $\mathbf{r}_I(t)$, and the 6-dimensional complex vector to determine its electronic wave function $|\lambda(t)\rangle$. The total energy of the impurity- ${}^4\text{He}_N$ complex after excitation to the ${}^2\text{P}$ manifold is

$$\begin{aligned} E[\Psi, \mathbf{r}_I, \lambda] &= \frac{\hbar^2}{2m} \int |\nabla\Psi|^2 d\mathbf{r} + \int \mathcal{E}_c[\rho] d\mathbf{r} \\ &\quad + \frac{p_I^2}{2m_I} + \int \rho(\mathbf{r}) V_\lambda(\mathbf{r} - \mathbf{r}_I) d\mathbf{r} + \langle \lambda | \mathcal{V}^{SO} | \lambda \rangle \end{aligned} \quad (2.43)$$

where V_λ is defined as

$$V_\lambda(\mathbf{r}) := \langle \lambda | \mathcal{V}^{DIM} | \lambda \rangle = \sum_{ijss'} \lambda_{is}^* V_{ijss'}^{DIM}(\mathbf{r}) \lambda_{js'} \quad (2.44)$$

and the components of the 6×6 matrix \mathcal{V}^{DIM} given by

$$V_{ijss'}^{DIM}(\mathbf{r}) = V_{ij}^{DIM} \delta_{ss'} = \left\{ V_\Pi(r) \delta_{ij} + [V_\Sigma(r) - V_\Pi(r)] \frac{r_i r_j}{\|\mathbf{r}_m\|^2} \right\} \delta_{ss'} \quad (2.45)$$

Unlike for the static DFT case, the time evolution of the system is obtained by minimising the following action

$$\begin{aligned} A[\Psi, \mathbf{r}_I, \lambda] &= \int \left\{ E[\Psi, \mathbf{r}_I, \lambda] - i\hbar \int \Psi^*(\mathbf{r}) \frac{\partial}{\partial t} \Psi(\mathbf{r}) d\mathbf{r} \right. \\ &\quad \left. - i\hbar \left\langle \lambda \left| \frac{\partial}{\partial t} \right| \lambda \right\rangle - \frac{1}{2} m_I \ddot{\mathbf{r}}_I^2 \right\} dt \end{aligned} \quad (2.46)$$

Variation of the action A with respect to $\{\Psi^*, \langle \lambda |, \mathbf{r}_I\}$ yields the following three coupled EL-equations

$$\begin{aligned} i\hbar \frac{\partial}{\partial t} \Psi &= \left[-\frac{\hbar^2}{2m} \nabla^2 + \frac{\delta \mathcal{E}_c}{\delta \rho(\mathbf{r})} + V_\lambda(\mathbf{r} - \mathbf{r}_I) \right] \Psi \\ i\hbar \frac{\partial}{\partial t} |\lambda\rangle &= \mathcal{H} |\lambda\rangle \\ m_I \ddot{\mathbf{r}}_I &= -\nabla_{\mathbf{r}_I} \left[\int \rho(\mathbf{r}) V_\lambda(\mathbf{r} - \mathbf{r}_I) d\mathbf{r} \right] = - \int V_\lambda(\mathbf{r} - \mathbf{r}_I) \nabla \rho(\mathbf{r}) d\mathbf{r} \end{aligned} \quad (2.47)$$

where the explicit time dependence of the variables is omitted for clarity. The second line of Eq. (2.47) is a 6×6 matrix equation with the matrix elements of \mathcal{H} given by

$$H_{ijss'} = U_{ijss'}^{DIM} + V_{ijss'}^{SO} = \int \rho(\mathbf{r}) V_{ijss'}^{DIM}(\mathbf{r} - \mathbf{r}_I) d\mathbf{r} + V_{ijss'}^{SO} \quad (2.48)$$

In the cases that SO-coupling can be neglected the 6-dimensional electronic state vector $|\lambda\rangle$ reduces to the 3-dimensional vector

$$|\lambda(t)\rangle = \sum_{i=\{x,y,z\}} \lambda_i(t) |p_i\rangle \quad (2.49)$$

and the 6×6 matrix \mathcal{H} reduces to the 3×3 matrix of Eq. (2.38) with elements

$$H_{ij} = U_{ij}^{DIM} = \int \rho(\mathbf{r}) V_{ij}^{DIM}(\mathbf{r} - \mathbf{r}_I) d\mathbf{r} \quad (2.50)$$

For the technical details about how this method is implemented the interested reader is directed to^[43]. For the collection of Fortran code that has been used to obtain the results presented here see [??]. For the manual to use the code see^[43].

Part I

Photo-excitation dynamics of alkalis

Chapter 3

Alkali-doped nanodroplets

In their 1996 paper^[44] Griffin and Stringari have argued that almost 100% Bose-Einstein Condensation could be achieved in the low density surface region of superfluid He at $T = 0$, as opposed to only about 10% in the bulk. It is therefore evident that a minimally perturbing probe capable of investigating the surface of a He cluster is very desirable.

It comes as no surprise then that alkali atoms are a very natural choice for exactly these type of studies. For example, with a solvation parameter of $\lambda = 0.729$ ^[29], Rb will remain bound to the surface of the droplet. Furthermore, they have a simple, well known, absorption spectrum. They introduce only weak perturbations (alkali-helium interaction energies are on the order of 1 cm^{-1} [8]). Moreover, their simple, one-valence electron structure allows for detailed theoretical modelling. Lastly, theoretical calculations [9, 10] and experimental spectra [11-13] of alkali atoms in bulk liquid helium are available for comparison.

Surprisingly, the study of alkali atoms seeded in highly quantum matrices is relevant to the optimisation of the use of solid hydrogen as a rocket propellant^[45].

Given that the alkalies are ideal probes to probe the boundary region of the nanodroplets, the $np^2\text{P} \leftarrow ns^2\text{S}$ transitions of the alkali atoms have attracted much interest from an experimental and theoretical point of view. The spectroscopy of the higher excited states has been thoroughly explored[32-42]. The obtained spectra can be successfully reproduced by a pseudo-diatomic model[9,21], except for the higher excited states, where the model progressively fails due to the limitations imposed by its realm of validity. While the effect of the excited states on the spectra are now fairly well understood, their influence on the following dynamics is largely

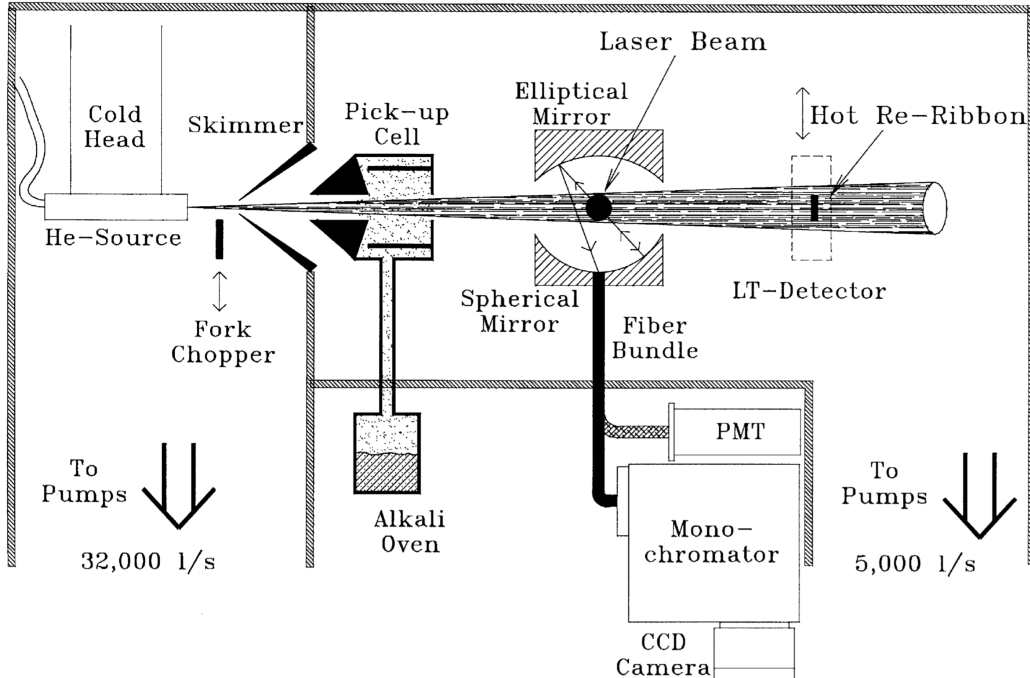


Figure 3.1: Caption

unexplored.

In this part of the thesis, the results of the real-time dynamics of a single electronically excited rubidium (Rb) atom, residing in the surface dimple of a helium nano-droplet will be presented. The atom will be excited from its ground state $5s\ 2\Sigma_{1/2}$ to the $5p\ ^2\{\Sigma, \Pi\}$ and $6p\ ^2\{\Sigma, \Pi\}$ manifold. This will be a combined experimental and theoretical study.

3.1 Experimental setup

A beam of large He clusters is produced in a supersonic expansion from a cold nozzle (Fig. 3.1). The weak He-He binding energy of 7.7 cm^{-1} [22] requires high stagnation pressures and low nozzle temperatures (T) for large cluster formation. In our apparatus two CTI cryocoolers are used to establish low temperature conditions (down to 12 K) at the source. The first cooler directly cools the nozzle while the second pre-cools the supplied gas. This is needed because, even for small nozzle diameters ($10\text{ }\mu\text{m}$), at stagnation pressures up to 10^7 Pa the $1/\sqrt{T}$

dependence of the gas flux leads to heavy gas loads. The pre-cooling system also provides for gas purification. The high gas throughput is easily handled by a 32000 1/s diffusion pump.

At these low temperatures seeding clusters with a chromophore cannot be achieved by co-expansion and the pick-up seeding method becomes necessary [23]. According to this method, the cluster beam is sent through a scattering cell (located a short distance after the skimmer) in which a variable pressure (10^{-3} – 10^{-1} Pa) of the chromophore is maintained by connecting it with an alkali reservoir through a heated tube. The temperature of the pick-up cell, (100 K higher than the reservoir), avoids alkali atom distillation and formation of dimers inside the cell. In their path through the cell the larger clusters pick up alkali atoms without being appreciably deflected. Dissipation of the energy of the captured chromophore is likely to occur by evaporation of He atoms from the clusters, the terminal temperature of which rapidly returns to its pre pick-up value (\approx 0.4 K) [2].

To probe the picked-up alkali atoms we use laser induced fluorescence (LIF) adopting the photon collection optics design described by Hefter and Bergmann in [24]. The intersection point of the laser and cluster beam from which the fluorescence photons are collected is located a few centimetres downstream of the pick-up cell. The light of the probe laser is introduced in the apparatus via a single mode fibre and focusing optics that makes the laser beam diameter at the crossing point approximately the same as the cluster beam diameter (\approx 2 mm). To suppress scattered laser light we use a stack of diaphragms forming a baffle of 90 cm length both for the in- and outgoing laser beam. A Woods horn serves as a beam dump. To detect the fluorescence light originating at the point of intersection, the combination of an elliptical and a spherical mirror is used. These two mirrors focus the emitted photons at the entrance of a fibre bundle. The geometrical collection efficiency is 85% of the 4π solid angle centred around the intersection point. After passing through the fibre bundle, the photons reach a photomultiplier (PMT) for signal detection. The output pulses of the PMT are (after standard amplification and discrimination) stored using two gated counters which follow the cluster beam chopping frequency. Alternatively, a monochromator (GCA / McPherson, EU-700) coupled to a liquid nitrogen cooled CCD detector (Princeton Instruments, LN/CCD 1152 UV) is used for dispersed fluorescence measurements. The absolute frequency of the probe laser is monitored continuously by a home built wave meter with 0.001 cm^{-1} precision. The amount and angular distribution of alkali atoms carried by the clusters can be monitored by means of a Langmuir-Taylor (LT) surface ionisation detector which is located further down-stream and is movable perpendicularly to the cluster beam direction. Since excitation

at certain frequencies leads with a significant probability to a desorption of the chromophores from the cluster, we are also able to detect beam depletion spectra. Finally the LT detector provides information on the alkali atom density inside the pick-up cell by measuring the alkali background inside the detection chamber. A computer controls the laser frequency and records the acquisition of photon counts, the actual laser frequency and the parameters for cluster beam and alkali source condition characterisation.

proof is in spectra; not as shifted as in the bulk

finally introduce experiment Vangerov et al

photo dissociation/ejection all but lowest part of $P_1/2$ excitation

introduce electronic spin relaxation to explain and Mudrich

Chapter 4

Results

4.1 Imaging Excited-State Dynamics

THE following article will focus on imaging and characterising the dynamics using femtosecond spectroscopy and time-dependent density functional theory. Specifically on the idea of a fall-back time, which is defined as the time delay $\tau := t_{ion} - t_{exc}$ between the time instance of the photo-excitation of Rb to the 5p and 6p states, and the time instance of its photo-ionisation, such that the Rb cation is still solvated by the helium droplet.

EXPLAIN SHORT PUMP-PROBE LASER EXPERIMENTS

Imaging Excited-State Dynamics of Doped He Nanodroplets in Real-Time

Johannes von Vangerow,[†] Fran ois Coppens,[‡] Antonio Leal,[§] Marti Pi,[§] Manuel Barranco,^{§,‡} Nadine Halberstadt,[‡] Frank Stienkemeier,[†] and Marcel Mudrich^{*,†,¶}

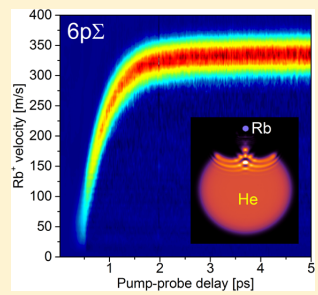
[†]Physikalisches Institut, Universit at Freiburg, Hermann-Herder-Str. 3, 79104 Freiburg, Germany

[‡]Laboratoire des Collisions, Agr gats, R activit , IRSAMC, UMR 5589, CNRS et Universit  Paul Sabatier-Toulouse 3, 118 route de Narbonne, F-31062 Toulouse Cedex 09, France

[§]Departament FQA, Facultat de F sica, and IN2UB, Universitat de Barcelona, Diagonal 645, 08028 Barcelona, Spain

Supporting Information

ABSTRACT: The real-time dynamics of excited alkali metal atoms (Rb) attached to quantum fluid He nanodroplets is investigated using femtosecond imaging spectroscopy and time-dependent density functional theory. We disentangle the competing dynamics of desorption of excited Rb atoms off the He droplet surface and solvation inside the droplet interior as the Rb atom is ionized. For Rb excited to the 5p and 6p states, desorption occurs on starkly differing time scales (~ 100 versus ~ 1 ps, respectively). The comparison between theory and experiment indicates that desorption proceeds either impulsively (6p) or in a transition regime between impulsive dissociation and complex desorption (5p).



He nanodroplets are intriguing quantum fluid objects of finite size capable of efficiently capturing and cooling atoms, molecules, and clusters for spectroscopy and dynamics studies.^{1,2} Upon electronic excitation, embedded atoms and small molecules tend to move toward the droplet surface and may be ejected due to short-range electron-He repulsion.³ In contrast, cations experience attractive forces toward the He droplets mediated by electrostatic polarization, which draw them to the droplet interior, where they may form snowball complexes.^{4–7} These two opposing trends lead to a rich dynamics initiated by photoexcitation of embedded species involving desorption, electronic relaxation, complex formation, as well as solvation and desolvation of the ionized impurity. Similar dynamics have been observed when exciting pure He droplets with extreme-ultraviolet radiation²⁰ as well as for other types of clusters.²¹

So far, time-resolved experiments on He droplets doped with alkali (Ak) metal atoms were mostly focused on the formation of AkHe exciplexes induced by laser excitation.^{15–18,22,23} The concurrent desorption of these excited species was estimated to proceed on a picosecond time scale.^{9,10,13,24–26} This estimate, sufficient for studies employing nanosecond laser pulses, clearly lacks precision for experiments with sub-picosecond time resolution. Thus in the previous measurements as well as in experiments focusing on electronic and vibrational coherences of Ak atoms and molecules^{17,19,22,23,27} the exact location of the dopants, attached to the droplets or in the vacuum, has remained somewhat uncertain.

Here we report a combined experimental and theoretical investigation of the excited-state dynamics of doped He nanodroplets in real time. The combination of fs pump-probe spectroscopy with velocity map imaging (VMI)²⁸ allows us to clearly disentangle complex formation, desorption, and ion solvation. As a model system, we investigate He droplets doped with single rubidium (Rb) atoms. Ground-state Rb atoms and small molecules are weakly bound to the He droplet surface in a dimple structure.^{29–31} Therefore, the ejection dynamics of the excited Rb atom (Rb*) is not affected by processes such as the interaction of Rb* with density waves traveling in the bulk of the droplet, as for Ag*.¹¹

We excite droplet-bound Rb atoms to states correlating either to the lowest excited state 5p or to the higher lying state 6p. The dynamics is probed by ionizing Rb* at variable delay times between photoexcitation ($t = 0$) and photoionization ($t = t_+$) while monitoring the velocity and signal yield of Rb⁺ ions. A simulation based on time-dependent density functional theory (TDDFT) gives us insight into the time evolution both of Rb* and of the Rb⁺ ion taking into account the quantum fluid properties of the He environment. Using these techniques, we follow the trajectory of the excited and subsequently ionized Rb atom in detail as it escapes from the droplet surface or submerges into it. Although separated by only ~ 1.4 eV in energy, the two states 5p and 6p are found to feature time

Received: November 6, 2016

Accepted: December 20, 2016

Published: December 20, 2016

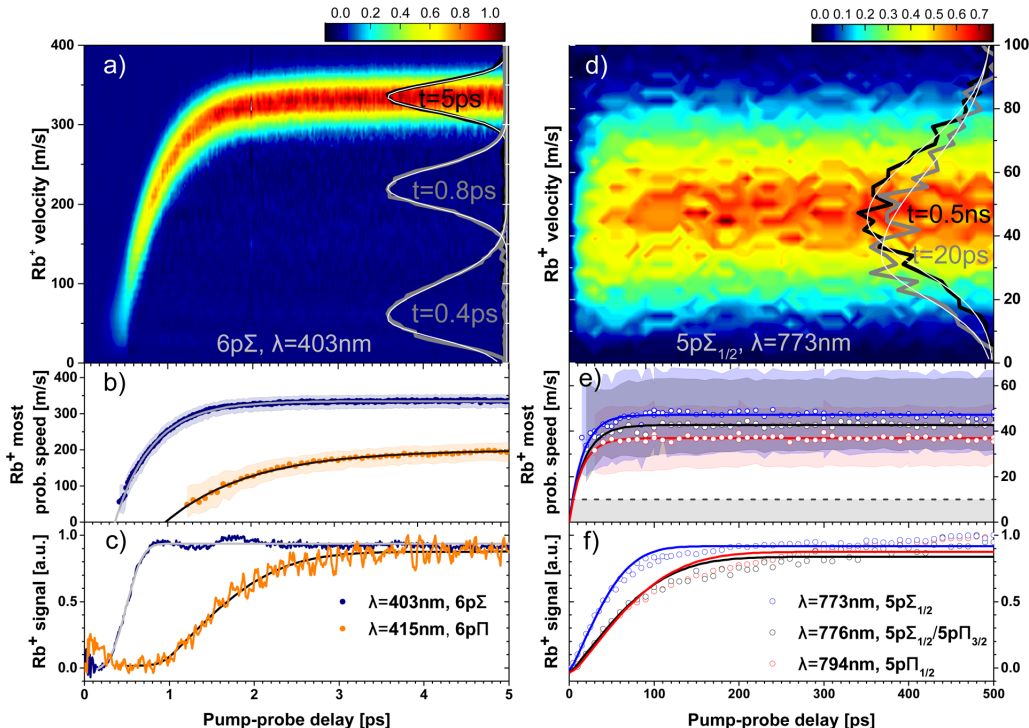


Figure 1. Rb⁺ transient speed distributions (a,d), most probable speeds (b,e), and ion yields (c,f) resulting from photoexcitation to He droplet perturbed states correlating to 6p (left column) and 5p states (right column) of Rb (pump) and subsequent ionization (probe). The shaded areas (b,e) indicate the left and right $\epsilon^{-1/2}$ widths of the speed distributions. The shaded area at the bottom of panel e depicts the experimental resolution. The smooth lines are fits to the data (see text).

constants of the desorption dynamics differing by about 2 orders of magnitude.

Figure 1a,d shows examples of measured Rb⁺ transient speed distributions derived from the VMIs by angular integration. From these distributions we infer the most probable speeds (b,e) by fitting a skewed Gaussian distribution as illustrated by selected speed distributions shown on the right-hand sides of Figure 1a,d.³⁴ For the droplet perturbed Rb 6p states the most probable speeds (b) as well as the total Rb⁺ ion yields (c) show a steep rise within a few picoseconds. In contrast, for the droplet perturbed 5p states we record speed distributions (e) close to our experimental resolution of ~10 m/s (shaded gray area) and ion yields (f) which increase within hundreds of picoseconds.

For the droplet perturbed Rb 6p excitations, the transient ion yield curves (c) have previously been interpreted in terms of the competing effects of repulsion from the He droplet surface and attraction of Rb⁺ toward it.¹⁴ Accordingly, the slower dynamics of the 6pΠ state compared with that of the 6pΣ state is due to the weaker repulsion from the droplet. We term “fall-back time”, τ_c , the critical delay discriminating between the ion falling back into the droplet and the ion escaping into the vacuum. It is obtained by fitting the 6p and 5p ion yield data with piecewisely defined asymmetric error function $I(t) = A_0 + A \cdot \{[t \leq \mu] \sigma_- \cdot \text{erf}[(t - \mu)/\sigma_-] + [t > \mu] \sigma_+ \cdot \text{erf}[(t - \mu)/\sigma_+]\}$, where σ_{\mp} denote widths on the right and left side of the inflection point μ . τ_c is obtained from computing the 50% rise time of that fit function. The evolution of the most probable

speeds \hat{v} is fitted by $\hat{v}(t) = \hat{v}_f \{1 - \exp[-\ln 2 \cdot (t - t_0)/\tau_v]\}$, from which we obtain the characteristic 50% rise times $\tau_v = t_0 + \tau_c$.

Note that for each applied pump–probe delay we measure the final velocity distribution of the ion after it has fully escaped from the droplet. Therefore, the experiment does not give direct access to the desorption dynamics of the neutral Rb^{*} atom. To get a complete picture of the dynamics, simulations based on the TDDFT approach are carried out using the functional of ref 35. Details of this approach have been described before.^{9,11,32} In short, we consider droplets consisting of $N = 1000$ atoms doped with one Rb atom. Because of its large mass compared with that of He we describe the dynamics of the Rb atom classically. The simulations of the full pump–probe sequence consist of two steps: the propagation of Rb^{*} in the excited state starting at $t = 0$ (step 1) and the propagation of the Rb⁺ ion at times $t > t_+$ (step 2). This is achieved by solving the coupled 3D TDDFT and Newton’s equations for the He droplet and the Rb impurity, respectively.

In step 1, the Rb^{*}–droplet interaction is obtained from the Rb^{*}–He $n\Sigma$ and $n\Pi$ pair potentials³⁶ with $n = 5$ and 6, and includes the spin–orbit interaction in the usual He–Rb^{*} distance-independent way; it also allows for the dynamic evolution of the internal electronic state of the Rb^{*} atom.¹¹ In step 2, the coupled dynamical equations are now simpler as they do not explicitly take into account the electronic structure of the closed-shell Rb⁺ ion. In all simulations, a spatial grid of 0.4 Å and a time step of 0.5 fs are used.

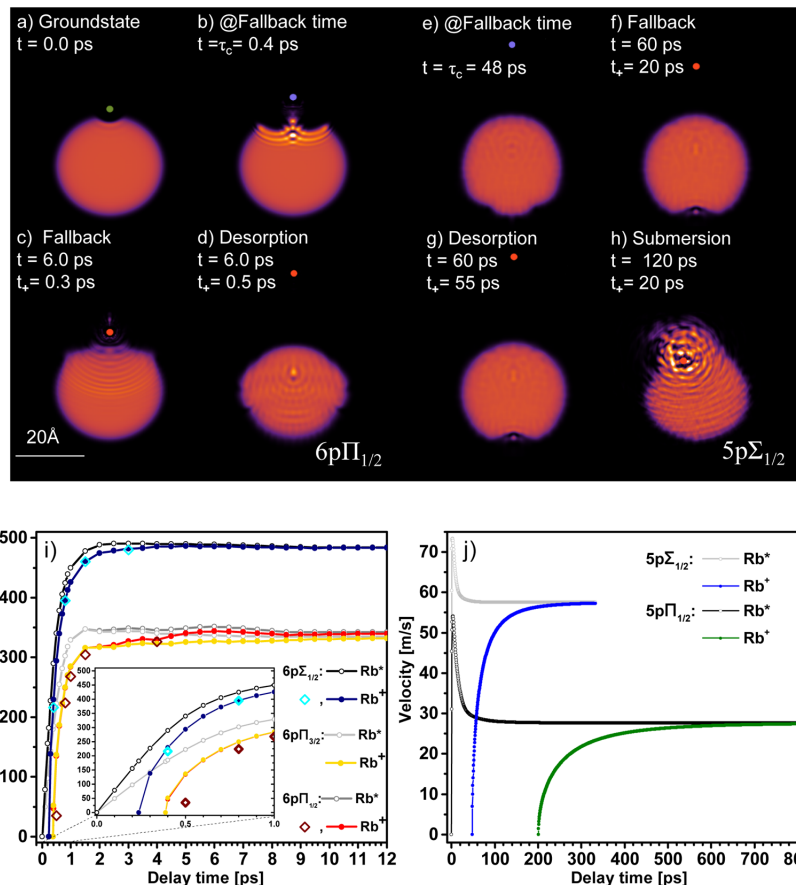


Figure 2. TDDFT-based 2D densities (a–d,e–h) and velocities (i,j) of Rb atoms attached to He_{1000} excited from equilibrium (a) to droplet perturbed 6p (left column) and 5p (right column) states. Configurations are shown for different propagation times t and ionization times t_+ : (b,e) neutral Rb at fall-back time $t = \tau_c$; (c,f) $t_+ < \tau_c$ fall-back of Rb^+ ion; (d,g) $t_+ > \tau_c$, desorption of Rb^+ ; (h) solvation of Rb^+ ; (i,j) evolution of Rb^* velocities with time t (gray open dots), and final velocities of Rb^+ (colored filled dots) as a function of t_+ .

For step 1, initial conditions are given by the structure of the neutral $\text{Rb}-\text{He}_{1000}$ complex in the ground state³² obtained using the $\text{Rb}-\text{He}$ potential of ref 37. For step 2 the initial conditions are given by the step 1 simulation at $t = t_+$. Carrying out the full simulations for step 2 is crucial for short and intermediate delays $t_+ \lesssim \tau_c$ as the droplet is still far from being relaxed when Rb^* is photoionized. At variance, we have checked that keeping the droplet density frozen as done in ref 14 is a good approximation for long delays $t_+ \gg \tau_c$. In Figure 2i the open diamonds show the difference between carrying out the full simulation and keeping the He density frozen at $t = \tau_c$ for $t_+ \gtrsim \tau_c$ (filled dots). For illustration, these simulations are provided as animations in the Supporting Information.

Figure 2a–d,e–h shows snapshots of the resulting 2D densities for different propagation times t and ionization times t_+ for the $6p\Pi_{1/2}$ (left column) and $5p\Sigma_{1/2}$ (right column) states. The ground-state dimple configuration is depicted in panel a. Figure 2b,e shows the configurations at the fall-back time τ_c . Panels c, d and g, h illustrate the desorption and fall-back processes. When ionization occurs before the fall-back time, $t_+ < \tau_c$ the ion turns around and submerges into the

droplet, where it becomes fully solvated (h). For $t_+ > \tau_c$ the ion keeps moving away from the droplet surface and fully desorbs (d, g). Panels i, j show the velocities of Rb^* (open symbols) and Rb^+ ions (filled symbols). The inset shows a close-up of the 6p dynamics at short propagation times.

For the 6p states, the Rb^* velocity features a steep rise that levels out after ~ 2 ps propagation time t (gray open dots). The final Rb^+ velocity is reduced compared with the Rb^* velocity at short delays $t_+ \lesssim 10$ ps (colored dots) due to the attraction of the Rb^+ ion toward the He droplet. For long delays these values converge as the Rb^+-He droplet attraction drops off at large distances. For the 5p case, the Rb^* velocity shows an overshoot at short delays relative to the asymptotic value. This is due to the transient Rb^*-He droplet interaction being weakly attractive at intermediate distance, which slows down the ejected Rb^* atom. It derives from the Rb^*-He potentials featuring an outer attractive region.

A compilation of the time constants for fall-back, τ_c , rise times of the ion speed, τ_v , as well as most probable Rb^+ final velocities, \hat{v}_f inferred from the experimental and theoretical data, is presented in Figure 3. The theory values of τ_v are

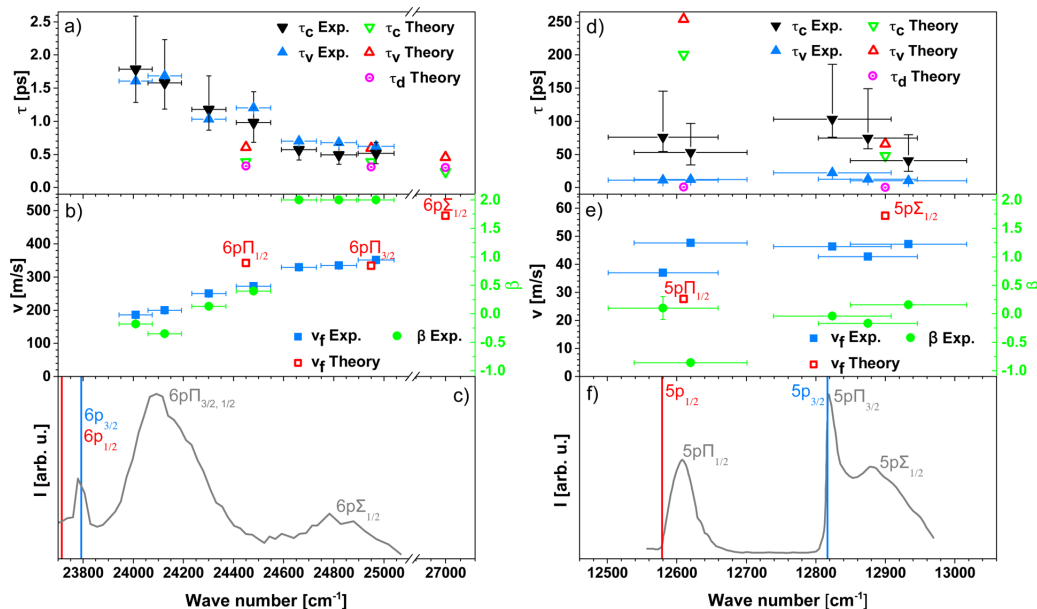


Figure 3. Experimental and theoretical fall-back time constants τ_c (a,d), velocity rise times τ_v (a,d), theoretical Rb* desorption times τ_d (a,d), Rb⁺ final most probable speeds v_f (b,e), and anisotropy parameters β (b,e) for different excitation wavenumbers corresponding to droplet perturbed Rb states 6p (left column) and 5p (right column). Panels c and f show fluorescence emission spectra as reference.^{25,38} Vertical lines indicate free atomic transitions.

determined by fitting the final ion velocities using the same model as for the experimental data. In addition, Figure 3a,d contains desorption times τ_d of the neutral Rb* atoms inferred from the simulation by fitting the same model as for ion velocities. Note that for the 5p $\Pi_{1/2}$ and 5p $\Sigma_{1/2}$ states we obtain values $\tau_d = 0.4$ and 0.2 ps, respectively, from the rising edges of the speed curves in Figure 2j. Figure 3b,e displays the anisotropy parameter β of the Rb⁺ angular distributions measured at long delay times. For reference we include the corresponding fluorescence excitation spectra taken from literature.^{25,38} Excitation wavenumbers for the theory values correspond to the peak positions of the simulated absorption spectra (not shown). Vertical error bars are connected to widths of the asymmetric fit function. Horizontal error bars reflect the spectral widths (FWHM) of the fs laser pulses.

The experimentally observed drastic difference between time scales for the 6p and 5p state dynamics is well-reproduced by the calculation. The general trend that fall-back times τ_c decrease and final velocities rise as a function of excitation wavenumber reflects the increasing repulsion acting between Rb* and the He droplet as the excitation energy is tuned up.^{9,13,24,26,32} Fall-back times τ_c and speed rise times τ_v exceed the desorption times τ_d of the neutral Rb* atom because the range of Rb⁺-He attractive interaction is larger than that of Rb*-He repulsion.¹⁴

Discrepancies are found for the asymptotic velocities of the 6p states that are smaller in the experiment than in the simulation by a factor of ~ 0.7 . Accordingly, experimental fall-back and speed rise times exceed the simulated values by a factor of 2 for the 6p $\Sigma_{1/2}$ and up to a factor of 4 for the 6p Π states. We attribute this mainly to the limited accuracy of the 6p Σ and 6p Π Rb*-He pair potentials³⁶ used in the simulation, causing a substantial blue shift of the simulated 6p \leftarrow 5s

absorption spectrum (not shown) with respect to the measured one.^{24,25}

For the 5p states the fall-back times being considerably larger than the speed rise times indicates that the desorption dynamics deviates to some extent from the impulsive model. In the limit of statistical desorption of Rb* atoms by an evaporation-like process, one would expect a continuously rising yield of free atoms and broad thermal distributions. Considering the slightly delayed, slow rise of the Rb⁺ yield (Figure 1f) and the peaked but broadened speed distributions that feature only small up-shifts at short delays (Figures 1d,e), we conclude that the dynamics of 5p excited states proceeds in a transition regime from impulsive dissociation to more complex, evaporation-like desorption. This conclusion is supported by the anisotropy parameter β (Figure 3e), whose sign correctly indicates the symmetry of the dissociating complex^{9,13,24} but whose absolute value is significantly reduced compared with that expected for impulsively dissociating complexes, in contrast with the 6p case (Figure 3b). Consequently, the quantitative agreement with the simulations, which do describe complex dynamical couplings within the superfluid model (Figure 2j) but do not contain statistical evaporation, is limited.

Aside from this, the experimentally observed higher final ion velocity and smaller fall-back time for the 5p $\Pi_{1/2}$ state compared with theory may be due to the measured signals being dominated by excitation of the blue edge of the 5p $\Pi_{1/2}$ feature. Considering the observed steep rise of fall-back time and drop of Rb⁺ velocity toward the red edge of the 5p $\Pi_{1/2}$ feature, our results agree with the previous finding that Rb* remains attached to the droplet surface upon narrow-band excitation at the red edge of the 5p $\Pi_{1/2}$ state.^{39,40}

Excitation of the $5p\Pi_{3/2}$ state leads to the formation of RbHe exciplexes because the Rb * -He pair interaction is strongly attractive in this state.^{15,16,38} While exciplex formation is reproduced by the simulation, the ejection of exciplexes off the He droplet surface is not. However, we find that nonradiative relaxation to the $5p\Pi_{1/2}$ state may supply enough kinetic energy to the Rb * atom to cause ejection. We therefore argue that when tuning the fs laser to the $5p\Pi_{3/2}$ peak, the experimentally observed Rb $^+$ signal is mainly due to spin relaxation to the $5p\Pi_{1/2}$ state.³⁸ Possibly the admixture of the nearby repulsive $5p\Sigma_{1/2}$ state also contributes. The relaxation dynamics will be further studied using time-resolved photoelectron spectroscopy. Let us mention that the RbHe $^+$ pump–probe transients (not shown) closely follow the ones of Rb $^+$ but significantly differ from those previously measured using a one-color NIR scheme.^{15,22} This raises some doubts as to the previous interpretation in terms of exciplex formation times and should be further investigated.

In conclusion, the observed dynamics of femtosecond pump–probe photoionization of Rb atoms attached to He nanodroplets is determined by the competition between the repulsive interaction of the droplet with the Rb atom in an excited state and the attractive interaction of the droplet with the Rb $^+$ cation, causing either desorption of Rb * off the droplet or submersion of the Rb $^+$ ion into the droplet interior, respectively. The resulting desorption dynamics proceeds impulsively within ~ 1 ps for the 6p excited states and in a transition regime between impulsive dissociation and statistical desorption within ~ 100 ps for the 5p states. This interplay between opposing trends (Rb * repulsion, Rb $^+$ attraction) is likely to be present in other types of clusters and condensed phase systems probed by time-resolved photoionization spectroscopy.

■ EXPERIMENTAL METHODS

The experimental setup has been previously described.^{14,32} In brief, He droplets with an average diameter of 10 nm are created by continuous supersonic expansion and doped by one Rb atom on average.^{14,32} The laser system generates amplified pulses of 100 fs duration at a repetition rate of 5 kHz with a tunable center wavelength in the near-infrared (NIR) region. Light in the visible range (VIS) is generated by frequency doubling. Pulses are split and separated in time in a Mach-Zehnder type interferometer. Droplet perturbed Rb 6p and 5p states are probed by one-color VIS and two-color NIR+VIS pump–probe schemes, respectively. NIR pulses are strongly attenuated to avoid excitations to higher lying states. Photoions are detected by a VMI spectrometer.^{24,28,32} For varying pump–probe delay steps, mass-selected ion VMIs are recorded and inverse-Abel transformed.³³ For each pump–probe scheme, a background contribution from ionization of effusive Rb is observed. In the measurement probing the Rb 6p states, additional background arises from single pulse ionization. To extract the pump–probe correlated dynamics, these contributions are subtracted from the signal.

■ ASSOCIATED CONTENT

Supporting Information

The following files are available free of charge. The Supporting Information is available free of charge on the ACS Publications website at DOI: [10.1021/acs.jpclett.6b02598](https://doi.org/10.1021/acs.jpclett.6b02598).

Desorption and fall-back dynamics of Rb atoms initially excited to the $5p\Pi_{1/2}$ state and ionized at $t_+ = 20$ ps. (AVI)

Desorption dynamics for $5p\Pi_{1/2}$ excitation and $t_+ = 55$ ps. (AVI)

Desorption and fall-back dynamics for $6p\Pi_{1/2}$ excitation $t_+ = 0.3$ ps. (AVI)

Desorption dynamics for $6p\Pi_{1/2}$ excitation and $t_+ = 0.5$ ps. (AVI)

■ AUTHOR INFORMATION

Corresponding Author

*E-mail: mudrich@physik.uni-freiburg.de.

ORCID

Marcel Mudrich: [0000-0003-4959-5220](https://orcid.org/0000-0003-4959-5220)

Notes

The authors declare no competing financial interest.

■ ACKNOWLEDGMENTS

Financial support for this work by the Deutsche Forschungsgemeinschaft (grant nos. MU 2347/6-1 and IRTG 2079), DGI, Spain (grant no. FIS2014-52285-C2-1-P), and HPC resources from CALMIP (Grant P1039) is gratefully acknowledged. M.B. thanks the Université Féderale Toulouse Midi-Pyrénées for financial support through the “Chaires d’Attractivité 2014” program IMDYNHE.

■ REFERENCES

- Toennies, J. P.; Vilesov, A. F. *Angew. Chem., Int. Ed.* **2004**, *43*, 2622.
- Stienkemeier, F.; Lehmann, K. *J. Phys. B: At., Mol. Opt. Phys.* **2006**, *39*, R127.
- Brauer, N. B.; Smolarek, S.; Loginov, E.; Mateo, D.; Hernando, A.; Pi, M.; Barranco, M.; Buma, W. J.; Drabbels, M. *Phys. Rev. Lett.* **2013**, *111*, 153002.
- Tiggesbäumker, J.; Stienkemeier, F. *Phys. Chem. Chem. Phys.* **2007**, *9*, 4748–4770.
- Müller, S.; Mudrich, M.; Stienkemeier, F. *J. Chem. Phys.* **2009**, *131*, 044319.
- Theisen, M.; Lackner, F.; Ernst, W. E. *Phys. Chem. Chem. Phys.* **2010**, *12*, 14861–14863.
- Zhang, X.; Drabbels, M. *J. Chem. Phys.* **2012**, *137*, 051102.
- Smolarek, S.; Brauer, N. B.; Buma, W. J.; Drabbels, M. *J. Am. Chem. Soc.* **2010**, *132*, 14086–14091.
- Hernando, A.; Barranco, M.; Pi, M.; Loginov, E.; Langlet, M.; Drabbels, M. *Phys. Chem. Chem. Phys.* **2012**, *14*, 3996–4010.
- Loginov, E.; Drabbels, M. *J. Chem. Phys.* **2012**, *136*, 154302.
- Mateo, D.; Hernando, A.; Barranco, M.; Loginov, E.; Drabbels, M.; Pi, M. *Phys. Chem. Chem. Phys.* **2013**, *15*, 18388–18400.
- Leal, A.; Mateo, D.; Hernando, A.; Pi, M.; Barranco, M.; Ponti, A.; Cargnoni, F.; Drabbels, M. *Phys. Rev. B: Condens. Matter Mater. Phys.* **2014**, *90*, 224518.
- Loginov, E.; Hernando, A.; Beswick, J. A.; Halberstadt, N.; Drabbels, M. *J. Phys. Chem. A* **2015**, *119*, 6033–6044.
- von Vangerow, J.; John, O.; Stienkemeier, F.; Mudrich, M. *J. Chem. Phys.* **2015**, *143*, 034302.
- Droppelmann, G.; Bünermann, O.; Schulz, C. P.; Stienkemeier, F. *Phys. Rev. Lett.* **2004**, *93*, 0233402.
- Reho, J.; Higgins, J.; Lehmann, K. K.; Scoles, G. *J. Chem. Phys.* **2000**, *113*, 9694–9701.
- Mudrich, M.; Doppelmann, G.; Claas, P.; Schulz, C.; Stienkemeier, F. *Phys. Rev. Lett.* **2008**, *100*, 023401.
- Mudrich, M.; Stienkemeier, F. *Int. Rev. Phys. Chem.* **2014**, *33*, 301–339.

- (19) Bruder, L.; Mudrich, M.; Stienkemeier, F. *Phys. Chem. Chem. Phys.* **2015**, *17*, 23877–23885.
- (20) Ziemkiewicz, M. P.; Neumark, D. M.; Gessner, O. *Int. Rev. Phys. Chem.* **2015**, *34*, 239.
- (21) Masson, A.; Poisson, L.; Gaveau, M.-A.; Soep, B.; Mestdagh, J.-M.; Mazet, V.; Spiegelman, F. *J. Chem. Phys.* **2010**, *133*, 054307.
- (22) Schulz, C. P.; Claas, P.; Stienkemeier, F. *Phys. Rev. Lett.* **2001**, *87*, 153401.
- (23) Giese, C.; Mullins, T.; Grüner, B.; Weidemüller, M.; Stienkemeier, F.; Mudrich, M. *J. Chem. Phys.* **2012**, *137*, 244307.
- (24) Fechner, L.; Grüner, B.; Sieg, A.; Callegari, C.; Ancilotto, F.; Stienkemeier, F.; Mudrich, M. *Phys. Chem. Chem. Phys.* **2012**, *14*, 3843.
- (25) Piffrader, A.; Allard, O.; Auböck, G.; Callegari, C.; Ernst, W.; Huber, R.; Ancilotto, F. *J. Chem. Phys.* **2010**, *133*, 164502.
- (26) Loginov, E.; Drabbels, M. *J. Phys. Chem. A* **2014**, *118*, 2738–2748.
- (27) Grüner, B.; Schlesinger, M.; Heister, P.; Strunz, W. T.; Stienkemeier, F.; Mudrich, M. *Phys. Chem. Chem. Phys.* **2011**, *13*, 6816–6826.
- (28) Eppink, A. T. J. B.; Parker, D. H. *Rev. Sci. Instrum.* **1997**, *68*, 3477.
- (29) Ancilotto, F.; DeToffol, G.; Toigo, F. *Phys. Rev. B: Condens. Matter Mater. Phys.* **1995**, *52*, 16125–16129.
- (30) Stienkemeier, F.; Higgins, J.; Ernst, W. E.; Scoles, G. *Phys. Rev. Lett.* **1995**, *74*, 3592–3595.
- (31) Bünermann, O.; Droppeleman, G.; Hernando, A.; Mayol, R.; Stienkemeier, F. *J. Phys. Chem. A* **2007**, *111*, 12684.
- (32) von Vangerow, J.; Sieg, A.; Stienkemeier, F.; Mudrich, M.; Leal, A.; Mateo, D.; Hernando, A.; Barranco, M.; Pi, M. *J. Phys. Chem. A* **2014**, *118*, 6604–6614.
- (33) Dick, B. *Phys. Chem. Chem. Phys.* **2014**, *16*, 570–580.
- (34) Mudholkar, G. S.; Hutson, A. D. *J. Stat. Plan. Inference* **2000**, *83*, 291–309.
- (35) Ancilotto, F.; Barranco, M.; Caupin, F.; Mayol, R.; Pi, M. *Phys. Rev. B: Condens. Matter Mater. Phys.* **2005**, *72*, 214522.
- (36) Pascale, J. *Phys. Rev. A: At., Mol., Opt. Phys.* **1983**, *28*, 632–644.
- (37) Patil, S. H. *J. Chem. Phys.* **1991**, *94*, 8089–8095.
- (38) Brühl, F. R.; Trasca, R. A.; Ernst, W. E. *J. Chem. Phys.* **2001**, *115*, 10220–10224.
- (39) Auböck, G.; Nagl, J.; Callegari, C.; Ernst, W. E. *Phys. Rev. Lett.* **2008**, *101*, 035301.
- (40) Theisen, M.; Lackner, F.; Ernst, W. E. *J. Phys. Chem. A* **2011**, *115*, 7005–7009.

4.2 Desorption dynamics of RbHe exciplexes

How does a Rb atom, excited to the $5p\ ^2\Pi_{3/2}$ state, detached from a droplets surface—as the experiments show—even though this is not predicted by TD-DFT calculations? That is the main question that led to this work. Upon photo-excitation of Rb to the $5p\ ^2\Pi_{3/2}$ state, a He atom may be attached to it forming a HeRb exciplex; this cannot happen if Rb is excited to the $5p\ ^2\Pi_{1/2}$ state because it finds a barrier preventing exciplex formation.

In the gas phase, a HeRb $5p\ ^2\Pi_{1/2}$ exciplex can be formed if there is enough kinetic energy for Rb^* to overcome the potential barrier; alternatively, the collision of the HeRb $5p\ ^2\Pi_{3/2}$ exciplex with another atom or complex might relax the Rb^* atom from the $5p\ ^2\Pi_{3/2}$ to the $5p\ ^2\Pi_{1/2}$ state, overcoming the barrier as the potential wells for both states are at similar Rb-He distances. In the condensed (droplet) phase at 0.4 K temperature, none of these mechanisms are active to explain the formation of HeRb $5p\ ^2\Pi_{1/2}$ exciplexes and their potential ejection.

However, a possible mechanism for this is non-radiative de-excitation from the $5p\ ^2\Pi_{3/2}$ to the $5p\ ^2\Pi_{1/2}$ that populates the later state and leaves the Rb^* atom with enough kinetic energy so as to be ejected. Notice from the figure that the minimum of the $5p\ ^2\Pi_{3/2}$ potential is 12683 cm⁻¹, and that of the $5p\ ^2\Pi_{1/2}$ potential is at 12518 cm⁻¹; the value of this potential at the barrier is 12611 cm⁻¹. Thus, non-radiative de-excitation of the Rb^* atom may add to its original kinetic energy of up to 165 cm⁻¹. It is worth noting that it will be ejected in the $5p\ ^2\Pi_{1/2}$ state, and not in the $5p\ ^2\Pi_{3/2}$ it was previously photo-excited.

This publication contains a extension of our combined experimental and theoretical investigation presented in the previous section. Here we focus on the formation of free RbHe-exciplex molecules from laser-excited Rb-doped He nanodroplets through the mechanism of electronic spin relaxation. The role of relaxation of internal degrees of freedom of the RbHe exciplex in the desorption process has not been explicitly addressed.

ARTICLE TYPE

Cite this: DOI: 10.1039/xxxxxxxxxx

Desorption dynamics of RbHe exciplexes off He nano-droplets induced by spin-relaxation

François Coppens,^{a,†} Johannes von Vangerow,^{b,†} Manuel Barranco,^{a,c,d} Nadine Halberstadt,^a Frank Stienkemeier,^b Martí Pi^{c,d}, and Marcel Mudrich^e

Received Date

Accepted Date

DOI: 10.1039/xxxxxxxxxx

www.rsc.org/journalname

Doped He nanodroplets are ideal model systems to study the dynamics of elementary photochemical processes in heterogeneous nanosystems. Here we present a combined experimental and theoretical investigation of the formation of free RbHe exciplex molecules from laser-excited Rb-doped He nanodroplets. Upon excitation of a droplet-bound Rb atom to the $5p_{3/2}$ $^2\Pi_{3/2}$ -state, a stable RbHe exciplex forms within about 20 ps. Only due to $^2\Pi_{3/2} \rightarrow ^2\Pi_{1/2}$ spin-relaxation does the RbHe exciplex detach from the He droplet surface with a half life of about 700 ps, given by the spin-relaxation time and the coupling of spin and translational degrees of freedom.

1 Introduction

Understanding the photochemistry of condensed phase systems and surfaces is essential in many research areas, such as atmospheric sciences¹ and photocatalysis². However, complex couplings between electronic and motional degrees of freedom of various subunits of the system often present a major challenge^{3–5}. Moreover, the heterogeneity of multi-component solid or liquid systems and experimental difficulties in precisely preparing the sample and reproducing measurements tend to make it hard to unravel specific elementary reactions. In this respect, He nanodroplets doped with single atoms or well-defined complexes are ideal model systems for studying photodynamical processes in the condensed phase, both experimentally and theoretically. Due to their ultralow temperature (0.37 K) and their quantum fluid nature, He nanodroplets have a homogeneous density distribution and dopant particles aggregate into cold clusters mostly inside the droplets^{6,7}. Only alkali metal atoms and small clusters are attached to He droplets in loosely bound dimple-like states at the droplet surface^{8–15}.

While He nanodroplets are extremely inert and weakly-perturbing matrices for spectroscopy of embedded atoms and

molecules in their electronic ground state, a rich photochemical dynamics is initiated upon photoexcitation or photoionization^{16,17}. This includes electronic relaxation^{18–21}, the ejection of the dopant out of the droplet^{22–29}, chemical reactions within the dopant complex^{30–32}, and even among the dopant and the surrounding He^{23,33–42}.

As a general trend, electronically excited dopant atoms and small molecules tend to be ejected out of He droplets either as bare particles or with a few He atoms attached to them^{18,43–45}. In particular, all atomic alkali species promptly desorb off the droplet surface, the only exceptions being Rb and Cs atoms in their lowest excited states^{46,47}. The dynamics of the desorption process has recently been studied at an increasing level of detail^{19,24,26,48}, including time-resolved experiments and simulations^{27,29}. The focus has been on the competing processes of desorption of the dopant induced by laser excitation, and the dopant falling back into the He droplet upon photoionization. The latter occurred at short pump-probe delay times when the distance between the photoion and the droplet was short enough for ion-He attraction to be effective.

The aim of this work is to extend our joint experimental and theoretical study of the photodynamics of Rb-doped He nanodroplets to RbHe exciplexes^{26,29}. The simultaneous effect of pair-wise Rb-He attraction and repulsion of Rb from the He droplet as a whole results in an intricate dynamics, and interpretations have remained somewhat ambiguous with respect to the exciplex formation mechanism and characteristic time scale, as well as the origin of free exciplexes detached from the He droplets^{19,29,33,34,36,37}. In particular the role of relaxation of internal degrees of freedom of the RbHe exciplex in the desorption process has not been explicitly addressed^{49,50}. Here, we discuss in detail the interplay of the RbHe formation dynamics, the

^a Laboratoire des Collisions, Agrégats, Réactivité, IRSAMC, Université Toulouse 3- Paul Sabatier, CNRS UMR 5589, 118 route de Narbonne, F-31062 Toulouse Cedex 09, France

^b Physikalisches Institut, Universität Freiburg, Hermann-Herder-Str. 3, 79104 Freiburg, Germany

^c Institute of Nanoscience and Nanotechnology (IN2UB), Universitat de Barcelona, Diagonal 645, 08028 Barcelona, Spain

^d Departament FQA, Facultat de Física, Universitat de Barcelona. Diagonal 645, 08028 Barcelona, Spain

^e Department of Physics and Astronomy, Aarhus University, Ny Munkegade 120, Aarhus 8000 C, Denmark

[†] F. Coppens and J. von Vangerow contributed equally to this work.

* E-mail: mudrich@phys.au.dk

RbHe desorption off the He droplet surface, and the fall-back of $[RbHe]^+$ created by photoionization in femtosecond pump-probe experiments^{27,29,34}. We find that electronic spin-relaxation is the main process driving the desorption of RbHe off the He droplet.

This paper is accompanied by animations showing the real-time dynamics of the Rb-He droplet complex for several excited states and for the scenario of time-delayed spin-relaxation. These animations are presented in the supplementary material S1-S4.

2 Methods

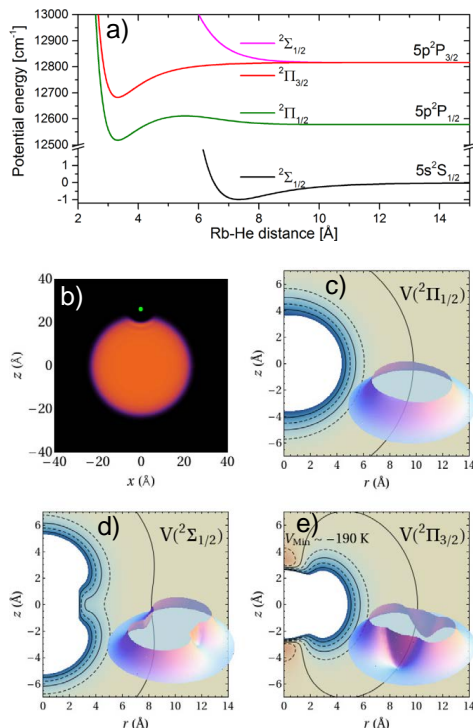


Figure 1 a) Rb-He pair potentials used in this work^{51,52}. The potentials correlating to the Rb excited 5p²P-state are split due to spin-orbit coupling. b) Equilibrium dimple configuration of Rb in the ground state in the x - z -plane (represented by a green dot). Panels c)-e) display the two-dimensional Rb-He potential surfaces in cylindrical coordinates (r , z) corresponding to this configuration, with the Rb atom located at the origin. Regions where the potentials are attractive (repulsive) are represented in pink (blue). The outermost equidensity line corresponds to zero potential. Notice that in panel e) the 5p²Π_{3/2} potential presents a deep minimum of about 190 K on the z -axis. The 5p²Π_{1/2} and 5p²Σ_{1/2} potentials [c) and d)] have shallow attractive minima of about 1 K depth at a distance of ~ 10 Å, not represented in the figure. Reprinted from Int. Rev. Phys. Chem. **36**, 621-707 (2017) with permission from Taylor & Francis Ltd, <http://www.tandfonline.com>.

2.1 Theoretical approach

During the last decade, the density functional theory (DFT) approach has emerged as an accurate and flexible tool to describe the statics and dynamics of doped helium droplets. The DFT activity carried out in this field has been summarized in two reviews^{10,17}. In the following we give the basic details how the method has been applied to the present problem, and refer the reader to Refs.^{17,25} for the details.

In this work, we describe the interaction of a Rb atom with a He droplet composed of $N = 1000$ He atoms. Due to its large mass, Rb is treated as an external field in the statics, and as a classical particle in the dynamics. The impurity-droplet interaction is described in a pairwise approximation, and the ground state of the droplet-impurity system is found by solving the Euler-Lagrange equation

$$\left\{ -\frac{\hbar^2}{2m} \nabla^2 + \frac{\delta \mathcal{E}_c}{\delta \rho} + V_X(|\mathbf{r} - \mathbf{r}_I|) \right\} \Psi_0(\mathbf{r}) = \mu \Psi_0(\mathbf{r}), \quad (1)$$

where $\Psi_0(\mathbf{r}) = \sqrt{\rho(\mathbf{r})}$ is the He effective wave function, with $\rho(\mathbf{r})$ being the atom density; μ is the He chemical potential, and V_X is the Rb-He pair potential⁵¹. The correlation energy density functional \mathcal{E}_c has been taken from Ref.⁵³. The results presented in this work are obtained using the 4He-DFT BCN-TLS computing package⁵⁴. We work in Cartesian coordinates using a space step of 0.4 Å. In the dynamics calculations we use a time step of 0.5 fs.

Once the droplet-equilibrium configuration, shown in Figure 1 b), is determined, the 5p \leftarrow 5s absorption spectrum is obtained using the DF sampling method⁵⁵. To this end, the diatomic-in-molecule model is used for the droplet-Rb interaction in the excited 5p²P state⁵⁶. The 5p²Σ and 5p²Π Rb-He pair potentials, shown in Figure 1 a), are taken from Refs.^{51,52}. The resulting simulated absorption dipole spectrum of the RbHe₁₀₀₀ complex, shown in Figure 6 of Ref.¹⁷, is in good agreement with the experimental and previous calculations^{34,57}.

Figs. 1 c)-e) show the direction-dependent potentials (spin-orbit term included) which, within the diatomic-in-molecule approach, enter the dynamics simulations of Rb in the 5p²P-correlated states. In the course of the time evolution of the system, the He atoms have a natural tendency to adapt to these potential surfaces, either going away if the potential is mostly repulsive as in the Σ_{1/2}-state [Figure 1 d)], or to evolve to a bound RbHe exciplex configuration in the Π_{3/2}-state [e)] featuring local minima at ($r = 0$, $z = \pm 3.5$ Å). In the Π_{1/2}-state [c)], one may also expect the formation of RbHe exciplexes given the potential minimum in the RbHe pair potential around 3.2 Å [a)]. However, RbHe formation is hampered by a potential barrier which cannot be overcome at the low temperature of the He droplet^{34,58}.

2.2 Experimental setup

The setup used for the present experiments has been described previously^{26,27}. Briefly, a beam of He droplets with an average diameter of 10 nm is produced by continuously expanding pressurized He (50 bar) out of a cold nozzle (diameter 5 μm, temperature 17 K). The He droplets are doped with one Rb atom on

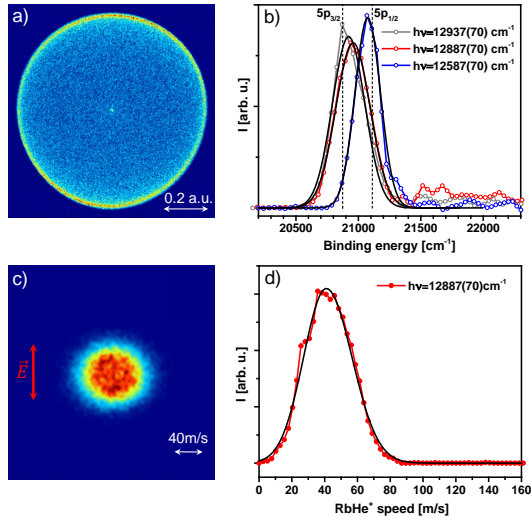


Figure 2 Raw velocity-map images of photoelectrons a) and of $[RbHe]^+$ photoions c) recorded at $\lambda = 776\text{ nm}$ (12887 cm^{-1}) for a long pump-probe delay time of 2 ns. The red vertical arrow indicates the laser polarization. b) Electron binding energy spectra inferred from the image shown in a), from an image recorded at $\lambda = 773\text{ nm}$ (12937 cm^{-1}), and from an image at $\lambda = 794\text{ nm}$ (12587 cm^{-1}). d) $[RbHe]^+$ photoion speed distribution inferred from c).

average by pickup of Rb atoms inside a heated vapor cell (length 1 cm, temperature 85°C).

An amplified Ti:Sa laser system generates pulses of 100 fs duration at a repetition rate of 5 kHz. The center wavelength is tunable in the near infrared (NIR) region. The FWHM of the spectral laser profile is 140 cm^{-1} . Light in the visible range (VIS) is generated by frequency doubling. The pulses are split and separated in time in a Mach-Zehnder type interferometer. The droplet-perturbed Rb 5p states are probed by a two-color NIR+VIS pump-probe resonant photoionization scheme. The NIR pulses are strongly attenuated to avoid the excitation of higher lying states by multi-photon processes. The polarizations of the two laser pulses are parallel to one another and parallel to the detector surface.

Photoions and photoelectrons are detected by a velocity-map imaging (VMI) spectrometer operated in single-particle detection mode^{19,26,59,60}. Mass-selected ion VMIs are recorded by time-gating the imaging detector according at the specific flight times of either Rb^+ or $[RbHe]^+$ ions. One VMI is recorded for each value of the pump-probe delay time. Both Rb^+ ion images and electron images contain background contributions from resonant ionization of free Rb atoms effusing out of the doping cell. In order to efficiently subtract these contributions, background images are recorded at each pump-probe delay using a chopper that periodically interrupts the He droplet beam at a frequency of 15 Hz. The acquired background and signal+background images are inverse Abel transformed to infer the full three-dimensional velocity

distributions^{61,62}. The resulting spectra obtained from angular integration are normalized to the number of counts and subtracted from each other, where we exploit the additivity of the inverse Abel transformation⁶³.

3 Time-resolved imaging spectroscopy

Typical experimental total electron and $[RbHe]^+$ ion VMIs recorded at a center wavelength of the pump laser pulse $\lambda = 776\text{ nm}$ (12887 cm^{-1}) and a pump-probe delay of 2 ns are shown in Figure 2 a) and c), respectively. The corresponding electron binding energy distribution and ion speed distribution inferred from these images are presented in Figure 2 b) and d), respectively. In addition, Figure 2 b) contains photoelectron spectra measured at $\lambda = 773$ (12937 cm^{-1}) and at $\lambda = 794\text{ nm}$ (12594 cm^{-1}). Note that the photoelectron spectra in Figure 2 b) are rescaled in terms of electron binding energies $E_b = h\nu_2 - T_e$, where $h\nu_2 = 2hc/\lambda$ denotes the photon energy of the ionizing laser pulse and T_e is the measured electron kinetic energy. The dashed vertical lines represent E_b for free Rb atoms in their $5p_{1/2}$ and $5p_{3/2}$ -states.

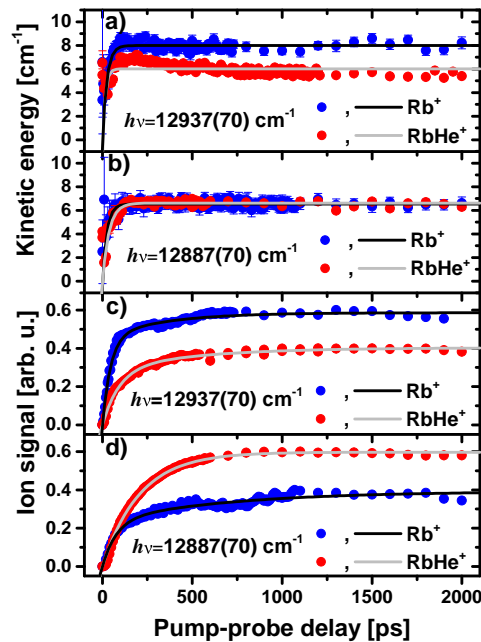


Figure 3 Rb^+ and $[RbHe]^+$ ion kinetic energies [a) and b)] and signal yields [c) and d)] recorded at laser wavelengths $\lambda = 773\text{ nm}$ [12937 cm^{-1} , a) and c)] and $\lambda = 776\text{ nm}$ [12887 cm^{-1} , b) and d)]. The smooth gray and black lines are fit curves (see text for details).

3.1 Photoion imaging

The $[RbHe]^+$ ion distribution [Figure 2 c)] is a round spot with a flat intensity distribution and a slight elongation in x -direction

(perpendicular to the laser polarization). The corresponding speed distribution [Figure 2 d)] is broad and nearly symmetric. The black line depicts a skewed Gaussian distribution fitted to the data⁶⁴. This fit is applied repeatedly to each speed distribution measured at various pump-probe delays in order to trace the evolution of the most probable kinetic energy, see Figure 3 a) and b). The yields of ions, shown in Figure 3 c) and d), are obtained by summing over ion counts contained in each image. Blue and red symbols show the results for Rb⁺ and [RbHe]⁺ ions, respectively. Both kinetic energies and ion yields monotonously increase within 50–500 ps, with a slight overshoot at $\lambda = 773$ nm (12937 cm⁻¹) [Figure 3 a)]. This increase results from the competing processes of desorption of the excited neutral Rb and RbHe species, and falling back of the Rb⁺ and [RbHe]⁺ photoions into the He droplet due to attractive Rb⁺-He interactions, as discussed in Refs.^{27,29}. By comparing the experimental data with TD-DFT simulations, we concluded that the 5p-correlated states of Rb and RbHe desorb off He droplets not purely impulsively, but in a more complex evaporation-like process²⁹. The overshoot of speeds in Figure 3 a) is likely due to weak long-range attractive forces acting between the desorbing Rb and RbHe and the He droplet surface, which slightly slow down the relative motion in the later stage of desorption.

The data in Figure 3 a) are measured at $\lambda = 773$ nm (12937 cm⁻¹), which corresponds to the excitation of the RbHe complex into the 5pΣ_{1/2}-state, with some contribution of the 5pΠ_{3/2}-state due to overlapping absorption bands and due to the broad spectral profile of the laser^{9,34,65}. The 5pΣ_{1/2}-state is the most repulsive one out of the three states studied here. Accordingly, the asymptotic most probable speed of Rb⁺ reached at long delays is comparatively high, $\hat{v} = 85$ m/s, corresponding to a kinetic energy of 8 cm⁻¹, whereas for [RbHe]⁺ we find $\hat{v} = 40$ m/s (5.8 cm⁻¹). Since the diatomic 5pΣ_{1/2} RbHe potential is purely repulsive [Figure 1 a)], this component of the excited population results in the desorption of neat Rb atoms. Accordingly, the yield of detected Rb⁺ ions exceeds that of [RbHe]⁺ ions by about a factor 1.5.

At $\lambda = 776$ nm (12887 cm⁻¹), a higher contribution of the 5pΠ_{3/2}-state is excited, which efficiently forms RbHe exciplexes³⁴. Thus, the yield of [RbHe]⁺ ions is higher than that of Rb⁺ by a factor 1.5. The Rb⁺ and [RbHe]⁺ asymptotic most probable speed is $\hat{v} = 42$ m/s (6.3 cm⁻¹), close to that of [RbHe]⁺ at $\lambda = 773$ nm (12937 cm⁻¹). At $\lambda = 794$ nm (12595 cm⁻¹), the 5pΠ_{1/2}-state of the Rb-He droplet complex is excited (not shown), and no [RbHe]⁺ ions are detected. Therefore we have recorded only Rb⁺ ion images at that wavelength²⁹. Here, the Rb⁺ asymptotic most probable speed is lowest, $\hat{v} = 38$ m/s (5.1 cm⁻¹), because dopant-He repulsion is weak.

The transient kinetic energies measured at all laser wavelengths rise within a delay time of about 50 ps. The characteristic energy rise time (to half value), τ_E^i , and the asymptotic ion kinetic energy E_∞^i , are determined by fitting the data with an exponential function

$$E^I(t) = E_\infty^i \cdot \left(1 - \exp[-\ln 2 \cdot t / \tau_E^i]\right). \quad (2)$$

The resulting fit parameters are summarized in table 1.

The ion yields increase with pump-probe delay slightly more slowly than the ion kinetic energies, where the Rb⁺ ion signal rises faster than the [RbHe]⁺ ion signal at short delays. The initial fast rise of the Rb⁺ ion yield flattens out at delays around 100 ps and continues to rise slightly up to about 2 ns. The [RbHe]⁺ ion yields show a similar initial fast rise followed by a more pronounced slow increase that levels off somewhat earlier. Therefore, for fitting the Rb⁺ and [RbHe]⁺ ion yield data we use a biexponential function,

$$I(t) = A_1^i \cdot \left(1 - \exp[-\ln 2 \cdot t / \tau_1^i]\right) + A_2^i \cdot \left(1 - \exp[-\ln 2 \cdot t / \tau_2^i]\right), \quad (3)$$

where (A_1^i, τ_1^i) and (A_2^i, τ_2^i) parametrize the fast and the slow signal rise, respectively.

While neither the Rb⁺ and [RbHe]⁺ asymptotic energies E_∞^i , nor the energy rise times τ_E^i depend much on λ , the rise times of ion yields of RbHe⁺, τ_E^i , clearly decrease monotonically with decreasing λ (increasing photon energy) by a factor 6, ranging from 186 ps at $\lambda = 780$ nm (12821 cm⁻¹) to 32 ps at $\lambda = 773$ nm (12937 cm⁻¹). The trend that the dynamics proceeds faster with decreasing λ (increasing photon energy) is partly due to the increasingly repulsive dopant-He interaction and agrees with our previous findings^{27,29}. However, the observation that the ion yields rise more slowly than the ion kinetic energies cannot be understood with the concept of impulsive desorption and fall-back. In that model, ion kinetic energies should be affected by ion-He attraction up to long delay times exceeding the fall-back time. Note that in previous experiments on the Rb 6p-state, where desorption proceeded impulsively, ion energies indeed increased more slowly than ion yields²⁹. Therefore we take our current finding ($\tau_1^i, \tau_2^i > \tau_E^i$) as a further indication for a non-impulsive, evaporation-like desorption mechanism.

Furthermore, from our analysis of the VMIs we obtain information about the anisotropy of the ion angular distribution, characterized by the parameter β ⁶⁶. For [RbHe]⁺ at long delay times we find $\beta = -0.39(1)$ when a higher contribution of the Π_{3/2}-state is excited at $\lambda = 776$ nm (12887 cm⁻¹). At $\lambda = 773$ nm (mainly Σ_{1/2}-excitation), the anisotropy becomes slightly positive, $\beta = 0.13(1)$. The corresponding values for the Rb⁺ ion distributions are $\beta = -0.16(1)$ and $\beta = 0.17(1)$, respectively. While the signs of the β -values are in accordance with the symmetries of the pseudo-diatom states (ideal perpendicular Σ → Π-transition in a diatomic implies $\beta = -1$, parallel Σ → Σ-transition implies $\beta = 2$), the absolute values are much smaller. On the one hand, this is due to the mixing of excited Σ_{1/2} and Π_{3/2}-states. On the other hand, the desorption process is more complex than direct dissociation of a diatomic molecule. We recall that the β -values came much closer to the ideal values in the case of excitation of Rb to the high-lying 6p-correlated states, where desorption proceeded more impulsively^{19,26,29}.

We mention that in earlier pump-probe experiments, significantly different Rb⁺ and [RbHe]⁺ ion yield curves were measured³⁶. However, in those experiments, NIR light emitted directly from a mode-locked titanium:sapphire laser was used at

λ [nm]	State	Ion	E_∞^i [1/cm]	τ_E^i [ps]	A_1^i	τ_1^i [ps]	A_2^i	τ_2^i [ps]	β
773	$\Sigma_{1/2}/\Pi_{3/2}$	Rb ⁺	8.0(1)	17(1)	0.45(2)	32(1)	0.14(2)	234(33)	0.17(1)
		[RbHe] ⁺	6.0(1)	10(2)	0.17(2)	41(6)	0.22(2)	178(17)	0.13(1)
776	$\Pi_{3/2}/\Sigma_{1/2}$	Rb ⁺	6.5(3)	17(1)	0.24(2)	53(5)	0.16(2)	490(104)	-0.16(1)
		[RbHe] ⁺	6.6(3)	26(1)	0.60(1)	143(2)	0.00(1)	-	-0.39(1)
780	$\Pi_{3/2}$	[RbHe] ⁺	6.3(1)	24(2)	0.95(1)	186(1)	0.00(1)	-	0.35(1)

Table 1 Time constants and energies inferred from pump-probe measurements of Rb⁺ and [RbHe]⁺ ion yields at the 5p $\Sigma_{1/2}$ and 5p $\Pi_{3/2}$ -states of the Rb-He droplet complex, obtained from fits with equations (2) and (3), see Figure 3.

a pulse repetition rate of 80 MHz. Therefore, a large fraction of the ion signals actually stemmed from Rb and RbHe that had been desorbed off the droplets by preceding pulse pairs. Thus, the observed pump-probe transients may have reflected the internal dynamics of free RbHe instead of the dynamics of the Rb-He droplet interaction. Besides, near-resonant two-photon excitation of higher lying states correlating to the Rb 5d-level were probably involved in the observed dynamics. This raises some doubts as to the conclusions of those previous experiments in terms of exciplex formation times^{29,36}. Further studies are needed to clarify this issue.

From the overall resemblance of the [RbHe]⁺ and Rb⁺ kinetic energy curves and ion yields in the present study one is tempted to conclude that RbHe exciplex formation is fast and desorption of RbHe off the He droplet surface proceeds essentially in the same way as for neat Rb atoms. However, the more pronounced biexponential rise of [RbHe]⁺ ion yields, as well as complementary delay-dependent photoelectron measurements, and numerical simulations presented in the following sections will show that the desorption dynamics of RbHe exciplexes actually is more intricate than that of Rb atoms.

3.2 Photoelectron imaging

The photoelectron spectra recorded at the three characteristic laser wavelengths λ [Figure 2 b)] exhibit pronounced peaks around the Rb 5p $_{1/2}$ and 5p $_{3/2}$ atomic binding energies, $E_{5p1/2}$ and $E_{5p3/2}$, respectively. Both the peak position and the peak width significantly vary with λ , as inferred from fits to the data with a Gaussian function, depicted as smooth lines. The resulting peak positions relative to $E_{5p1/2}$ and $E_{5p3/2}$ are plotted in Figure 4 a), b), respectively. Figure 4 c) shows the Gaussian peak widths σ . For reference, the open symbols represent the peak positions measured for the Rb atomic background. The scatter of data points around the literature value (grey horizontal line) indicates the level of precision of our measurements.

The excess energies for the 5p $\Sigma_{1/2}$ and 5p $\Pi_{3/2}$ -states, $E_b - E_{5p1/2,5p3/2}$ shown in Figure 4 b), exhibit a fast decay (E_1^e , τ_1^e) above and a slow decay (E_2^e , τ_2^e) below $E_{5p3/2}$ (horizontal line at $y = 0$). Therefore, these data are fitted with a biexponential decay function

$$E^e(t) = E_1^e \cdot \exp(-\ln 2 \cdot t / \tau_1^e) + E_2^e \cdot \exp(-\ln 2 \cdot t / \tau_2^e) + E_\infty^e. \quad (4)$$

Here, E_∞^e denotes the asymptotic energy value at long delay times. When exciting the 5p $\Pi_{1/2}$ -state at $\lambda = 794$ nm (12594 cm⁻¹),

the transient droplet correlated peak position remains constant within the experimental scatter. Therefore, merely the mean value E_1^e is determined. The resulting energies and time constants are summarized in table 2. The increasing peak widths in the cases of $\lambda = 773$ (12937 cm⁻¹) and 776 nm (12887 cm⁻¹) are fitted by the simple exponential function given by Eq. (2).

The fact that the droplet-related photoelectron energy E_1^e for the $\Pi_{1/2}$ -state is constant but shifted with respect to the atomic value indicates that most of the Rb atoms remain attached to the droplet surface upon electronic excitation, in accordance with previous studies^{46,67}. Thus, the slowly rising Rb⁺-ion signal measured at that wavelength, indicative for excited Rb desorption, reflects only a small fraction of Rb atoms, most of which actually remain bound to the droplets. The measured up-shift of electron energy of $E_1^e = 33(2)$ cm⁻¹ is attributed to a lowering of the ionization threshold induced by the He environment. This value is in reasonable agreement with previous measurements, where the ionization threshold was found to be lowered by 50(10) cm⁻¹ at comparable conditions⁶⁷.

The similar dynamics of electron energies and ion yields for the $\Sigma_{1/2}$ and $\Pi_{3/2}$ -states, a biexponential evolution with a fast component (tens of ps) and a slow component (hundreds of ps), are taken as a confirmation that two distinct relaxation processes occur simultaneously. The fast process – prompt desorption of excited Rb off the He droplet – is associated mainly with the $\Sigma_{1/2}$ -component of the excited state, whereas the $\Pi_{3/2}$ -component undergoes slow relaxation. The latter will be discussed in the following sections. Deviations of the time constants τ_1^e vs. τ_1^i , and τ_2^e vs. τ_2^i , are mainly due to the different nature of the observables. Both ion yields and speeds are affected by the dynamics occurring after the probe-ionization, whereas electron spectra probe the electronic state (affected by the He configuration around the Rb) at the moment of ionization. In particular, ion signals provide information only about that fraction of ions that eventually detach from the He droplets, whereas electron signals are measured for all photoionization events, including those where the ion falls back into the droplet; in this respect the electron spectra are the better probes of the full dynamics, with the restriction that we cannot distinguish between the final products (Rb, RbHe, and Rb attached to a He droplet).

We mention that at $\lambda = 776$ nm (12887 cm⁻¹, $\Pi_{3/2}$ -state), an extended low intensity distribution is present in the spectrum of Figure 2 b) at higher electron binding energies $\geq 21,500$ cm⁻¹ (lower electron kinetic energies). We attribute this component to elastic scattering of photoelectrons with He atoms as they prop-

λ [nm]	State	E_1^e [1/cm]	τ_1^e [ps]	E_2^e [1/cm]	τ_2^e [ps]	E_∞^e [1/cm]
773	$\Sigma_{1/2}/\Pi_{3/2}$	32(2)	15(2)	63(4)	683(130)	-53(5)
776	$\Pi_{3/2}/\Sigma_{1/2}$	36(2)	13(2)	110(4)	709(70)	-96(5)
794	$\Pi_{1/2}$	33(2)	-	-	-	-

Table 2 Time constants and energies inferred from fits of equation (4) to the transient photoelectron energies (Figure 4).

agate through the He droplet. Low-energy features in photoelectron spectra due to electron-He scattering have been observed before, in particular when using one-photon ionization.^{68–71} The fact that this feature is most pronounced for the $\Pi_{3/2}$ -excitation may be related to the more abundant formation of RbHe exciplexes which enhances the electron-He scattering probability.

4 TD-DFT dynamics simulation

Time-dependent density functional theory (TD-DFT) simulations are carried out as thoroughly described in Refs.^{17,25}. Starting with the Rb-droplet equilibrium configuration, the dynamics is initiated by a “vertical DFT transition” into the excited state. This is realized by suddenly switching from the potential energy surface of the Rb-He droplet ground state to that of the Rb-He excited state. The subsequent evolution of the system can be followed in real-time, as illustrated by the series of snapshots of the He density distribution (red area) and the position of the Rb atom (green and magenta dots) in Figure 5. The animated version of this evolution is shown in the Video S4 in the supplementary material. Here, excitation of the $5p\Pi_{3/2}$ -state at $t = 0$ is followed by relaxation to the $5p\Pi_{1/2}$ -state at $t = 60$ ps. This time has been chosen rather arbitrarily; the only constraint is that it should be large enough to allow the exciplex around the $5p\Pi_{3/2}$ -state to fully develop, see Figure 7 below.

4.1 Direct ejection of bare Rb atoms from the $^2\Sigma_{1/2}$ and $^2\Pi_{1/2}$ -states

From these data we now infer the relevant quantities to compare with the experimental results, such as the kinetic energy of the Rb atom relative to the droplet, the occurrence of He density attached to Rb which we identify with the formation of an exciplex, and the transient interaction energy of the neutral and ionized Rb atom with the surrounding He. The latter is related to the kinetic energy of a photoelectron created in a time-delayed photoionization process.

Figure 6 collects our results for the dynamics of the Rb atom excited to the droplet-perturbed states correlating to the atomic $5p$ -state. For the $\Sigma_{1/2}$ and $\Pi_{1/2}$ -states, the velocities (dashed lines) and kinetic energies (solid lines) feature a rapid increase to reach a maximum at time $t = 2.5$ ps after excitation, followed by a drop due to long-range attractive forces acting on the desorbing Rb atom. The asymptotic values are reached for $t > 50$ ps. When exciting the $\Pi_{3/2}$ -state, the Rb-velocity features a damped oscillation around zero indicating that the Rb atom remains bound to the He droplet surface. The following conclusions can be drawn from these results:

(i) Rb excited to the $5p\Sigma_{1/2}$ -state detaches from the droplet

reaching an asymptotic kinetic energy of 13 cm^{-1} . This value deviates from the experimental one (8.0 cm^{-1}) due to contributions of $\Pi_{3/2}$ -excitation to the experimental signal. Despite of the shallow local minima in the corresponding Rb-He droplet potential surface [1 c)], no binding of He density to the departing Rb atom occurs. This finding is in accordance with experiments^{19,34,36}, where mostly free Rb atoms were detected following excitation at wavelengths $\lambda < 774 \text{ nm}$ ($> 12929 \text{ cm}^{-1}$). The full evolution of the excited Rb-He nanodroplet complex is shown in the Video S1 in the supplementary material.

(ii) Rb excited to the $5p\Pi_{1/2}$ -state also detaches from the He droplet, but the asymptotic kinetic energy is much lower, 2.8 cm^{-1} . For this case, the evolution is shown in the Video S2 in the supplementary material. This value of the Rb kinetic energy again deviates from the experimental one (5.1 cm^{-1}), but the trend that desorption of the less repulsive $\Pi_{1/2}$ -state yields a lower energy than for the $\Sigma_{1/2}$ -state is well reproduced. The potential well at short distance $\sim 3 \text{ \AA}$ would in principle support a stable RbHe exciplex. However, at the low temperature of the He droplet, exciplex formation is hindered by a potential barrier located at $\sim 5 \text{ \AA}$, between the well and the range where the $5p\Pi_{1/2}$ -state is populated by excitation from the $5s\Sigma_{1/2}$ -ground state (7 \AA).^{33,34,58}

We recall that in previous experiments using narrow-band excitation of the low energy edge of the $\Pi_{1/2}$ -resonance, it was observed that Rb and Cs dopants remained attached to the He droplet surface.⁴⁶ However, our simulations correspond to the excitation at the peak of the resonance, where free Rb atoms are also observed in the experiment. Thus, our simulations are not in conflict with the experimental findings. Note that Quantum Monte Carlo (QMC) calculations carried out for this state⁷² yielded a weakly bound Rb in a shallow dimple. Had we carried out a static DFT relaxation, we would also have found a bound structure, due to the shallow minimum on the Rb-He droplet potential surface. However, in the dynamical TD-DFT simulation this minimum is too shallow to retain the departing Rb atom.

(iii) In our simulation we find that Rb excited to the $5p\Pi_{3/2}$ -state remains bound to the He droplet surface where it forms a RbHe exciplex (see Video S3 in the supplementary material). Figure 1 shows two deep barrierless potential wells at a Rb-He distance of about 3 \AA . In the course of the dynamics, the Rb atom is drawn to the well close to the droplet surface, develops a RbHe exciplex that remains bound to it, and oscillates around an equilibrium position of $\sim 3 \text{ \AA}$ above the static equilibrium position at the dimple as shown in Figure 6. This result is in full agreement with static QMC calculations by Leino et al.⁴⁹. Note that our simulations do not provide any indication that the vibrational motion

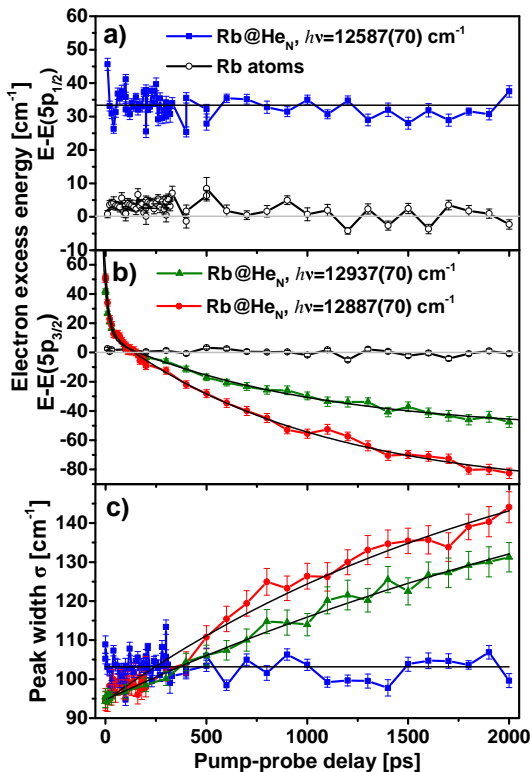


Figure 4 Photoelectron energies as a function of pump-probe delay (filled circles) recorded at laser wavelengths $\lambda = 794$ nm (12594 cm⁻¹, $5p\Pi_{1/2}$) (a), $\lambda = 773$ nm (12937 cm⁻¹, $5p\Sigma_{1/2}$), and $\lambda = 776$ nm (12887 cm⁻¹, $5p\Pi_{3/2}$) (b). Open circles indicate the electron energies measured for atomic Rb background signal. The widths of electron distributions are depicted in (c).

of the RbHe exciplex structure leads to its desorption from the He droplet.

The dynamics of the exciplex formation process can be quantitatively represented by integrating over the He density within a spherical inclusion volume with radius r_{incl} around Rb. The result is shown in Figure 7. Thus, for $r_{\text{incl}} = 5.7$ Å, which contains the entire localized He density at the Rb atom without including He density of the remaining droplet, we find a rise to 75 % of the final value at $t = 20$ ps. For $t > 60$ ps the He number density stabilizes close to 1, indicating the full evolution of a RbHe exciplex containing 1 He atom. This result is in good agreement with the formation time estimated using the tunneling model by Reho et al.³³ using model parameters inferred from the previous fs-ps pump-probe measurements (42 ps)⁵⁰.

The finding that the RbHe exciplex remains attached to the He droplet is in apparent contradiction to experiments where the ejection of free Rb and RbHe was clearly observed^{19,34,36}. Therefore, an additional mechanism must be active that induces the

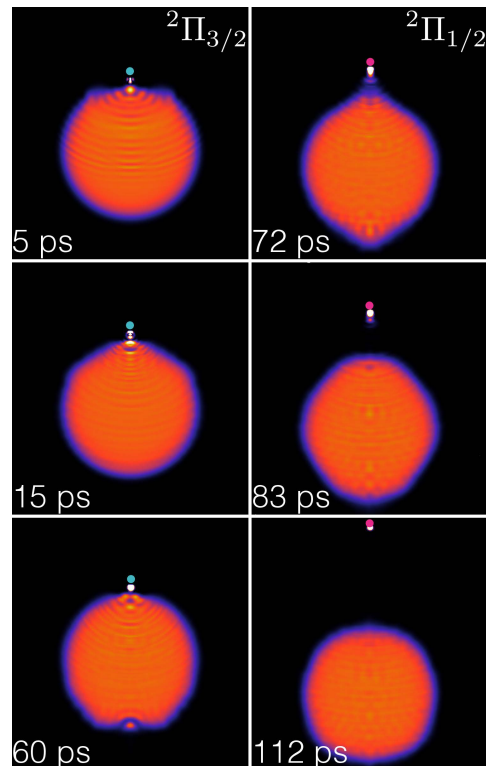


Figure 5 Snapshots of the He density during the evolution of the excited RbHe₁₀₀₀ complex for $\eta = 15\%$, $\Delta t = 60$ ps. The green dot represents the Rb atom excited into the $5p\Pi_{3/2}$ -state; the magenta dot is the Rb atom after suddenly relaxing to the $5p\Pi_{1/2}$ -state. The white spot accompanying the green or magenta dot representing the Rb atom depicts the He density carried away with it.

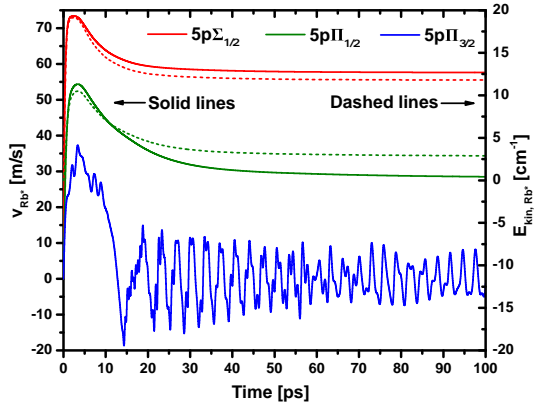


Figure 6 Velocity (solid lines, left scale) and kinetic energy (dashed lines, right scale) of the Rb atom excited to the 5p-state as a function of time. The kinetic energy of the $5p\Pi_{3/2}$ -state is not given as this state remains bound to the droplet.

η (%)	v_∞ (m/s)	Kin. energy (cm^{-1})
5	bound	–
10	13.4	0.64
12.5	43.0	6.6
15	62.4	13.9
20	80.4	23.0

Table 3 Asymptotic velocity and kinetic energy of the ejected RbHe exciplex for various values of the fraction η of the $5p\Pi_{3/2,1/2}$ -energy spacing of 165 cm^{-1} , which is converted into kinetic energy of Rb by relaxation from the $5p\Pi_{3/2}$ into the $5p\Pi_{1/2}$ -state. The calculations are carried out at a delay time $\Delta t = 60 \text{ ps}$ between photo-excitation and non-radiative de-excitation of the Rb atom.

desorption of the RbHe molecule off the He droplet surface.

4.2 RbHe exciplex formation around the $5p^2\Pi_{1/2}$ -state: non-radiative relaxation from the $5p^2\Pi_{3/2}$ -state

In the gas phase, a RbHe exciplex can form in the $5p\Pi_{1/2}$ -state if enough kinetic energy is provided by collisions such that the Rb can overcome the potential barrier⁵⁸. Alternatively, collisions of a RbHe formed in the $5p\Pi_{3/2}$ -state with another atom or complex might induce relaxation into a RbHe electronic state correlating to the Rb $5p_{1/2}$ -state. In this case the barrier is circumvented by the relaxation process, as the potential wells for the two states $\Pi_{3/2}$ and $\Pi_{1/2}$ are at similar Rb-He distances. In the condensed (droplet) phase at 0.4 K temperature, none of these mechanisms are active to explain the formation of RbHe $5p^2\Pi_{1/2}$ exciplexes and their potential ejection.

However, Figure 1 a) indicates another possible mechanism: Non-radiative de-excitation from the $5p\Pi_{3/2}$ to the $5p\Pi_{1/2}$ -state accompanied by transfer of energy into the relative motion of the Rb atom away from the He droplet. Notice from the figure that the minimum of the $5p\Pi_{3/2}$ -potential is at $\sim 12683 \text{ cm}^{-1}$, and that of the $5p\Pi_{1/2}$ -potential is at $\sim 12518 \text{ cm}^{-1}$; the value of this potential at the barrier is 12611 cm^{-1} . Thus, non-radiative de-excitation of the Rb atom may add to its original kinetic energy a fraction of this 165 cm^{-1} difference energy. Consequently, the RbHe exciplex will be ejected in the $5p\Pi_{1/2}$ -state, and not in the $5p\Pi_{3/2}$ -state that was originally photo-excited. Non-radiative electronic relaxation induced by the He droplet has been observed for a number of metal atoms^{18–21,41,44,73}. In particular, previous measurements of the dispersed fluorescence emitted upon excitation of Rb into the $5p\Pi_{3/2}$ -state of the Rb-He droplet complex have evidenced large populations of free Rb atoms in the $5p\Pi_{1/2}$ -state³⁴. Efficient spin-relaxation of $5p\Pi_{3/2}$ -excited Rb atoms can be rationalized by the large cross section for mixing of fine structure states in collisions of alkali metal atoms with He⁷⁴. For low-temperature Rb-He collisions, the fine structure relaxation rate was found to be enhanced by the transient formation of a RbHe exciplex by orders of magnitude compared to binary Rb-He collisions⁵⁸.

Here, we explore this scenario within TD-DFT. Starting from Rb in the $5p\Pi_{3/2}$ -state, we induce a “vertical DFT transition” by suddenly switching potential energy surfaces from $5p\Pi_{3/2}$ to $5p\Pi_{1/2}$, imparting to the Rb a kinetic energy corresponding to a fraction

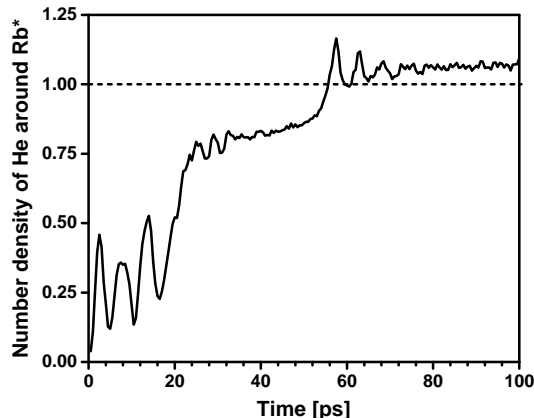


Figure 7 Simulated time evolution of the integrated He density within an inclusion volume of radius $r_{\text{incl}} = 5.7 \text{ \AA}$ around the Rb atom excited to the $5p\Pi_{3/2}$ -state.

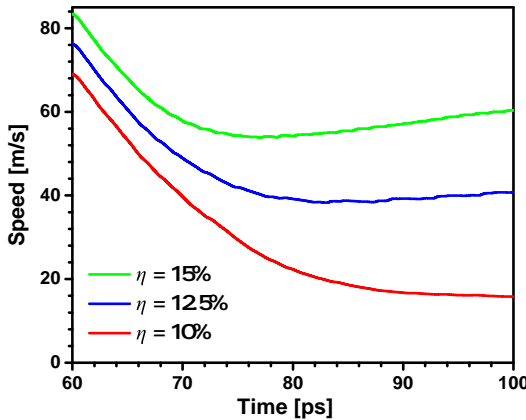


Figure 8 Velocity of the excited Rb atom with attached He density as a function of time after $5p\Pi_{3/2} \rightarrow 5p\Pi_{1/2}$ relaxation at $\Delta t = 60$ ps for various values of the energy conversion factor η .

η of the available non-radiative de-excitation energy. The time Δt elapsing between the vertical excitation and de-excitation has to be chosen as well; this time influences the degree of RbHe $5p\Pi_{3/2}$ exciplex formation which, as we have seen, may require some tens of ps. The actual value of these inputs cannot be determined by the model itself.

In the following, we present results obtained from simulations using as input parameters the delay before relaxation $\Delta t = 60$ ps, and several values of η . As shown in Figure 6 (see also the bottom left panel of Figure 5), this –arbitrary– time is sufficient to allow for a full development of the $5p\Pi_{3/2}$ /RbHe exciplex and to bring it to a rather stationary configuration.

The snapshots in Figure 5 and the corresponding animation (Video S4 in the supplementary material) illustrate the evolution following the $5s\Sigma_{1/2} \rightarrow 5p\Pi_{3/2} \rightarrow 5p\Pi_{1/2}$ process for $\eta = 15\%$, $\Delta t = 60$ ps. Thus, upon sudden relaxation to the $5p\Pi_{1/2}$ -state, the RbHe structure promptly detaches from the remaining He droplet. The velocity of the Rb atom as a function of time is depicted in Figure 8 for this and other values of η . Clearly, as the fraction of relaxation energy converted to Rb kinetic energy is increased from 10 % to 15 %, the initial speed, and even more so, the asymptotic value for long evolution times rises significantly. Table 3 collects the results obtained for various values of η . It can be seen that a fairly small $\eta \geq 10\%$ is enough to induce the ejection of the RbHe complex. For a value $\eta = 12.5\%$, the asymptotic value of the RbHe velocity matches best the experimental one measured for maximum $5p\Pi_{3/2}$ -excitation at $\lambda = 776$ nm (12887 cm $^{-1}$).

When assuming that the relaxation-induced RbHe desorption proceeds as an impulsive dissociation reaction, the conversion factor η can be related to an effective mass of the He droplet, m_{eff} ²⁴. From $\eta = 12.5\%$ we obtain $m_{eff} = 12.7$ amu, which corresponds to about 3 He atoms effectively interacting with the excited RbHe. This value is significantly less than what was found

for the prompt desorption of Rb and RbHe upon excitation of the Rb 6s and 6p-correlated states^{19,26}. This is no surprise, though, since the orbital overlap between the excited RbHe and the He droplet is smaller than for the higher excited and more extended 6s and 6p-states. Besides, the effective mass model is not strictly valid in the present situation, since it neglects the internal degrees of freedom of RbHe which is taken as one fixed subunit.

Now that we have established the RbHe formation and desorption mechanisms, we can take our comparative study one step further and compute from the simulation results the electron binding energies to compare with the experimental photoelectron spectra. For this, we evaluate the interaction energy of the excited Rb atom and of the Rb $^+$ ion with the droplet by calculating, respectively,

$$U^*(t) = \int d\mathbf{r} \gamma_{\text{He-Rb}^*}(|\mathbf{r} - \mathbf{r}_{\text{Rb}^*}|) \rho(\mathbf{r}, t) \quad (5)$$

and

$$U^+(t) = \int d\mathbf{r} \gamma_{\text{He-Rb}^+}(|\mathbf{r} - \mathbf{r}_{\text{Rb}^+}|) \rho(\mathbf{r}, t). \quad (6)$$

Here the He-Rb $^+$ pair potential $\gamma_{\text{He-Rb}^+}$ is taken from Ref.⁴⁰.

The interaction energies $U^*(t)$ and $U^+(t)$ are shown in Figure 9 for Rb in the $\Sigma_{1/2}$ -state in a), for the $\Pi_{1/2}$ -state in b), and for the $\Pi_{3/2}$ -state in c). Figure 9 d) shows the evolution following the sudden relaxation of Rb to the $\Pi_{1/2}$ -state at $t = 60$ ps. The prompt desorption of Rb in the $\Sigma_{1/2}$ and $\Pi_{1/2}$ -states is seen as a sudden drop of $U^*(t)$ near $t = 0$ followed by a slow rise towards zero due to long-range van der Waals attraction as Rb departs from the He droplet. Due to the purely attractive interaction of the Rb $^+$ ion with the He droplet, $U^+(t)$ monotonically rises to zero. The exciplex formation dynamics in the $\Pi_{3/2}$ -state is reflected by the irregular behavior of $U^*(t)$ and $U^+(t)$, eventually stabilizing at $t > 60$ ps at negative values, *i.e.* in a configuration where Rb is bound to the He droplet. Only when allowing for a sudden relaxation into the $\Pi_{1/2}$ -state at $t = 60$ ps, the RbHe exciplex receives a momentum “kick” and subsequently detaches from the He droplet, in spite of a rising $U^*(t)$. The asymptotic values of U^* and U^+ are then given by the binding energy of the free RbHe exciplex configuration. The fast oscillations at $t > 65$ ps indicate that RbHe keeps vibrating as it is ejected.

5 Discussion

Knowledge of the interaction energies $U^*(t)$ and $U^+(t)$ allows us to determine the electron binding energy $E_b(t) = U^+(t) - U^*(t)$ and to compare it with the experimental photoelectron spectra. Here, $U^*(t)$ and $U^+(t)$ are referenced to their asymptotic values, *i.e.* the binding energies of free Rb and Rb $^+$, respectively. The resulting values of E_b are depicted as thick colored lines in Figure 10 in the range of delay times 0–100 ps. Compared to the experimental values, we note both matches and deviations. The TD-DFT values of E_b for the $\Pi_{1/2}$ -state (red line) converge within 100 ps to the value of the free Rb($5p_{1/2}$)-atom, as in the simulation Rb in that state detaches from the droplet. In contrast, the experimental values (blue symbols) are constant and below the atomic value because most of the atoms actually remain bound to the He droplet, see section 3.2.

The TD-DFT values for the $\Sigma_{1/2}$ -state (green line) quickly rise

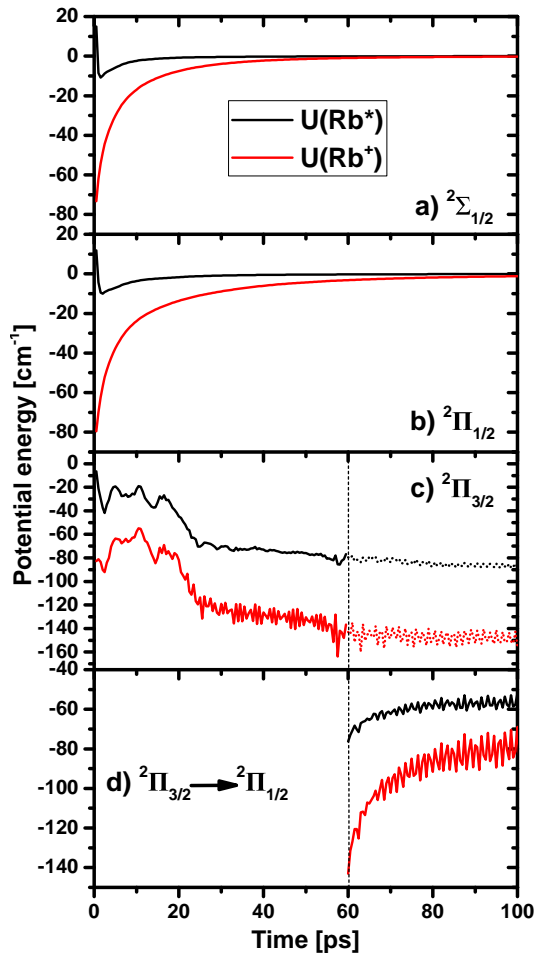


Figure 9 Simulated energies of the Rb-atom excited into various states interacting with the surrounding He distribution (black lines), and of the Rb⁺ ion for the same momentary geometry (red lines). In d), the excited state of Rb is suddenly switched from $\Pi_{3/2}$ to $\Pi_{1/2}$ to simulate the dynamics initiated by spin-relaxation.

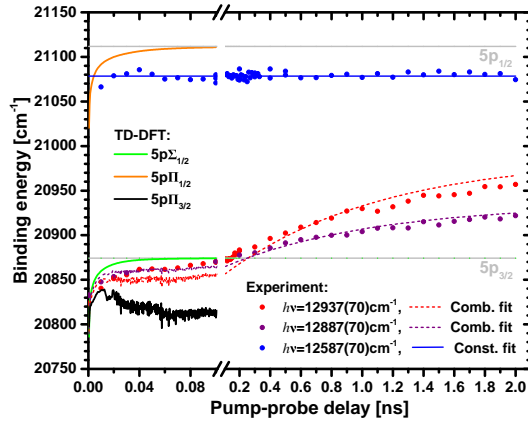


Figure 10 Comparison of experimental and simulated electron binding energies. Thick solid lines: TD-DFT results. Dashed lines: Combined TD-DFT and analytical model. Thin solid lines: Biexponential fits of the experimental data.

to $E_{5p3/2}$ within a few tens of ps, again due to prompt desorption, yielding free Rb $5p_{3/2}$ atoms. The experimental values for excitation at 12,937 and 12,887 cm⁻¹ (red and grey symbols) show a very similar increase in that time range. This supports our conclusion that the fast dynamics observed both in the photoelectron peak position and in the yield of photoions mainly results from prompt desorption of the $\Sigma_{1/2}$ -component of the excited state. In the experiment we found that the [RbHe]⁺ ion signal associated with $\Pi_{3/2}$ -component of the excitation features a weak fast rising component as well [Figure 3 c)]. This we attribute to a finite rate of prompt desorption of Rb and RbHe in the $\Pi_{3/2}$ -state.

The TD-DFT curve for the $\Pi_{3/2}$ -state without relaxation (black line) drops in binding energy, at odds with the experiment. However, when $\Pi_{3/2} \rightarrow \Pi_{1/2}$ -relaxation is included, the simulated curve also rises, staying only slightly below the experimental values in the time range 20–100 ps. Thus, we achieve good agreement of our extended TD-DFT simulations with the experiment for the fast (tens of ps) desorption of the $\Sigma_{1/2}$ -state, and qualitative agreement with regard to the desorption of the $\Pi_{3/2}$ -state when allowing for spin-relaxation.

The lacking quantitative agreement is not surprising given the simplicity of our assumption – instantaneous spin-relaxation. Naturally, this relaxation process has its own time dependence. If we identify the latter with the observed slow variation of photoelectron spectra and ion yields, we can set up a more realistic, combined model. Hereby, we account for the populations $p_{\Sigma1/2}$ in the $\Sigma_{1/2}$ -state and $p_{\Pi3/2}$ in the $\Pi_{3/2}$ state, which are determined by the spectral profile of the laser $I_\ell(\hbar\nu)$. The coefficients $p_{\Sigma1/2,\Pi3/2}$ are calculated from the state-selective absorption profiles $I_\Sigma(\hbar\nu)$ and $I_\Pi(\hbar\nu)$ using LeRoy's LEVEL program⁷⁵ based on the spin-orbit corrected pseudodiatom potentials by Callegari and Ancilotto⁶⁵. In a second step, the absorption profiles are weighted with $I_\ell(\hbar\nu)$ and integrated over $\hbar\nu$, yielding $p_{\Pi3/2} = 0.28$ for the center frequency $\hbar\nu = 12,937$ cm⁻¹ and

$p_{\Pi_{3/2}} = 0.52$ for $h\nu = 12,887 \text{ cm}^{-1}$.

The transient energy of the $\Pi_{3/2}$ -state, $E_{\Pi_{3/2}}(t)$, consists of a contribution of the binding energy [$U_{\Pi_{3/2} \rightarrow \Pi_{1/2}}^+ - U_{\Pi_{3/2} \rightarrow \Pi_{1/2}}^*$] for the dynamics including relaxation to $\Pi_{1/2}$, and a contribution [$U_{\Pi_{3/2}}^+ - U_{\Pi_{3/2}}^*$] for the $\Pi_{3/2}$ -state without relaxation. When assuming an exponential time dependence of the relaxation with a time constant τ , we get

$$\begin{aligned} E(t) &= p_{\Sigma_{1/2}} \cdot [U_{\Sigma_{1/2}}^+ - U_{\Sigma_{1/2}}^*] + p_{\Pi_{3/2}} \cdot e^{-\ln 2 / \tau} \cdot [U_{\Pi_{3/2}}^+ - U_{\Pi_{3/2}}^*] \\ &+ p_{\Pi_{3/2}} \cdot (1 - e^{-\ln 2 / \tau}) \cdot [U_{\Pi_{3/2} \rightarrow \Pi_{1/2}}^+ - U_{\Pi_{3/2} \rightarrow \Pi_{1/2}}^*]. \end{aligned}$$

Here, $U^*(t)$ and $U^+(t)$ are extrapolated for long times $t > 200 \text{ ps}$ by constants for the $\Sigma_{1/2}$ and $\Pi_{3/2}$ -states and by an exponential function for the $\Pi_{3/2} \rightarrow \Pi_{1/2}$ case. For simplicity, we neglect the 60 ps time delay between excitation and relaxation which is short compared to the full relaxation dynamics.

If we assign to τ the experimental value of the slow time constant of the fit of photoelectron energies, $\tau = \tau_{\text{c}}^{\text{f}}$, we obtain the dashed lines in Figure 10, which nicely match the experimental data. Thus, we identify the slow variations of ion and electron signals spanning hundreds of ps to He-induced spin-relaxation, which proceeds on that time scale and causes the desorption of RbHe exciplexes. The fact that the Rb^+ signal associated mainly with $\Sigma_{1/2}$ -excitation features a weak slowly rising component as well [Figure 3 c) and d)], we take as an indication that spin-relaxation also causes the desorption of neat $\text{Rb}(\text{Sp}_{1/2})$ -atoms to some extent.

6 Conclusion

In summary, we have presented a detailed study of the formation and desorption dynamics of RbHe exciplexes initiated by laser excitation of Rb atoms attached to He nanodroplets. Experimentally, the two-color femtosecond pump-probe photoionization scheme allows us to selectively probe the dynamics of the lowest three excited states of the Rb-He droplet complex. Both photoion and photoelectron signals feature pump-probe dynamics proceeding on two distinct time scales (~ 30 and 700 ps). By comparing with time-dependent DFT simulations, complemented by a spin-relaxation mechanism, we conclude that the fast dynamics is due to prompt desorption of Rb atoms when exciting the $\Sigma_{1/2}$ -state. The slow desorption of RbHe exciplexes is induced by $\Pi_{3/2} \rightarrow \Pi_{1/2}$ spin-relaxation. By analyzing the rearrangement of the He surrounding the Rb atom in the $\Pi_{3/2}$ -state, we infer a formation time of the RbHe exciplex ranging between 20 and 50 ps. When exciting the lowest state of the Rb-He droplet complex, $\Pi_{1/2}$, we find that a small fraction of Rb atoms desorbs as free atoms, as predicted by the DFT simulation, whereas the larger fraction Rb atoms remains bound to the He droplets.

While this work represents in our opinion the most complete investigation of the real-time dynamics of an alkali metal-He exciplex, still some uncertainties remain. In the experiment, a better reconcilability of electron and ion signals may be achieved by detecting electrons and ions in coincidence^{71,76}. Furthermore, extending such studies to other types of dopant species which are solvated more deeply inside He droplets (e.g. alkaline earth met-

als, transition metals) would give further insight into the mechanisms of desolvation and ejection of excited impurity atoms out of He nanodroplets^{18,20,21,77}.

On the theory side, a more complete description of the couplings between electronic states and the configurational degrees of freedom in such excited complexes induced by the He droplet environment would be highly desirable^{3,4}. In a recent advance, electronic relaxation of Ba^+ ions in He nanodroplets, based on a diabatization of the He- Ba^+ ground and excited electronic states interaction potentials⁵, has been proposed as a mechanism for ejecting Ba^+ and Ba^+He_n off He droplets. These mechanisms for spin-relaxation and inter-electronic state relaxation have to be confirmed by real-time dynamics studies.

6.0.0.1 Acknowledgements The authors would like to thank Marcel Drabbels for useful exchanges. Financial support by the Deutsche Forschungsgemeinschaft (MU 2347/6-1 and IRTG 2079) is greatly acknowledged. This work has been performed under Grant No. FIS2017-87801-P from DGI, Spain. M. B. thanks the Université Fédérale Toulouse Midi-Pyrénées for financial support throughout the “Chaires d’Attractivité 2014” Programme IMDYNHE. The dynamics simulations presented in this work have been carried out thanks to the HPC resources of CALMIP supercomputing center (Grant P1039).

References

- C. George, M. Ammann, B. D’Anna, D. J. Donaldson and S. A. Nizkorodov, *Chem. Rev.*, 2015, **115**, 4218–4258.
- J. Schneider, D. Bahnemann, J. Ye, G. L. Puma and D. D. Dionysiou, *Photocatalysis: Fundamentals and Perspectives*, The Royal Society of Chemistry, Cambridge CB4 0WF, UK, 2016.
- K. D. Closser, O. Gessner and M. Head-Gordon, *J. Chem. Phys.*, 2014, **140**, 134306.
- A. Masson, M.-C. Heitz, J.-M. Mestdagh, M.-A. Gaveau, L. Poisson and F. Spiegelman, *Phys. Rev. Lett.*, 2014, **113**, 123005.
- P. Vindel-Zandbergen, M. Barranco, F. Cargnoni, M. Drabbels, M. Pi and N. Halberstadt, *Helium-induced electronic transitions in photo-excited Ba^+-He_n exciplexes*, submitted, 2018.
- J. P. Toennies and A. F. Vilesov, *Angew. Chem. Int. Ed.*, 2004, **43**, 2622.
- F. Stienkemeier and K. Lehmann, *J. Phys. B*, 2006, **39**, R127.
- F. Ancilotto, G. DeToffol and F. Toigo, *Phys. Rev. B*, 1995, **52**, 16125–16129.
- F. Stienkemeier, J. Higgins, C. Callegari, S. I. Kanorsky, W. E. Ernst and G. Scoles, *Z. Phys. D*, 1996, **38**, 253–263.
- M. Barranco, R. Guardiola, S. Hernández, R. Mayol, J. Navarro and M. Pi, *J. Low Temp. Phys.*, 2006, **142**, 1–81.
- C. Stark and V. V. Kresin, *Phys. Rev. B*, 2010, **81**, 085401.
- L. An der Lan, P. Bartl, C. Leidlmair, H. Schöbel, R. Jochum, S. Denifl, T. D. Märk, A. M. Ellis and P. Scheier, *J. Chem. Phys.*, 2011, **135**, 044309.
- L. An der Lan, P. Bartl, C. Leidlmair, H. Schöbel, S. Denifl, T. D. Märk, A. M. Ellis and P. Scheier, *Phys. Rev. B*, 2012, **85**, 115414.

- 14 Höller, Johannes, Krotscheck, Eckhard and Zillich, Robert E., *Eur. Phys. J. D*, 2015, **69**, 198.
- 15 F. Calvo, *Phys. Rev. B*, 2017, **95**, 035429.
- 16 M. Mudrich and F. Stienkemeier, *Int. Rev. Phys. Chem.*, 2014, **33**, 301–339.
- 17 F. Ancilotto, M. Barranco, F. Coppens, J. Eloranta, N. Halberstadt, A. Hernando, D. Mateo and M. Pi, *Int. Rev. Phys. Chem.*, 2017, **36**, 621–707.
- 18 E. Loginov and M. Drabbels, *J. Phys. Chem. A*, 2007, **111**, 7504–7515.
- 19 L. Fechner, B. Grüner, A. Sieg, C. Callegari, F. Ancilotto, F. Stienkemeier and M. Mudrich, *Phys. Chem. Chem. Phys.*, 2012, **14**, 3843.
- 20 A. Kautsch, M. Koch and W. E. Ernst, *J. Phys. Chem. A*, 2013, **117**, 9621–9625.
- 21 F. Lindebner, A. Kautsch, M. Koch and W. E. Ernst, *Int. J. Mass Spectrom.*, 2014, **365–366**, 255–259.
- 22 M. Koch, G. Auböck, C. Callegari and W. E. Ernst, *Phys. Rev. Lett.*, 2009, **103**, 035302.
- 23 S. Smolarek, N. B. Brauer, W. J. Buma and M. Drabbels, *J. Am. Chem. Soc.*, 2010, **132**, 14086–14091.
- 24 A. Hernando, M. Barranco, M. Pi, E. Loginov, M. Langlet and M. Drabbels, *Phys. Chem. Chem. Phys.*, 2012, **14**, 3996–4010.
- 25 D. Mateo, A. Hernando, M. Barranco, E. Loginov, M. Drabbels and M. Pi, *Phys. Chem. Chem. Phys.*, 2013, **15**, 18388–18400.
- 26 J. von Vangerow, A. Sieg, F. Stienkemeier, M. Mudrich, A. Leal, D. Mateo, A. Hernando, M. Barranco and M. Pi, *J. Phys. Chem. A*, 2014, **118**, 6604–6614.
- 27 J. von Vangerow, O. John, F. Stienkemeier and M. Mudrich, *J. Chem. Phys.*, 2015, **143**, 034302.
- 28 A. Sieg, J. von Vangerow, F. Stienkemeier, O. Dulieu and M. Mudrich, *J. Phys. Chem. A*, 2016, **120**, 7641–7649.
- 29 J. von Vangerow, F. Coppens, A. Leal, M. Pi, M. Barranco, N. Halberstadt, F. Stienkemeier and M. Mudrich, *J. Phys. Chem. Lett.*, 2017, **8**, 307–312.
- 30 A. Przystawik, S. Göde, T. Döppner, J. Tiggesbäumker and K. H. Meiwes-Broer, *Phys. Rev. A*, 2008, **78**, 021202.
- 31 S. Müller, S. Krapf, T. Koslowski, M. Mudrich and F. Stienkemeier, *Phys. Rev. Lett.*, 2009, **102**, 183401.
- 32 A. Kautsch, M. Koch and W. E. Ernst, *Phys. Chem. Chem. Phys.*, 2015, **17**, 12310–12316.
- 33 J. Reho, J. Higgins, C. Callegari, K. K. Lehmann and G. Scoles, *J. Chem. Phys.*, 2000, **113**, 9694–9701.
- 34 F. R. Brühl, R. A. Trasca and W. E. Ernst, *J. Chem. Phys.*, 2001, **115**, 10220–10224.
- 35 C. P. Schulz, P. Claas and F. Stienkemeier, *Phys. Rev. Lett.*, 2001, **87**, 153401.
- 36 G. Dropelmann, O. Bünermann, C. P. Schulz and F. Stienkemeier, *Phys. Rev. Lett.*, 2004, **93**, 0233402.
- 37 M. Mudrich, G. Dropelmann, P. Claas, C. Schulz and F. Stienkemeier, *Phys. Rev. Lett.*, 2008, **100**, 023401.
- 38 S. Müller, M. Mudrich and F. Stienkemeier, *J. Chem. Phys.*, 2009, **131**, 044319.
- 39 M. Theisen, F. Lackner and W. E. Ernst, *Phys. Chem. Chem. Phys.*, 2010, **12**, 14861–14863.
- 40 A. Leal, D. Mateo, A. Hernando, M. Pi, M. Barranco, A. Ponti, F. Cargnani and M. Drabbels, *Phys. Rev. B*, 2014, **90**, 224518.
- 41 E. Loginov, A. Hernando, J. A. Beswick, N. Halberstadt and M. Drabbels, *J. Phys. Chem. A*, 2015, **119**, 6033–6044.
- 42 M. Kuhn, M. Renzler, J. Postler, S. Ralsen, S. Spieler, M. Simpson, H. Linnartz, A. G. G. M. Tielens, J. Cami, A. Mauacher, Y. Wang, M. Alcamí, F. Martín, M. K. Beyer, R. Wester, A. Lindinger and P. Scheier, *Nat. Comm.*, 2016, **7**, 13550.
- 43 N. B. Brauer, S. Smolarek, E. Loginov, D. Mateo, A. Hernando, M. Pi, M. Barranco, W. J. Buma and M. Drabbels, *Phys. Rev. Lett.*, 2013, **111**, 153002.
- 44 M. Koch, A. Kautsch, F. Lackner and W. E. Ernst, *J. Phys. Chem. A*, 2014, **118**, 8373–8379.
- 45 Y. Seki, T. Takayanagi and M. Shiga, *Phys. Chem. Chem. Phys.*, 2017, **19**, 13798–13806.
- 46 G. Auböck, J. Nagl, C. Callegari and W. E. Ernst, *Phys. Rev. Lett.*, 2008, **101**, 035301.
- 47 M. Theisen, F. Lackner and W. E. Ernst, *J. Phys. Chem. A*, 2011, **115**, 7005–7009.
- 48 T. Takayanagi and M. Shiga, *Phys. Chem. Chem. Phys.*, 2004, **6**, 3241.
- 49 M. Leino, A. Viel and R. E. Zillich, *J. Chem. Phys.*, 2011, **134**, 024316.
- 50 C. Giese, T. Mullins, B. Grüner, M. Weidmüller, F. Stienkemeier and M. Mudrich, *J. Chem. Phys.*, 2012, **137**, 244307.
- 51 S. H. Patil, *J. Chem. Phys.*, 1991, **94**, 8089–8095.
- 52 J. Pascale, *Phys. Rev. A*, 1983, **28**, 632–644.
- 53 F. Ancilotto, M. Barranco, F. Caupin, R. Mayol and M. Pi, *Phys. Rev. B*, 2005, **72**, 214522.
- 54 M. Pi, F. Ancilotto, F. Coppens, N. Halberstadt, A. Hernando, A. Leal, D. Mateo, R. Mayol and M. Barranco, *⁴He-DFT BCN-TLS: A Computer Package for Simulating Structural Properties and Dynamics of Doped Liquid Helium-4 Systems*. <https://github.com/bcntls2016/>.
- 55 D. Mateo, A. Hernando, M. Barranco, R. Mayol and M. Pi, *Phys. Rev. B*, 2011, **83**, 174505.
- 56 A. Hernando, M. Barranco, R. Mayol, M. Pi and M. Krośnicki, *Phys. Rev. B*, 2008, **77**, 024513.
- 57 O. Bünermann, G. Dropelmann, A. Hernando, R. Mayol and F. Stienkemeier, *J. Phys. Chem. A*, 2007, **111**, 12684.
- 58 K. Hirano, K. Enomoto, M. Kumakura, Y. Takahashi and T. Yabuzaki, *Phys. Rev. A*, 2003, **68**, 012722.
- 59 A. T. J. B. Eppink and D. H. Parker, *Rev. Sci. Instrum.*, 1997, **68**, 3477.
- 60 A. Wituschek, J. von Vangerow, J. Grzesiak, F. Stienkemeier and M. Mudrich, *Rev. Sci. Instrum.*, 2016, **87**, 083105.
- 61 G. A. Garcia, L. Nahon and I. Powis, *Rev. Sci. Instrum.*, 2004, **75**, 4989–4996.
- 62 B. Dick, *Phys. Chem. Chem. Phys.*, 2014, **16**, 570–580.
- 63 A. Braun and M. Drabbels, *J. Chem. Phys.*, 2007, **127**, 114303.
- 64 G. S. Mudholkar and A. D. Hutson, *J. Stat. Plan. Inference*, 2000, **83**, 291–309.

- 65 C. Callegari and F. Ancilotto, *J. Phys. Chem. A*, 2011, **115**, 6789–6796.
- 66 R. N. Zare, *Mol. Photochem.*, 1972, **44**, 1.
- 67 M. Theisen, F. Lackner, G. Krois and W. E. Ernst, *J. Phys. Chem. Lett.*, 2011, **2**, 2778–2782.
- 68 E. Loginov, D. Rossi and M. Drabbels, *Phys. Rev. Lett.*, 2005, **95**, 163401.
- 69 D. S. Peterka, J. H. Kim, C. C. Wang and D. M. Neumark, *J. Phys. Chem. B*, 2006, **110**, 19945–19955.
- 70 C. C. Wang, O. Kornilov, O. Gessner, J. H. Kim, D. S. Peterka and D. M. Neumark, *J. Phys. Chem. A*, 2008, **112**, 9356.
- 71 D. Buchta, S. R. Krishnan, N. B. Brauer, M. Drabbels, P. O’Keeffe, M. Devetta, M. Di Fraia, C. Callegari, R. Richter, M. Coreno, K. C. Prince, F. Stienkemeier, R. Moshammer and M. Mudrich, *J. Phys. Chem. A*, 2013, **117**, 4394–4403.
- 72 M. Leino, A. Viel and R. E. Zillich, *J. Chem. Phys.*, 2008, **129**, 184308.
- 73 E. Loginov and M. Drabbels, *J. Phys. Chem. A*, 2014, **118**, 2738–2748.
- 74 L. Krause, in *Adv. Chem. Phys.*, edited by J. W. McGowan (Wiley, New York), 1975.
- 75 R. LeRoy, *Chemical Physics Research Report*, University of Waterloo, CP-555, 1995, 1995.
- 76 A. C. LaForge, V. Stumpf, K. Gokhberg, J. von Vangerow, F. Stienkemeier, N. V. Kryzhevci, P. O’Keeffe, A. Ciavarini, S. R. Krishnan, M. Coreno, K. C. Prince, R. Richter, R. Moshammer, T. Pfeifer, L. S. Cederbaum and M. Mudrich, *Phys. Rev. Lett.*, 2016, **116**, 203001.
- 77 E. Loginov and M. Drabbels, *J. Chem. Phys.*, 2012, **136**, 154302.

4.3 Supervised work: potassium-doped nanodroplets

UNDER the supervision of Nadine Halberstadt and me, a master stage – M2 *Physique Fondamentale* – titled “*Dynamics of a superfluid helium nanodroplet doped with a single potassium atom*” has been performed by Maxime Martinez.

The project investigates the static and dynamic behaviour of a single potassium atom excited from the $K\text{-}{}^4\text{He}_{1000}$ equilibrium configuration to the $K^*(4p)\text{-}{}^4\text{He}_{1000}$ and $K^*(5s)\text{-}{}^4\text{He}_{1000}$ states. The choice of potassium was motivated by a discrepancy in the time-resolved experimental studies^[46–48]. Moreover, the mass of potassium sits between those of the heavier alkalis like rubidium and cesium, and the lighter ones, like lithium and sodium. Therefore, potassium presents an interesting case, being on the borderline between the classical regime for heavy alkalis and a quantum-mechanical regime for the lighter ones. Both treatments of the equilibrium properties and the $5s \leftarrow 4s$ excitation are studied. This work is not included in the thesis but can be found in this reference^[49].

Part II

Head-on collisions and capture by quantised vortices

Chapter 5

Quantised vortices in droplets

One of the most unambiguous signatures of the quantum mechanical nature of a substance—and indeed superfluidity—is the appearance of quantised vortices. In contrast to a normal fluid, which will rotate as a solid body when its container moves at low angular velocity, a superfluid will remain at rest. However, above a certain critical angular velocity the thermodynamically stable state of a superfluid includes one or more quantum vortices. Such a vortex can be characterised by a macroscopic wave function and quantised velocity circulation in units of $\kappa = \frac{\hbar}{m}$, where \hbar is Planck's constant and m is the mass of the ^4He atom [2,3]. Recently, the study of vorticity was extended to finite systems such as BECs confined to traps [3,4]. The transfer of energy and angular momentum in finite systems between quantised vortices and surface excitations is of particular interest, as it defines the nucleation dynamics, shape, and stability of the involved vortices [3,4]. In comparison to confined BECs, ^4He droplets are self-contained and present a case for the strongly interacting superfluid. Moreover, the diameter of a vortex core which is approximately 0.2 nm in superfluid ^4He [2] is small relative to the droplet size, suggesting a three-dimensionality of the vortices in droplets. Vorticity in ^4He droplets has therefore attracted considerable interest [5–8].

A schematic of the experiment is shown in Fig. 5.1. Helium droplets are produced by expansion of He, at 20 bar and a temperature $T_0=5.4\text{--}7\text{ K}$, into vacuum through a nozzle of diameter D 1/4 5 "m. The droplets cool rapidly via evaporation and reach a temperature of 0.37 K [20], which is well below the superfluid transition temperature T! 1/4 2:17 K [2,3]. Further downstream, the droplets capture 103–106 Ag atoms in an oven [21]. The droplets are then collided against a thin carbon film substrate at room temperature [21]. Upon impact, the droplets evaporate, leaving on the

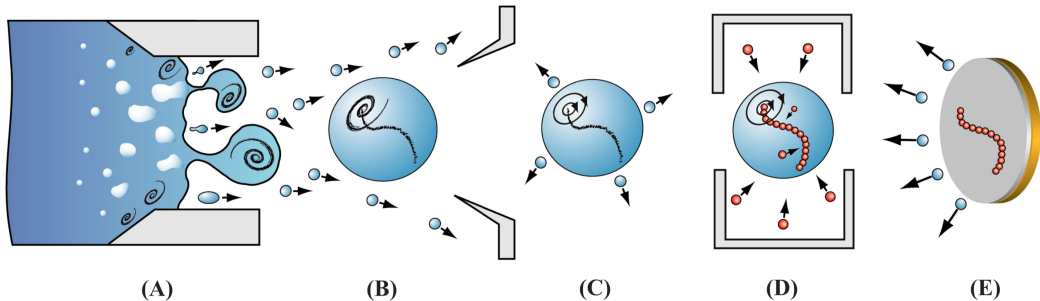


Figure 5.1: Schematic of the experiment. (a) He fluid expands in vacuum and (b) breaks up into rotating droplets. (c) A quantum vortex is formed as a consequence of fast evaporative cooling of the droplet to below T_λ . (d) The droplet is doped with Ag atoms, which are attracted to the vortex core. (e) The droplet then collides with the carbon surface leaving behind the Ag trace, whereas the He evaporates.

surface the Ag traces, which are subsequently imaged via a transmission electron microscope (TEM).

Recently, Gomez, Loginov and Vilesov performed experiments[PRL 108, 155302 (2012)] where vortices inside superfluid ^4He droplets, produced by the expansion of liquid helium, were traced by introducing Ag atoms which clustered along the vortex lines, into the droplets. The Ag clusters were subsequently surface-deposited and imaged via electron microscopy. The prevalence of elongated track-shaped deposits (see Figure 1.5) shows that vortices are present in droplets larger than about 300 nm and that their lifetime exceeds a few milliseconds. Two years later Gomez reported[Science 345, 906 (2014)] on the formation of quantum vortex lattices inside droplets. He used single-shot femtosecond x-ray coherent diffractive imaging to investigate the rotation of single, isolated superfluid helium-4 droplets containing $\sim 10^8$ to 10^{11} atoms. The formation of quantum vortex lattices inside the droplets was confirmed by observing the characteristic Bragg patterns from xenon clusters trapped in the vortex cores (see Figure 5.2).

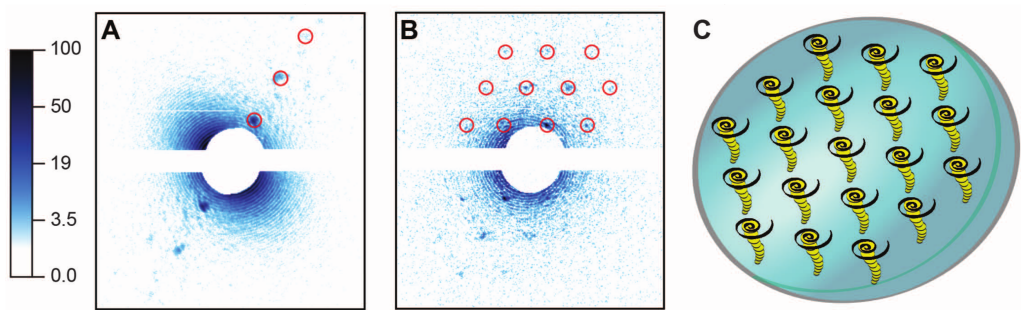


Figure 5.2: He droplets doped with Xe atoms. (A and B) X-ray diffraction images of doped droplets, displayed in a logarithmic intensity scale. (C) Droplet and embedded Xe clusters. Images in (A) and (B) correspond to tilted and parallel alignments of the vortex axes with respect to the incident x-ray beam, respectively.

Chapter 6

Head-on collisions of Xe and Cs

6.1 Introduction

It is well known that helium drops readily capture foreign atoms and molecules^[50], and this ability has had a considerable influence on the chemistry and physics of these systems^[51]. Among the studies carried out in the past on atom-drop collisions, let us mention those aiming at experimentally determining the density profiles of large ^4He and ^3He droplets from the scattering of Ar and Kr atoms off helium droplets, which have been analyzed within density functional theory (DFT)^[52,53]; the microscopic simulation of the scattering of ^3He and ^4He atoms from inhomogeneous liquid helium systems^[54,55], and an earlier theoretical work on the scattering of ^4He atoms from ^4He droplets within a liquid drop plus optical model approach^[56].

Very recently, time-dependent density functional theory (TDDFT) has been used to address the capture of Cs or Ne atoms by ^4He nanodroplets^[? ?]. The Cs capture was treated fully three dimensionally with the Cs atom described as a classical particle, whereas for the Ne capture study the Ne atom was described quantum-mechanically but the description was strictly one-dimensional.

Motivated by recent experiments that use Xe atoms to visualize vortex arrays in very large helium droplets^[57,58], we present here a first step towards the description of the capture of Xe atoms by helium droplets, namely head-on collisions of Xe atoms against a $^4\text{He}_{1000}$ droplet. A discussion on the dynamic capture of Xe atoms by droplets hosting vortex lines and vortex arrays will be provided by a forthcoming study combining DFT

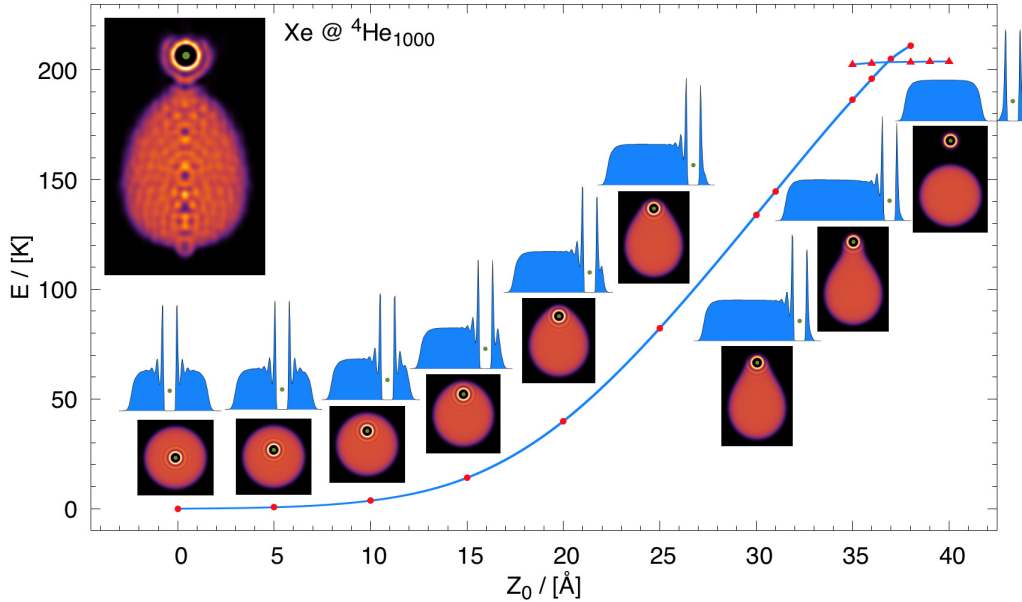


Figure 6.1: Energy of the $\text{Xe}@\text{He}_{1000}$ complex as a function of the distance between the Xe atom and the COM of the droplet. Several two-dimensional helium densities and density profiles are shown for distances between 0 and 40 Å in 5 Å steps. Connected (dots) and disconnected (triangles) helium configurations are shown (see text). Top left inset: Snapshot of the helium density at the first turning point during the dynamic evolution of a Xe atom (green dot) at $v_0 = 600$ m/s attained 78 ps after it has started. (Color figure online.)

simulation of vortex arrays as in Refs.^[59,60] for helium nanocylinders and nanodroplets and collision with Xe atoms as in this work. Whenever possible, the results for Xe, a heliophilic atom, are contrasted with results for Cs, a heliophobic atom with similar mass.

6.2 Results

We consider a droplet made of $N = 1000$ helium atoms. Its ground state structure is obtained using DFT and gives a sharp-density radius of about 22.2 Å. Then the dynamics is initiated by placing the Xe atom 32 Å away from the center of mass (COM) of the droplet with an impact parameter equal to zero (head-on collision). The simulations are carried out for initial Xe velocities v_0 ranging from 200 to 600 m/s in the system of reference of

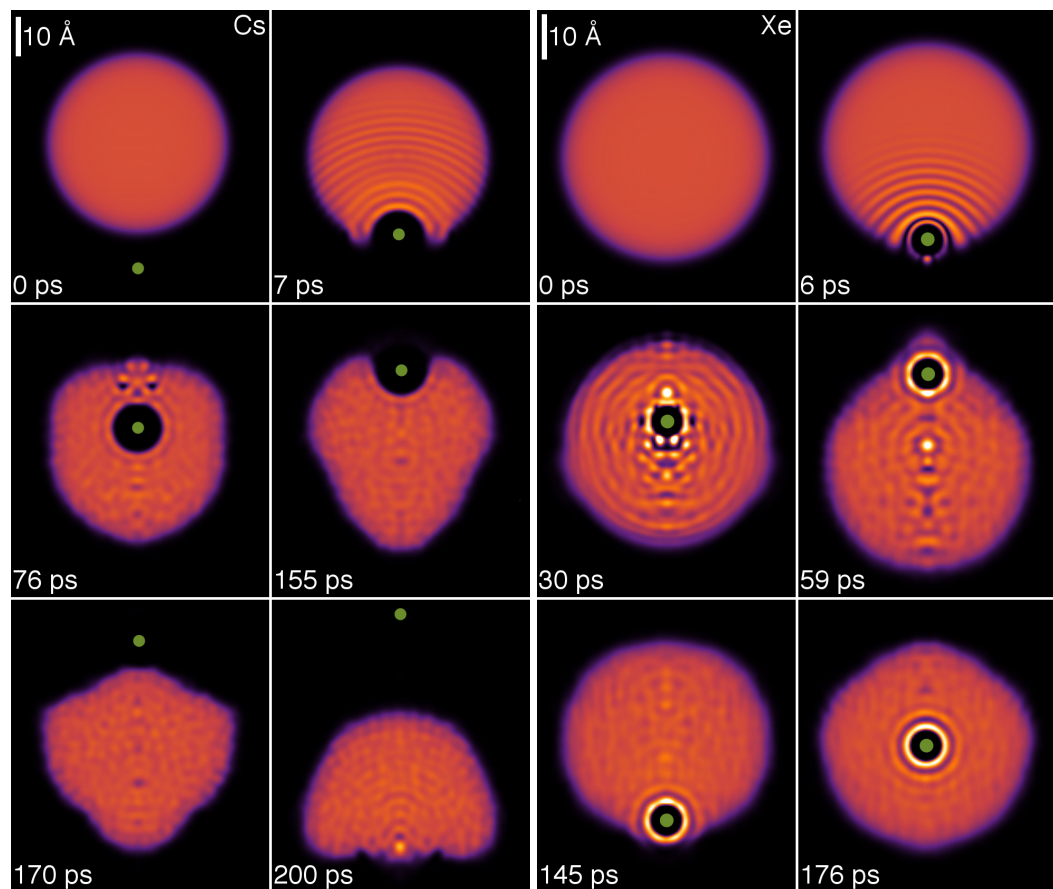


Figure 6.2: Right panel: Dynamic evolution of a Xe atom (big dot) approaching the ${}^4\text{He}_{1000}$ droplet from below at $v_0 = 200$ m/s. The corresponding time is indicated in each frame. Left panel: Same as left figure for a Cs atom. (Color figure online.)

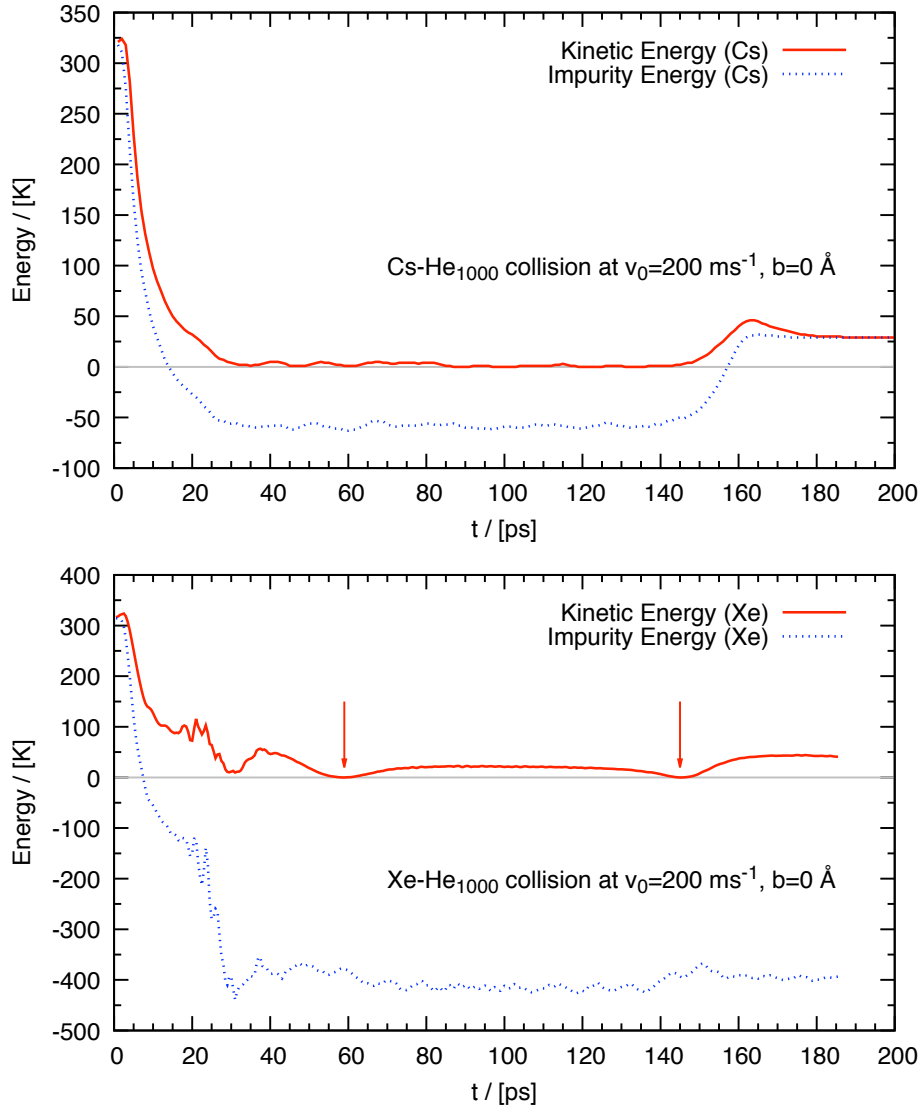


Figure 6.3: Top figure: Kinetic and total (kinetic plus potential) energy as a function of time of a Cs atom head-on colliding against a ${}^4\text{He}_{1000}$ droplet at $v_0 = 200 \text{ m/s}$. Bottom figure: same as top figure for a Xe atom. The vertical arrows indicate the first two turning points at 59 and 145 ps, whose corresponding helium densities are shown in the right Fig. 7.2. (Color figure online.)

the droplet, corresponding to kinetic energies between 315.8 K and 2842 K. These energies can be compared to the solvation energy of a Xe atom at the center of a ${}^4\text{He}_{1000}$ droplet, $S_{\text{Xe}} = E(\text{Xe} @ {}^4\text{He}_{1000}) - E({}^4\text{He}_{1000}) = -316.3$ K. For the sake of comparison, the solvation energy of Cs is -5.2 K and its equilibrium position is in a dimple at the outer droplet surface, about 26.6 Å from its center.

Thermal Xe atoms ($v_0 \sim 240$ m/s) are used in the experiments^[57,58], and the average drop velocity is about 170 m/s^[61].

Figure 7.1 shows the energy of the $\text{Xe} @ {}^4\text{He}_{1000}$ complex referred to that of the equilibrium configuration (Xe at the center of the droplet, -5716.4 K) as a function of the distance between the Xe atom and the COM of the droplet. It is obtained by a constrained calculation similar to that presented in Ref.^[62] for Ba^+ . With increasing distance, the stretched droplet-Xe configuration eventually breaks into a minicluster around the Xe atom containing about 22 helium atoms disconnected from the rest of the droplet. The appearance of this minicluster is at variance with the situation for a heliophobic impurity such as Cs^[?]. The stretched (connected) configuration energies are represented by dots, the disconnected ones by triangles. The two corresponding curves cross at 37 Å. At shorter distances the connected configuration is stable and the disconnected one metastable, and at larger distances the roles are inverted. In an actual dynamics the number of He atoms in the minicluster depends on the velocity of the Xe projectile.

Figure 7.2 displays two-dimensional plots of the helium density for Xe head-on colliding against the ${}^4\text{He}_{1000}$ droplet at $v_0 = 200$ m/s, and Fig. 7.3 the energy of the impinging atom as a function of time, with the corresponding plots for Cs collisions for the sake of comparison. It can be seen that for both species most of the initial kinetic energy is spent in piercing the droplet surface, after which the impurity moves inside the droplet at a velocity well below the critical Landau velocity v_L .

Figure 7.2 also shows that the collision launches a series of density waves in the droplet that are reflected at the droplet free surface producing complex interference patterns in its bulk. As an illustrative example, Fig. 7.4 shows the density profile along the incident direction (z axis) corresponding to the Xe collision at $v_0 = 200$ m/s, 6 ps after the process starts. The wave number associated to this wave can be estimated from the wavelength λ of the oscillations, $q = 2\pi/\lambda \sim 2.7$ Å⁻¹.

In the case of Xe, Figs. 7.2 and 7.3 reveal the appearance of turning points at which the velocity of the impurity is zero. Note that these points are not fixed during the dynamics since the droplet deforms due to the swift motion of Xe inside it; the droplet is not a rigid object and reacts to

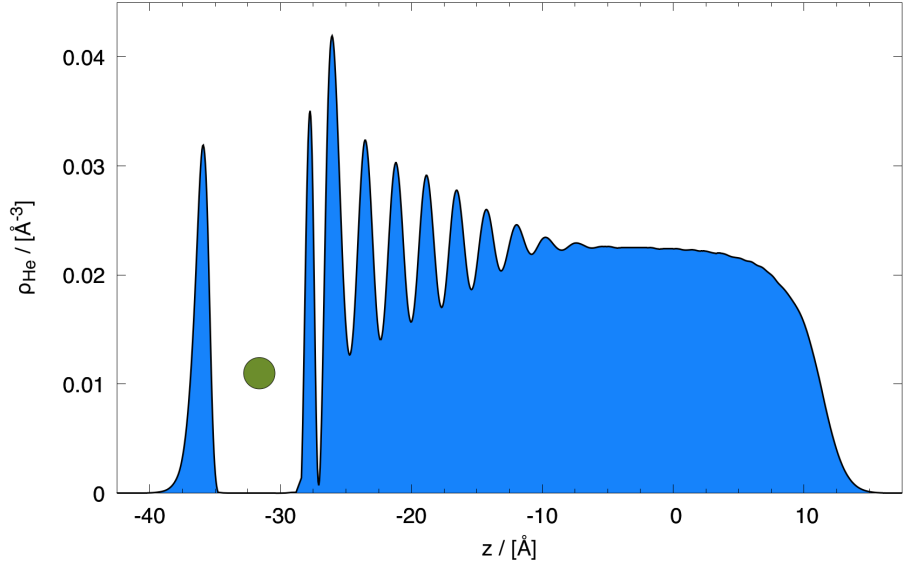


Figure 6.4: Density profile of the He_{1000} droplet along the incident direction corresponding to the Xe collision at $v_0 = 200$ m/s after 6 ps. (Color figure online.)

the motion of the impurity, with energy being transferred not only from the impurity to the droplet but also the other way around^[63].

The top left inset in Fig. 7.1 shows a snapshot obtained at the first turning point for $v_0 = 600$ m/s, with 57 He atoms around the Xe dopant. We have found that the Xe atom has to hit the droplet at a velocity above 600 m/s in order to go across the helium droplet, otherwise it remains attached to the droplet. The kinetic energy lost by the Xe atom is partially deposited in the droplet and partially carried away by prompt-emitted helium atoms, *i.e.* atoms expelled early on in the collision and with a significant kinetic energy. The number of He atoms emitted during the first 78 ps is about 47. For comparison, about 19 atoms are emitted after 185 ps for $v_0 = 200$ m/s. Eventually, the energy deposited into the droplet should be lost by atom evaporation; however, the time scale for this to happen is beyond the reach of any realistic simulation.

The piercing of the droplet by the Cs atom produces a density wave that travels on its surface and collapses at the surface region opposite to the hitting point. This collapse nucleates a vortex ring (the two dark spots in the 76 ps plot of the left panel of Fig. 7.2)^[? 1].

It is worth pointing out that the falloff of the Xe velocity in the $t = 20\text{--}30$ ps interval observed in Fig. 7.3 is due to the increase of its inertia due to the

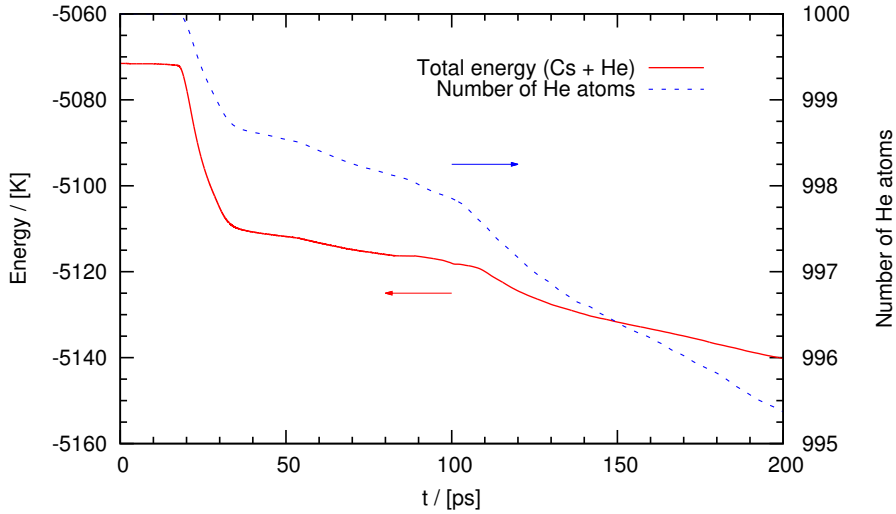


Figure 6.5: Total energy (left scale) and number of atoms in the droplet (right scale) as a function of time for the $\text{Cs}@\text{He}_{1000}$ system at $v_0 = 200$ m/s. (Color figure online.)

appearance of a dynamic “snowball” –a crust of helium atoms surrounding the Xe bubble indicated by the bright spots in Fig. 7.2– that is eventually washed out at larger times. At variance with our findings for Ba^+ ^[63], vortex rings have not been nucleated in the case of Xe; in particular, we have checked that the two dark spots in the 30 ps plot of the right panel of Fig. 7.2 for Xe do not correspond to a vortex ring.

The collapse of the Cs bubble at the surface of the droplet some 150 ps after the process gives back to the impurity part of the kinetic energy it has lost in the piercing of the droplet. The Cs atom is expelled at 64.5 m/s (corresponding to 33.6 K kinetic energy). The number of prompt-emitted helium atoms is 5, which is smaller than for Xe at the same collision energy (19 atoms). As revealed by Fig. 7.5, they are preferentially emitted as a forward burst (first sharp drop around 20 ps in the number of atoms) and as a backward burst (second sharp drop slightly after 100 ps).

Chapter 7

Capture by quantised vortices

7.1 Introduction

It is well established that helium droplets can readily capture in their interior almost any atom or molecule interacting with them, as first shown for the case of Ne atoms,^[50] with the notable exception of alkali^[64] and some alkaline-earth^[65] atoms. This property, together with the extremely low temperature (T) achieved in helium droplets – of the order of 0.4 K – makes them the perfect ultracold and inert environment for hosting and studying isolated atoms and molecules, which is at the basis of current applications of helium droplets for spectroscopic studies of atoms and molecules. Besides, the superfluid nature of helium facilitates binary encounters of atoms/molecules in the bulk of the droplet while absorbing the energy released upon recombination, making possible chemical reactions which would not otherwise occur in the gas phase. These unique properties of helium droplets have had a huge impact on their study.^[51,66–69]

The pickup of Ar, Kr and Xe atoms in the gas phase by ${}^4\text{He}_N$ droplets with $N > 10^3$ atoms produced by nozzle beam expansions was described about twenty years ago by Toennies and coworkers.^[70] In these experiments the droplets in the helium beam were deflected by impacting with a secondary beam made of rare gas atoms.

Recently, a technique has been introduced to determine the size of large He droplets ($N > 10^5$). It is based on the attenuation of a continuous droplet beam through collisions with Ar atoms at room temperature.^[61] The pickup chamber of the droplet beam apparatus is filled with argon gas and the helium droplets experience multiple, isotropic collisions with the Ar atoms on their way towards the detection chamber. Large helium droplets could also be doped in this way. This method, using Xe atoms,

has been instrumental for detecting and imaging quantized vortex arrays in helium droplets.^[57,58] Xe atoms were used in these experiments because of their large sensitivity to the x-ray coherent diffractive imaging employed to detect them within the helium droplets. Experiments with large superfluid helium droplets are reviewed in a recent publication.^[71]

The impurity-droplet interaction in the presence of vortices is also relevant as the first stage of a more complex process leading to the formation of nanowires, see e.g. refs.^[72? -74]. Long filaments made of micrometer-sized solid hydrogen particles trapped on quantized vortex cores were used to directly image the vortex reconnection between quantized vortices in superfluid helium.^[?]

The impact and capture of impurities interacting with pure helium droplets has been addressed recently within time-dependent density functional theory (TDDFT). Real time simulations have been carried out for heliophobic^[75] (Cs) and heliophilic^[76] (Ne) atoms. In addition to the TDDFT equation for ^4He , heavy impurities are treated as classical particles using Newton's equation of motion, whereas a time-dependent Schrödinger equation has been used in the case of light impurities within the mean field model.^[76,77] A comparison between the results for head-on collisions of Cs and Xe atoms –heliophobic and heliofilic atoms of similar mass– has been presented in ref.^[78].

In this work we present results obtained within TDDFT for the collision and capture of Xe and Ar atoms by a ${}^4\text{He}_{1000}$ droplet at different kinetic energies and impact parameters. Special attention is paid to the time-dependent interaction of Xe and Ar atoms with helium nanodroplets hosting vortex lines, and to the effect of multiply-doped vortex arrays in large helium droplets.

Due to the heavy computational cost of the TDDFT simulations presented here, we address only a few facets of the capture process that we consider of experimental relevance rather than carrying out a systematic study of the process. In particular:

- We study the capture of Xe atoms by a ${}^4\text{He}$ nanodroplet, both for head-on collisions and for different impact parameters, with velocities ranging from thermal values up to several hundred m/s. The results of peripheral collisions with different values of the impact parameter are used to estimate the cross section for the Xe capture.
- We study how a Xe atom dynamically interacts with a droplet hosting a vortex line, under different initial conditions resulting in different velocity regimes of the impurity as it collides with the vortex core: i) a Xe atom initially at rest on the droplet surface and sinking under the effect of solvation forces; (ii) a head-on collision of a moving Xe or Ar atom against

the ${}^4\text{He}$ nanodroplet.

- We study the stationary state of a large ${}^4\text{He}_{15000}$ droplet hosting a ring of six vortex lines, doped with Ar atoms completely filling all six vortex cores. This is the simplest system that mimics those experimentally described in ref.^[57], where doped vortex arrays embedded in rotating ${}^4\text{He}$ microdroplets have been imaged.

Multimedia materials accompany this paper, showing the real time dynamics of several impact/capture processes described here. These materials are presented in the electronic supplementary information (ESI†) document. They constitute an important part of this work, since often it is only by viewing how a complex microscopic process unfolds in real time that one can catch important physical details which would otherwise escape in a written account.

7.2 Results

The results presented in this work have been obtained using the 4He-DFT BCN-TLS computing package.^[?]

7.2.1 Xe capture by vortex-free droplets

We have simulated head-on collisions of a Xe atom with a ${}^4\text{He}_{1000}$ droplet at relative velocities v_0 ranging from 200 to 600 m/s. Figure 7.1 displays two-dimensional plots of the helium density for the highest value, $v_0 = 600$ m/s. This velocity is well above the range of velocities typically encountered in experiments.^[57,58,61] In spite of the appearance of disconnected helium density shown in the $t = 87$ ps frame, we have found that the Xe atom eventually turns around and is captured again inside the droplet even at that relatively high impact velocity. Note that the Xe impurity, even when it temporarily emerges from the bulk of the droplet, appears to be coated with a few ${}^4\text{He}$ atoms, see the configuration at 87 ps.

Figure 7.1 also shows the development of bow waves in the density profile, moving ahead of the impurity at supersonic velocity, and an incipient conic density wave front with its vertex at the Xe bubble. Similar conic shapes, characteristic of supersonic flows, are found when an impurity moves in bulk liquid helium. In the present case the limited size of the droplet and the loss of kinetic energy during the first stages of the collision smooth out this front, making it just barely visible in the figure.

For low initial velocities of the impurity, we find that Xe moves back and forth inside the droplet. The turning points are not fixed, because

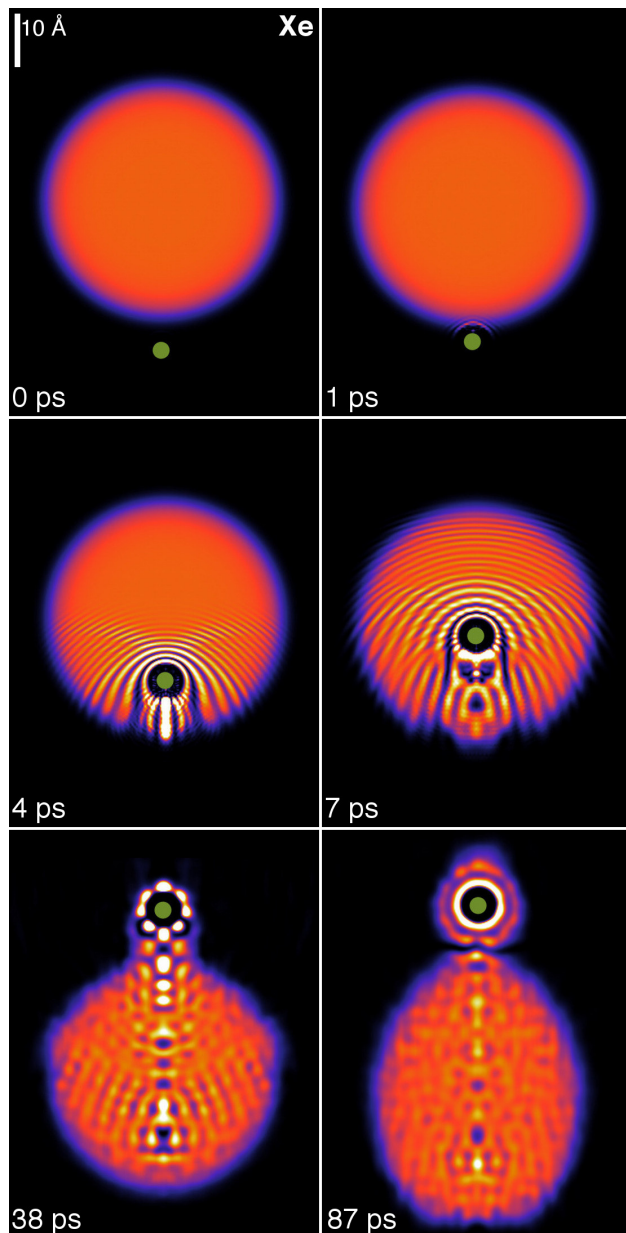


Figure 7.1: Dynamic evolution of a Xe atom (green dot) approaching the ${}^4\text{He}_{1000}$ droplet from below at $v_0 = 600$ m/s. The corresponding time is indicated in each frame. Bright spots correspond to high density regions.^[?]

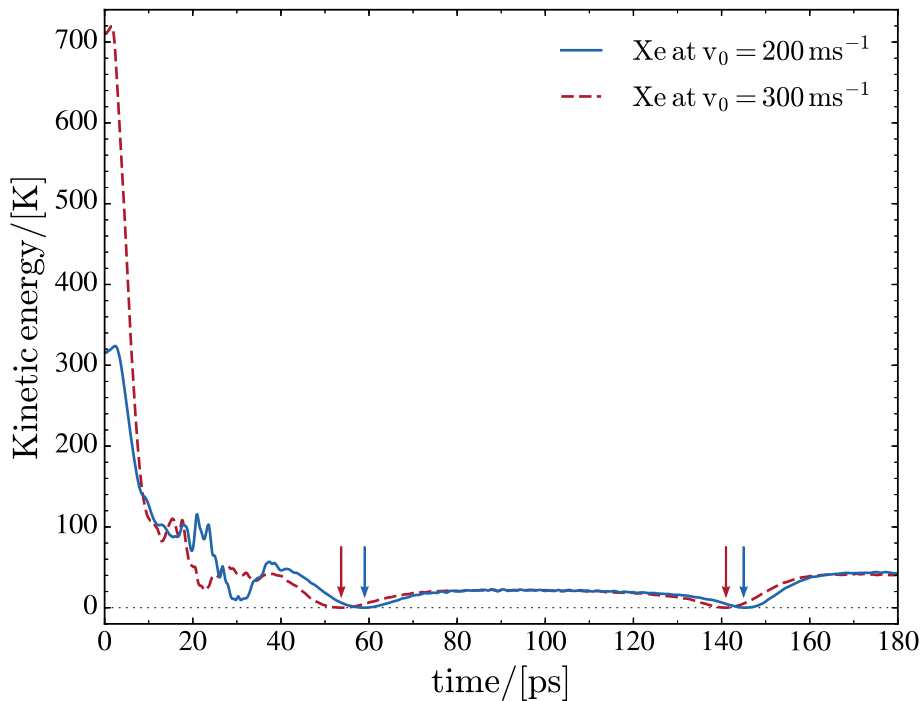


Figure 7.2: Kinetic energy of the Xe atom in the center of mass (COM) frame of the ${}^4\text{He}_{1000}$ droplet as a function of time for a head-on collision at $v_0 = 200$ and 300 m/s. The kinetic energy increase during the first few picoseconds is due to the acceleration produced by the attractive part of the Xe-He potential. The vertical arrows indicate the first two turning points inside the droplet.

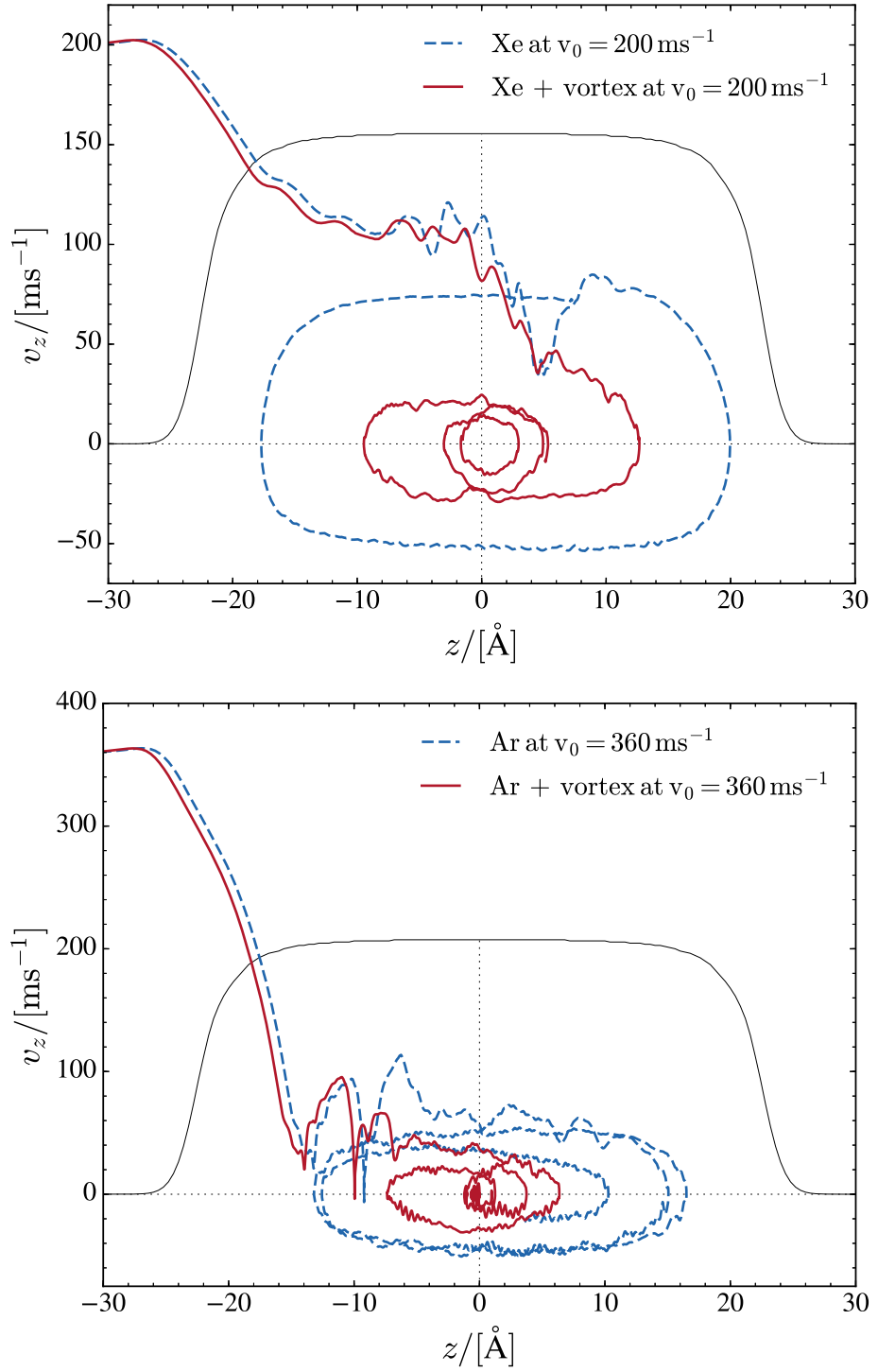


Figure 7.3: Top: Phase-space trajectory of Xe for a head-on collision at $v_0 = 200 \text{ m/s}$ against a ${}^4\text{He}_{1000}$ droplet with and without a vortex line. The Xe atom is referred to the COM frame of the droplet. Bottom: Same as top panel for Ar at $v_0 = 360 \text{ m/s}$. The droplet density at $t = 0$ is also represented in arbitrary scale (black profile)

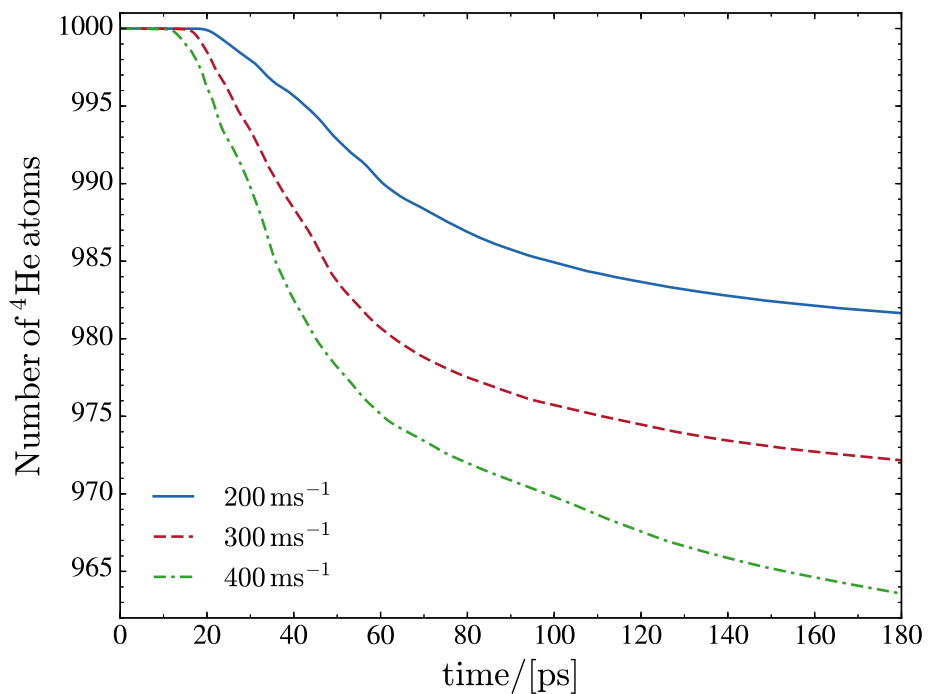


Figure 7.4: Number of He atoms remaining in the droplet as a function of time for the Xe against ${}^4\text{He}_{1000}$ collision at $v_0 = 200, 300$ and 400 m/s.

Table 7.1: Number of He atoms promptly ejected (N_e) and average energy per ejected atom (E_e) during the first 200 ps.

Species	v_0 (m/s)	N_e	E_e (K)
Xe	200	18	19
	300	28	23
	400	37	30
Ar	360	16	22

the droplet deforms due to the displacement of the Xe atom and to the waves that are continuously emitted by the moving impurity (mainly in the direction of its motion), hit the droplet surface, and are reflected back inside it.^[78] This is shown in Fig. 7.2 for $v_0 = 200$ and 300 m/s. Thermal Xe atoms ($v_0 \sim 240$ m/s) are used in the vortex imaging experiments,^[57,58] and the average droplet velocity as it travels through the pick-up chamber is about 170 m/s,^[61] corresponding to relative collision velocities which are within the range investigated here. The kinetic energy gained by the Xe atom after the turning point at 140–150 ps is precisely due to the fact that the droplet is not a rigid object and reacts to the motion of the impurity. As a consequence, energy is transferred not only from the impurity to the droplet but also the other way around. We want to emphasize that the droplet experiences large deformations rather than large displacements; the velocity of the center of mass (COM) of the droplet is rather small (below 6 m/s for $v_0 = 200$ and 300 m/s as well) due to the large mass difference between the impurity and the droplet.

We have found that most of the energy is transferred from the Xe to the droplet in the first stages of the collision. This is why, for collisions in this kinetic energy range leading to Xe capture, the motion of the impurity inside the droplet is independent on the initial kinetic energy to a large extent. This is shown in Fig. 7.3, which displays the trajectory of Xe (Ar) in phase space for $v_0 = 200$ (360) m/s. The figure also shows similar trajectories in the case where a vortex is present in the droplet; these cases will be discussed later in this paper.

The kinetic energy lost by the impurity atom is partly deposited in the droplet, where it produces large deformations and sound waves, and partly carried away by prompt-emitted helium atoms. These are atoms with a significant kinetic energy which are expelled from the droplet early on in the collision process. Fig. 7.4 shows the number of atoms remaining in the simulation cell as a function of time for collisions with Xe at $v_0 = 200, 300$ and 400 m/s. Eventually, the energy deposited into the droplet should be lost by atom evaporation. The energy carried away by the

ejected He atoms during the first 200 ps is collected in Table 7.1 for the head-on collisions described in this paper. For comparison, the calculated binding energy of a helium atom in the ${}^4\text{He}_{1000}$ droplet is 6.0 K. Note that helium atom ejection continues after 200 ps, the droplet still being far from “thermalized” (equilibrated).

In the case of heavy dopants it is possible to obtain a simple expression for their capture cross section. Defining

$$\kappa = \sqrt{\frac{2\mu E}{\hbar^2}} , \quad (7.1)$$

where μ is the reduced mass of the system and E is the available energy in the center-of-mass frame, and provided that the reduced de Broglie wave length of the impurity $\lambda/(2\pi) = 1/\kappa$ is much smaller than the dimensions of the droplet (which is the case for all v_0 in this study), the system behaves classically and^[75]

$$\sigma(E) = \frac{\pi}{\kappa^2} \sum_{\ell=0}^{\ell_{cr}} (2\ell + 1) = \frac{\pi}{\kappa^2} (\ell_{cr} + 1)^2 \quad (7.2)$$

where ℓ_{cr} is the largest relative angular momentum leading to the impurity capture. For a given energy, ℓ_{cr} is determined by carrying out simulations with different impact parameters b using $\ell = \mu v_0 b / \hbar$. We have done it for Xe at $v_0 = 200$ m/s. Figure 7.5 shows the simulation corresponding to the largest impact parameter among the ones we have calculated which led to Xe capture, $b = 20.3$ Å, and Fig. 7.6 shows the simulation corresponding to the smallest one which led to Xe deflection, $b = 22.2$ Å. The radius of the droplet, which is defined as $R = r_0 N^{1/3}$ with $r_0 = 2.22$ Å, is 22.2 Å for $N = 1000$. Hence, at this energy –well within the thermal conditions of the experiment– the cross section for Xe capture is very similar to the geometric droplet cross section.

The circulation lines of the superflow are displayed in two selected panels in Figs. 7.5 and 7.6. They show the flow pointing towards the approaching Xe atom at the beginning of the collision and the appearance of vortex loops in the droplet at the latest stages of the simulation. Vortex loops appear from local distortions of the droplet surface.^[79] The circulation lines displayed in the figures of this work have been drawn inside the region where the density is above $0.5 \rho_0$ (with $\rho_0 = 0.0218 \text{ \AA}^{-3}$) that defines the dividing surface of the droplet.

In peripheral collisions not only energy but also angular momentum is deposited into the droplet, which allows to visualize the irrotational flow

of the superfluid helium. In particular, for Xe at $v_0 = 200$ m/s and $b=22.2$ Å the initial angular momentum is $917 \hbar$. This collision was followed for some 220 ps and produced the ejection of 15 He atoms, 5 of them attached to the Xe atom, see Fig. 7.6. After the collision, the $\text{Xe}+{}^4\text{He}_5$ complex carries away 522 angular momentum units, while some 95 units are deposited in the droplet as vortex loops and capillary waves,^[?] see bottom right panel of Figs. 7.5 and 7.6. The remaining angular momentum is taken away by the ejected helium atoms.

7.2.2 Helium droplets hosting vortex lines

To determine the structure of a droplet hosting a singly-quantized linear vortex we have started the imaginary time iteration from a helium density in which the vortex is “imprinted”. For this purpose, a vortex line along the z can be described by the effective wave function

$$\Psi_0(\mathbf{r}) = \rho_0^{1/2}(r) e^{iS(\mathbf{r})} = \rho_0^{1/2}(\mathbf{r}) \frac{(x + iy)}{\sqrt{x^2 + y^2}} \quad (7.3)$$

where $\rho_0(\mathbf{r})$ is the density of either the pure or the impurity-doped droplet without vortex. Vortex lines along other directions passing through a chosen point can be imprinted as well.^[80]

In the case represented by Eq. (7.3), if the impurity is within the vortex core along a symmetry axis of the impurity-droplet complex, the effective wave function $\Psi_0(\mathbf{r})$ – before and after relaxation – is an eigenvector of the angular momentum operator $\hat{L}_z = -i \hbar \partial/\partial\theta$. The angular momentum of the droplet is then

$$\langle \hat{L}_z \rangle = \langle \Psi_0(\mathbf{r}) | \hat{L}_z | \Psi_0(\mathbf{r}) \rangle = N \hbar \quad (7.4)$$

Different energy balances involving pure and doped droplets hosting vortices are defined:^[60,80,81]

- Solvation energy of the impurity:

$$S_X = E(X@{}^4\text{He}_N) - E({}^4\text{He}_N)$$

- Vortex energy:

$$E_V = E(V@{}^4\text{He}_N) - E({}^4\text{He}_N)$$

- Binding energy of the impurity to the vortex:

$$B_X = S_X - \{E[(X + V)@{}^4\text{He}_N] - E(V@{}^4\text{He}_N)\}$$

Using the functional of ref.^[82] and the He-rare gas pair potentials of ref.^[?], solvation energies of -316.3 K and -215.7 K have been found for Xe and Ar atoms, respectively. Thus, for the same incident kinetic energy, about 100 K of additional energy have to be dissipated in the case of Xe in order to get the same kinematic conditions than for Ar.

The binding energy of the impurity to the vortex is the result of a delicate balance between terms which are individually much larger than their difference. It can thus be affected by relatively large inaccuracies. Within DFT, it has been found that the Xe atom is barely bound to the vortex line, with $B_{Xe} \sim 3 - 5$ K.^[59,81]

A critical angular velocity ω_c exists above which nucleation of vortices with quantized velocity circulation in units of \hbar/m_4 occurs. The critical angular velocity for nucleating a vortex line along a diameter in a droplet made of N helium atoms is

$$\omega_c = \frac{1}{\hbar} \frac{E_V}{N} \quad (7.5)$$

This expression is obtained by computing the energy that minimizes $\langle H - \omega L_z \rangle$ (*i.e.* corresponding to the equilibrium configuration in the corotating frame) with and without a vortex line. Using the values appropriate for a ${}^4\text{He}_{1000}$ droplet we obtain $\omega_c = 0.127 \text{ K}/\hbar = 0.0167 \text{ ps}^{-1}$.

When the angular velocity is increased above ω_c , larger amounts of angular momentum may be stored into the superfluid by increasing the number of nucleated vortices. The higher the angular velocity, the more packed the vortex array is around the rotation axis. These vortices arrange themselves into ordered structures whose existence in bulk superfluid ${}^4\text{He}$ was established long ago.^[83?]

To generate vortex arrays we have worked in the fixed-droplet frame of reference (corotating frame at angular velocity ω), *i.e.* we look for solutions of the following EL equation:

$$\{\mathcal{H}[\rho] - \omega \hat{L}_z\} \Psi(\mathbf{r}) = \mu_4 \Psi(\mathbf{r}), \quad (7.6)$$

In this case, $\Psi(\mathbf{r})$ no longer is an eigenvector of the angular momentum. To determine $\Psi(\mathbf{r})$ describing a configuration where n_v vortex lines are present we have followed again the imprinting strategy, starting the imaginary-time evolution of Eq. (7.6) with the helium effective wave function

$$\Psi_0(\mathbf{r}) = \rho_0^{1/2}(\mathbf{r}) \prod_{j=1}^{n_v} \left[\frac{(x - x_j) + i(y - y_j)}{\sqrt{(x - x_j)^2 + (y - y_j)^2}} \right] \quad (7.7)$$

where $\rho_0(\mathbf{r})$ is the density of the vortex-free droplet and (x_j, y_j) is the initial position of the j -vortex linear core with respect to the z -axis of the droplet (note that in refs.^[59,60] $\Psi_0(\mathbf{r})$ was incorrectly written). We underline the fact that during the functional minimization of the total energy, the vortex positions and shapes will change to provide at convergence the lowest energy vortex configuration for the given value of the angular velocity ω .

Figure 7.7 shows the two-vortex stationary configuration of a ${}^4\text{He}_{100}$ droplet in the corotating frame at angular frequency $\omega = 0.175 \text{ K}/\hbar = 0.0229 \text{ ps}^{-1}$. The angular momentum of this configuration is $\langle \hat{L}_z \rangle = 1836 \hbar$. Notice the bending of the vortex line so that they meet the droplet surface perpendicularly at both ends, and also the flattening of the droplet in the z direction due to centrifugal forces.

At variance with the single vortex line along the symmetry axis of the droplet, the two-vortex configuration is not stationary in the laboratory frame, where the density and velocity field change with time. To show this, $\Psi(\mathbf{r})$ has been evolved in the laboratory for about 150 ps taking as initial condition the stationary configuration in the corotating frame. As expected, the vortex cores appear to rotate in the laboratory frame. Within the numerical accuracy, they do so rigidly. This can be seen in Fig. 7.7. Besides, they rotate precisely at $\omega = 0.0229 \text{ ps}^{-1}$. This is a stringent test on the accuracy of the dynamics and the consistency of the method. It can be seen in the ESI† material how the two vortex lines turn around each other.

Figure 7.7 shows how a superfluid droplet hosting a vortex array “rotates”. The fact that the vortex cores rotate rigidly is not in contradiction with the irrotational character of the superfluid flow, since they are empty. The cores carry along with them the superfluid whose velocity field is irrotational, whereas for a rigid solid or a classical liquid in steady flow one has $\mathbf{v} = \omega \times \mathbf{r}$, hence $\nabla \times \mathbf{v} = 2\omega$. The circulation lines in Fig. 7.7 do not correspond to a rigid rotation, but to an irrotational flow in the presence of two vortices. The helium density adapts to the vortex cores as they rotate and this gives the appearance of a solid rotation in the laboratory frame, but it is not.

It is worth discussing the different configurations that may appear when $\omega < \omega_c$. The lowest energy corresponds to the current-free (CF) $\langle L_z \rangle = 0$ configuration. Metastable one-vortex (1V) configurations with $\langle L_z \rangle = N\hbar$ also exist in this angular frequency range.^[59,60] Other irrotational (IR) configurations with $\langle L_z \rangle < N\hbar$ do exist, arising from velocity potentials such as e.g. $S(\mathbf{r}) = \alpha xy$. For an ellipsoidal droplet with a sharp surface, the parameter α is related to the angular velocity around the z -axis and the deformation of the ellipsoid, see the Appendix and refs.^[? ? ?].

These IR configurations may be generated by using the phase $S(\mathbf{r}) =$

αxy in Eq. (7.3) and minimizing $\langle H - \omega \hat{L}_z \rangle$. At a given value of $\omega < \omega_c$, the energies in the corotating frame are ordered as $E_{CF} < E_{IR} < E_{1V}$. Fig. 7.8 shows the stationary configuration in the corotating frame corresponding to $\omega = 0.10 \text{ K}/\hbar = 0.0131 \text{ ps}^{-1}$. Although this angular frequency is close to ω_c , this configuration is hardly distorted and hosts a negligible amount of angular momentum: less than $5 \times 10^{-2} \hbar$, compared to the value of $10^3 \hbar$ at ω_c). The circulation lines can be analytically calculated if the density profile is approximated by that of an ellipsoid with constant density, see the Appendix.

Figures similar to Fig. 7.8 are shown in refs.^[? ?] for a rotating elliptic vessel filled with a fluid whose flow is irrotational. Whereas in the case of a rigid solid or viscous liquid in steady flow the entire system rotates as a whole, an irrotationally flowing fluid in a rotating vessel is just pushed by the walls of the container; the same happens for a Bose-Einstein condensed gas in a rotating trap.^[?] For an isolated self-bound ${}^4\text{He}$ droplet, the apparent “rotation” of the system in the laboratory arises from deformations of the fluid elements constituting the droplet, but not from their local rotation which is forbidden by the irrotational condition. The vorticity Ω [defined in hydrodynamics as^[?] $\Omega = \nabla \times \mathbf{v}(\mathbf{r})$], initially distributed in the helium droplet when it is in the normal phase, concentrates in the vortex lines when the droplet becomes superfluid and its velocity field becomes irrotational.

The above discussion shows how difficult is to set a superfluid droplet in rotation. Experimentally^[57,58,84] the situation is different, since the helium droplet is initially in a normal phase state at a temperature above the normal-to-superfluid transition temperature T_λ (about 2.17 K in bulk liquid at 1 bar). As a consequence, it may store large amounts of angular momentum and experience large deformations. Copious evaporation drives the droplet into a superfluid state at a temperature below T_λ and the angular momentum remaining in the droplet is then stored in vortex arrays that are being nucleated.

7.2.3 Dynamics of Xe and Ar capture by vortex lines

To study the interaction of an atomic impurity with vortices, we have imprinted a vortex line in the ${}^4\text{He}_{1000}$ droplet and prepared the Xe atom in different kinematic conditions.

The inelastic scattering of xenon atoms by quantized vortices in superfluid bulk helium has been addressed in ref.^[85]. It was found that a head-on collision leads to the capture of Xe by the vortex line for $v_0 = 15.4 \text{ m/s}$, but not for $v_0 = 23.7 \text{ m/s}$. We have carried out an equivalent simula-

tion by initially placing the Xe atom inside the droplet 10 Å away from the vortex line and sending it head-on towards the vortex at a velocity of 10 m/s. This velocity is of the order of the thermal velocity of a Xe atom in a droplet under experimental conditions, once the droplet has thermalized after capturing the Xe atom ($T \sim 0.4$ K).^[51] Since the equilibrium position of the Xe atom is at the center of the droplet, it moves to this region and remains there during the rest of the simulation. In this region of the droplet, the Xe atom is also attracted by the vortex, but it is deflected by the superfluid flow around the vortex line and ends up orbiting around it. Hence it is captured by the vortex without getting into its core.

A detailed analysis of the Xe capture as a function of the impact parameter has also been carried out in ref.^[85], with the conclusion that when the impact parameter of the Xe atom approaching the vortex line is larger than about 5 Å, Xe is deflected but not captured.^[85] In the case of droplets, the final result is very different. Upon capture, the Xe atom wanders erratically inside the droplet, as we have seen in the case of vortex-free droplets. The surface of the droplet deforms dynamically and acts as a “pinball machine”, which eventually brings the Xe atom close enough to the vortex line if it missed it in the first attempt or was not previously ejected off the droplet.

The smoothest capture process one might think of corresponds to the Xe atom being initially placed at rest on the droplet surface, as no kinetic energy is given to the impurity. The Xe atom is accelerated towards the center of the droplet due to the attractive He-Xe interaction. We show that, under these kinematic conditions, some He atoms are first drawn towards the impurity because they are lighter, see also Figs. 7.9 and 7.10 in ref.^[?]. Eventually, the impurity with its “solvation structure” sinks, acquires some velocity, and is also deflected by the velocity field of the vortex line.

We have tried two different initial locations of the Xe atom on the droplet surface. One is a point on the equator of the droplet, in a plane perpendicular to the vortex line; the other location is one of the open vortex core ends. Our aim was to see if a sensible difference in the transit time of Xe across the droplet could be detected. The simulations do not show important differences between the time taken by the impurity to reach the center of the droplet. It is about 20 % larger when Xe starts from the equator than from the core end.^[?] It is worth noting that in the latter case the sliding of the impurity along the core proceeds rather smoothly, and that the impurity oscillates back and forth much as in the vortex-free case.

The simulation of Xe ($v_0=200$ m/s) and Ar ($v_0=360$ m/s) atoms head-on colliding with a ${}^4\text{He}_{1000}$ droplet perpendicularly to the vortex line has been

analyzed and compared with the result corresponding to a vortex-free droplet. The trajectory of the Xe and Ar atoms in phase space is shown Fig. 7.3. In both cases the trajectory of the impurity is limited to the region of the droplet around the vortex line. The impurity orbits around the vortex line because the superfluid flow does so. Since in the DFT approach no dissipation is included, the signature of the capture of an impurity by a vortex is its close orbiting around the vortex line, as shown in the figure and especially in ref.^[?]. The ESIT material shows that whereas Ar is captured during its first transit across the droplet, the Xe atom is only captured in its second transit. We attribute this difference to the larger solvation energy of Xe (see Sec. 3.2), which requires more time to be dissipated. It can be seen^[?] that when Xe detaches from the vortex in the first transit, the vortex line is reconnected near the atomic solvation structure because no open ends can remain in the bulk of the droplet.

Figures 7.9 and 7.10 show that when the impurity hits the droplet surface a series of surface and volume density waves are launched. These waves travel much faster than the impurity itself, which has lost a large amount of kinetic energy when it pierced the surface.

The displacement of the atom in the droplet produces sound waves in the liquid and distortions along the vortex line (Kelvin modes). It is worth seeing that before the bending by the collision with the impurity, the vortex line is twisted (helical Kelvin mode). This is due to the interference between the spherical wave front flow produced by the hitting of the droplet surface, that travels from bottom to top, and the flow around the vortex core. The spherical wave front hits first the central portion of the vortex line, whose ends are anchored on the droplet surface. This yields the appearance of the helical distortion along the vortex line shown in Fig. 7.11. The twisting can no longer be followed after the impurity solvation structure reaches the vortex line, bending and dragging it along in the course of its orbiting around it. But it is clearly visible before as shown in Fig. 7.11, that displays the density of the droplet around the vortex line at the indicated collision time.

We have thus shown that Xe and Ar atoms are readily captured by vortex lines in helium droplets under conditions prevailing in the experiments.^[57,58] Simulating the capture of a huge number of impurities or clusters by vortex arrays in very large droplets is beyond reach at present. However, the results presented in this subsection are the proof of concept that the limitation is technical and not conceptual.

7.2.4 Vortex arrays in ${}^4\text{He}$ droplets doped with Ar atoms

The existence of ordered vortex lattices inside ${}^4\text{He}$ droplets has been established by the appearance of Bragg patterns from Xe clusters trapped inside the vortex cores in droplets made of $N = 10^8 - 10^{11}$ atoms (corresponding to radii from 100 to 1000 nm).^[57,58] We have recently studied the stability of vortex arrays made of up to $n_v = 9$ vortices inside a ${}^4\text{He}$ nanodroplet using the DFT approach.^[60] It was found that the energetically favored structure for $n_v > 6$ is a ring of vortices encircling a vortex at the center of the droplet. For $n_v = 6$, the configuration with a six-vortex ring is found to have almost the same energy as the five-fold ring plus a vortex at the center. The former structure has been experimentally observed,^[57,58,84] although classical vortex theory predicts for it a much higher free energy cost than for the latter.^[?] Similar equilibrium structures have been obtained within DFT for helium nanocylinders hosting vortex arrays.^[59]

In the experiments of ref.^[58] the diffraction images show that rotating ${}^4\text{He}$ nanodroplets of about 200 nm in diameter contain a small number of symmetrically arranged quantum vortices whose cores are filled with regularly spaced Xe clusters. Unexpected large distances of the vortices from the droplet center ($\sim 0.7 - 0.8$ droplet radii) are observed and explained as a result of the balance between the contribution of the Xe atoms to the total angular momentum of the droplets and the solvation potential of the embedded Xe atoms, which opposes the migration of vortices towards the droplet surface and their annihilation there, as it would happen instead in the case of undoped vortices for low values of the droplet rotational frequency.

In practice, as more and more Xe atoms become attached to a vortex, they adopt the angular velocity of its revolution about the droplet center. If the Xe capture is isotropic, the total angular momentum of the droplet is conserved, and thus the angular momentum accompanying the Xe rotational motion must be transferred from the vortices to the impurities. This reduction in the angular momentum of the vortices causes them to move outwards, resulting in the larger equilibrium distances of the vortices observed in the experiments. The actual equilibrium radial positions result from a balance between this tendency to move towards the droplet surface and the solvation potential, which tends instead to draw impurities towards the droplet center.

We have looked for stationary configurations of a 6-vortex ring in a rotating He_{15000} droplet by solving the EL equations in the corotating frame with a fixed angular velocity. Each vortex core is filled with Ar atoms, and the system is allowed to fully relax. In the end, the column of atoms inside

each vortex core reaches an equilibrium structure where the Ar atoms are separated by a distance which is roughly that of the Ar dimer. One such configuration is shown in Fig. 7.12. Note that the vortex cores are almost straight lines, whereas in an undoped droplet rotating with the same velocity the vortex lines would be bent, as shown e.g. in Fig. 7.7. The Ar atoms are not shown in the Figure. The localized structures appearing in the vortex cores are regions of highly inhomogeneous, high ^4He density resulting from the Ar-He attractive potential.

The presence of impurities thus confers rigidity to the vortex lines, preventing them from bending. Yet, the small segment of the vortex line free from impurities bends so as to hit the droplet surface perpendicularly, see the bottom Fig. 7.12. Note that in the absence of vortices, Ar atoms initially placed in a linear chain structure would relax towards the lower energy, compact configuration of an Ar cluster in the bulk of the droplet. However, once trapped by a vortex core, their collapse into such a cluster structure does not occur, i.e. an energy barrier appears and prevents the formation of Ar clusters. Our simplified description of the more complex experimental conditions (where each vortex line hosts chains of regularly spaced atomic clusters, instead of chains of single atoms) is due to computational limitations.

Our choice of Ar instead of Xe as a dopant is motivated by the weaker He-Ar and Ar-Ar interactions, which facilitates the imaginary-time relaxation. The interaction of the helium environment with several close-by impurities increases the strength of dopant-droplet interaction, producing helium localization around the impurities (snowball structures), see Fig. 7.9. Stabilizing these structures is extremely time consuming, especially when the He-impurity interaction is strong. Experiments were also carried out with Ar atoms as dopants, but have not been analyzed yet.^[?] However, no significant difference is expected between argon and xenon, neither from the experimental nor from the theoretical viewpoint.

There are obvious differences in scales between our simulations and the actual experiments, due to computational cost. In experiments heavier impurities are used (Xe), the droplets are much larger and the doping is known to occur by filling the vortex cores with a chain of equally spaced Xe clusters, each made of hundreds of atoms, instead of atom chains as done in our simulations. In spite of these differences, we find results which qualitatively explain the unusual behavior of vortex lines experimentally observed in doped rotating helium droplets.

We have looked for the equilibrium structure of the Ar@6-vortex $^4\text{He}_{15000}$ droplet for different imposed values of the angular velocity of rotation. The results show that the doping inside each vortex core adds a substantial sta-

bility to the system, such that doped vortices are still stable in a droplet rotating at rather low values of the angular velocities, whereas undoped vortices for such values would be pushed towards the surface of the droplet and eventually expelled. The solvation potential effect becomes apparent below some critical value of the angular velocity, where the vortices cease to move towards the surface and the system reaches an equilibrium maximum distance of the vortices from the droplet center. This is shown in the Fig. 7.13, where we plot the radial distance of the vortices from the center as a function of the angular momentum of the system. Note how doped vortices are stable for values of the angular momentum well below the stability limit of an undoped droplet. A similar behavior has been observed in the experiment (see for instance Fig. 2 in the Supplemental Material of ref.^[58]).

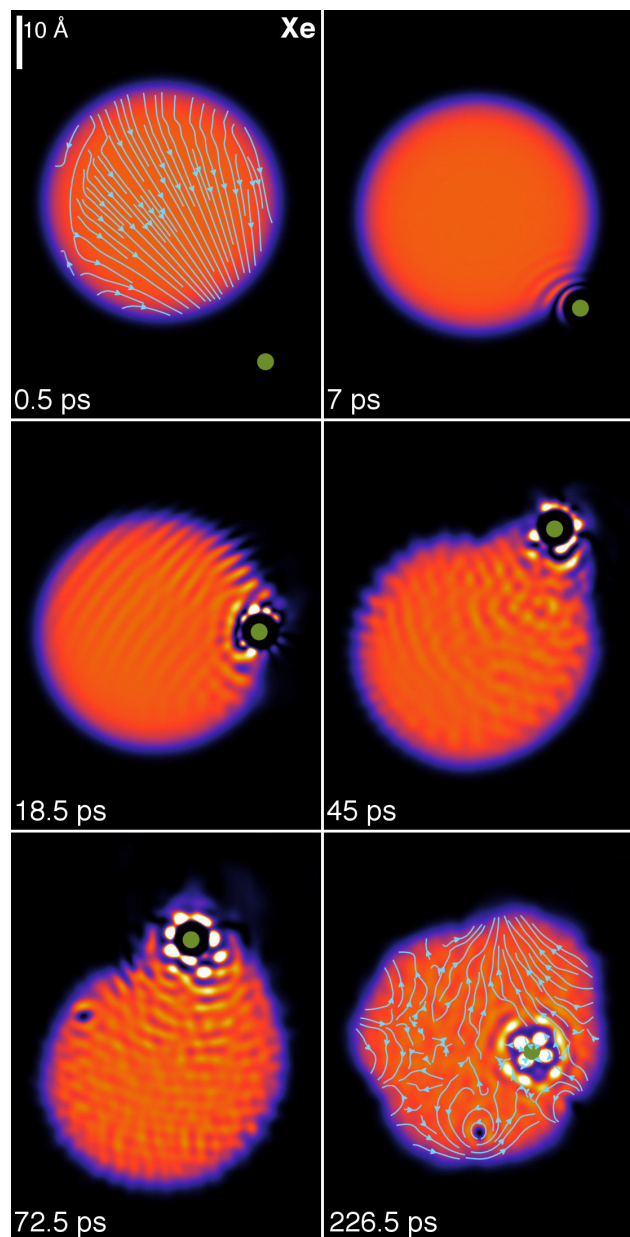


Figure 7.5: Dynamic evolution of a Xe atom (green dot) approaching the ${}^4\text{He}_{1000}$ droplet from below at $v_0 = 200$ m/s with impact parameter $b = 20.3$ Å. The corresponding time is indicated in each frame.^[?]

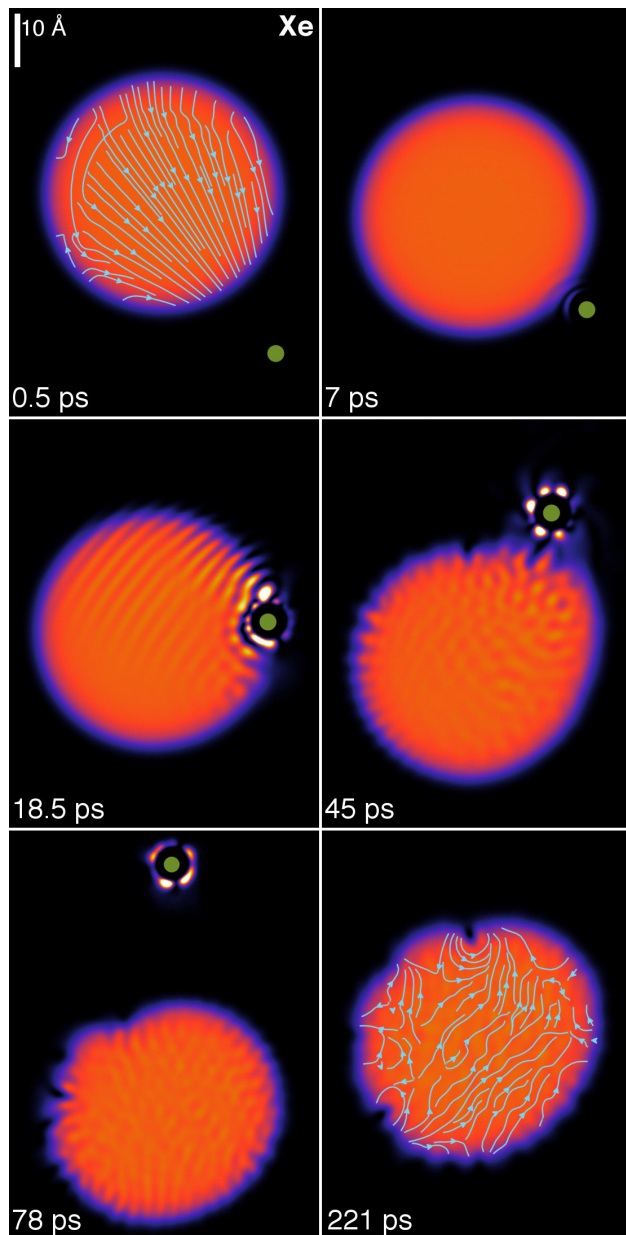


Figure 7.6: Dynamic evolution of a Xe atom (green dot) approaching the ${}^4\text{He}_{1000}$ droplet from below at $v_0 = 200$ m/s with impact parameter $b = 22.2$ Å. The corresponding time is indicated in each frame.^[?]

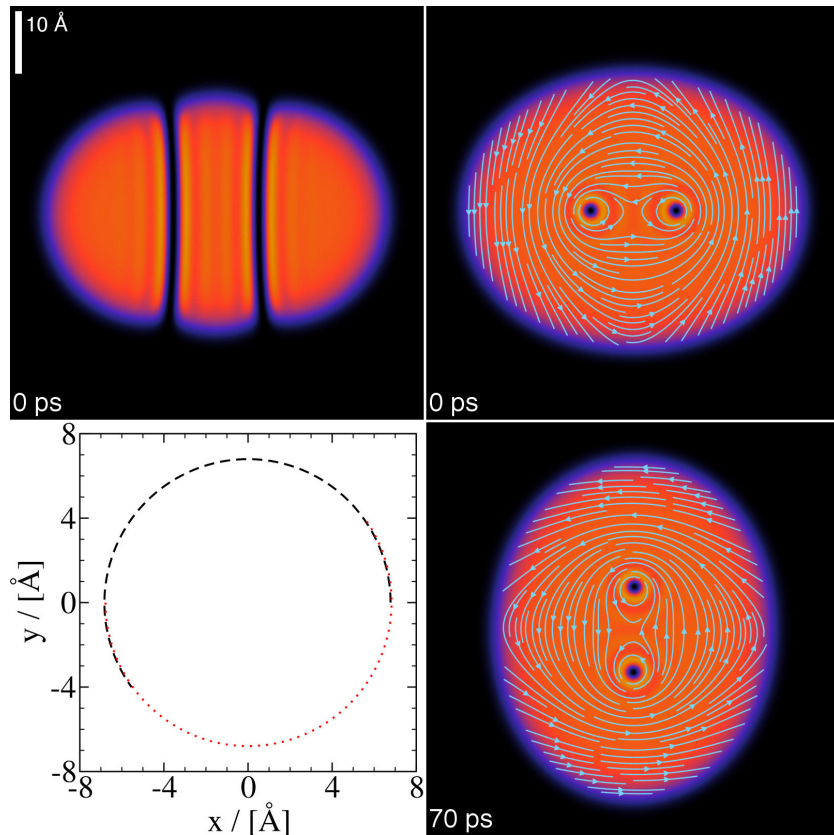


Figure 7.7: ${}^4\text{He}_{1000}$ droplet at $\omega = 0.0229 \text{ ps}^{-1}$: Top panels, stationary two-vortex configuration on the $x - z$ plane (left) and $x - y$ plane (right) in the corotating frame. Bottom left panel, trajectory of the vortex cores in the $x - y$ plane of the laboratory frame. The dashed line is the trajectory of one of the vortex cores, and the dotted line that of the other. Both trajectories overlap for a rigid rotation of the cores. Bottom right panel, helium density in the $x - y$ plane at $t = 70 \text{ ps}$ obtained in the laboratory frame starting from the above configuration.^[2]

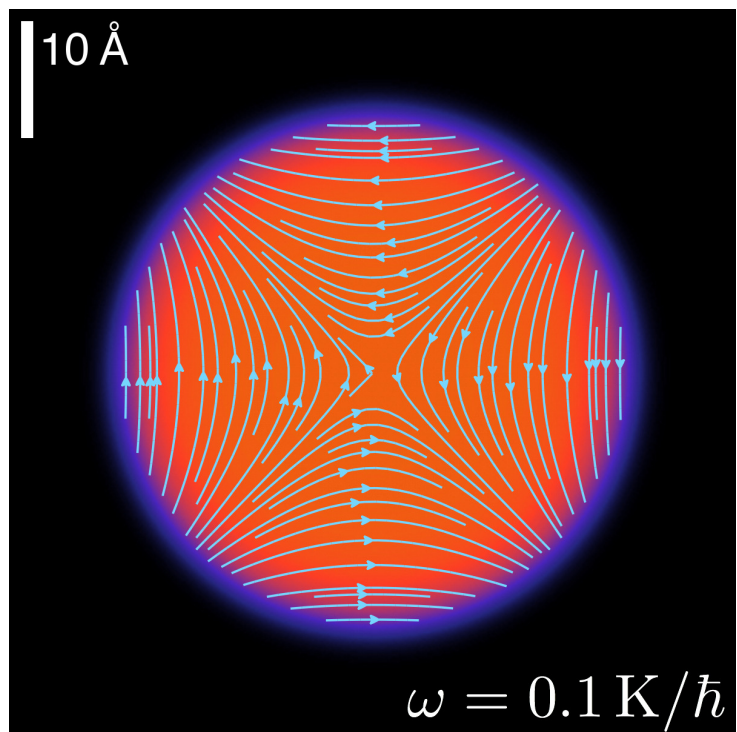


Figure 7.8: Stationary configuration of the ${}^4\text{He}_{1000}$ droplet at $\omega = 0.10 \text{ K}/\hbar = 0.0131 \text{ ps}^{-1}$ in the corotating frame ($x - y$ plane).

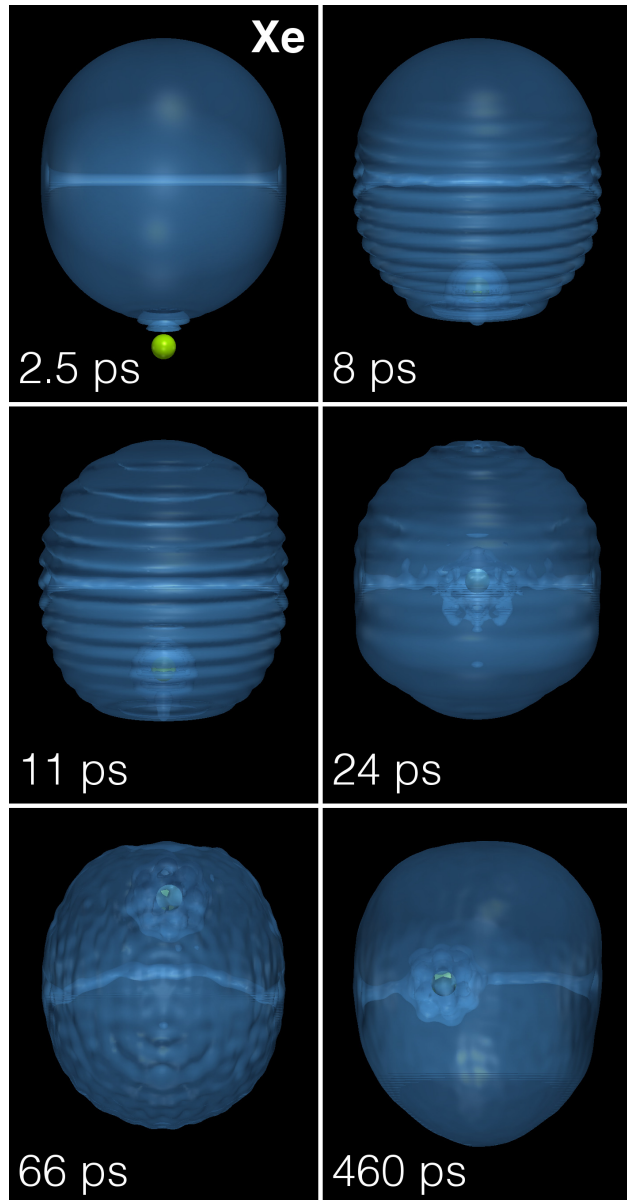


Figure 7.9: Dynamic evolution of a Xe atom (green dot) approaching a ${}^4\text{He}_{1000}$ droplet hosting a vortex line from below at $v_0 = 200$ m/s. The corresponding time is indicated in each frame.^[?]

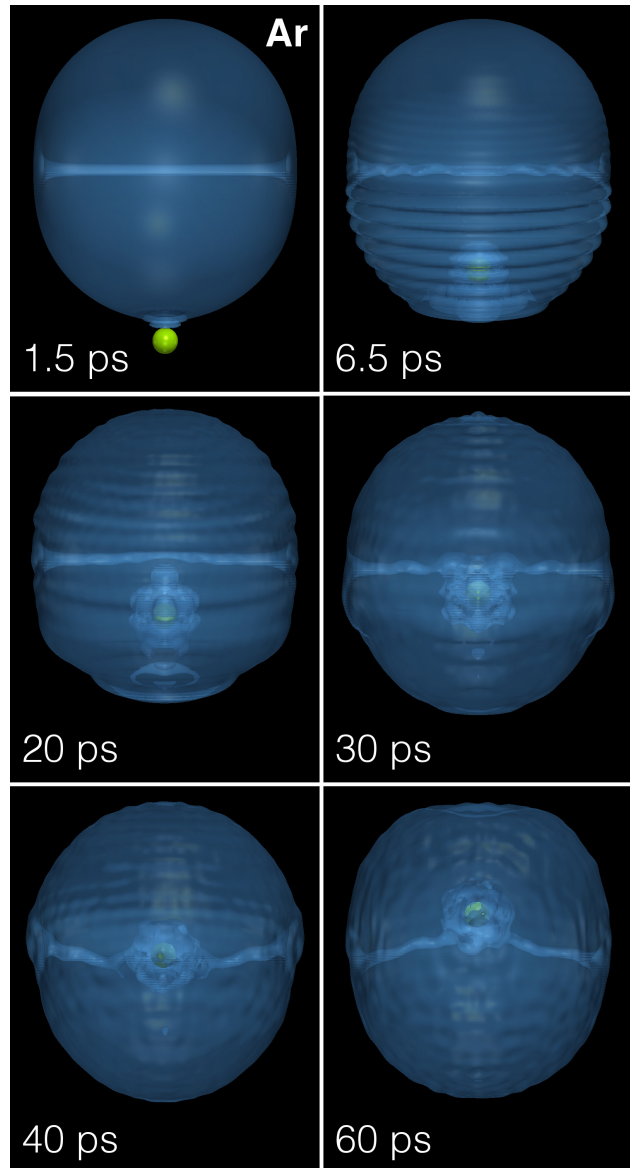


Figure 7.10: Dynamic evolution of an Ar atom (green dot) approaching a ${}^4\text{He}_{1000}$ droplet hosting a vortex line from below at $v_0 = 360$ m/s. The corresponding time is indicated in each frame.^[?]

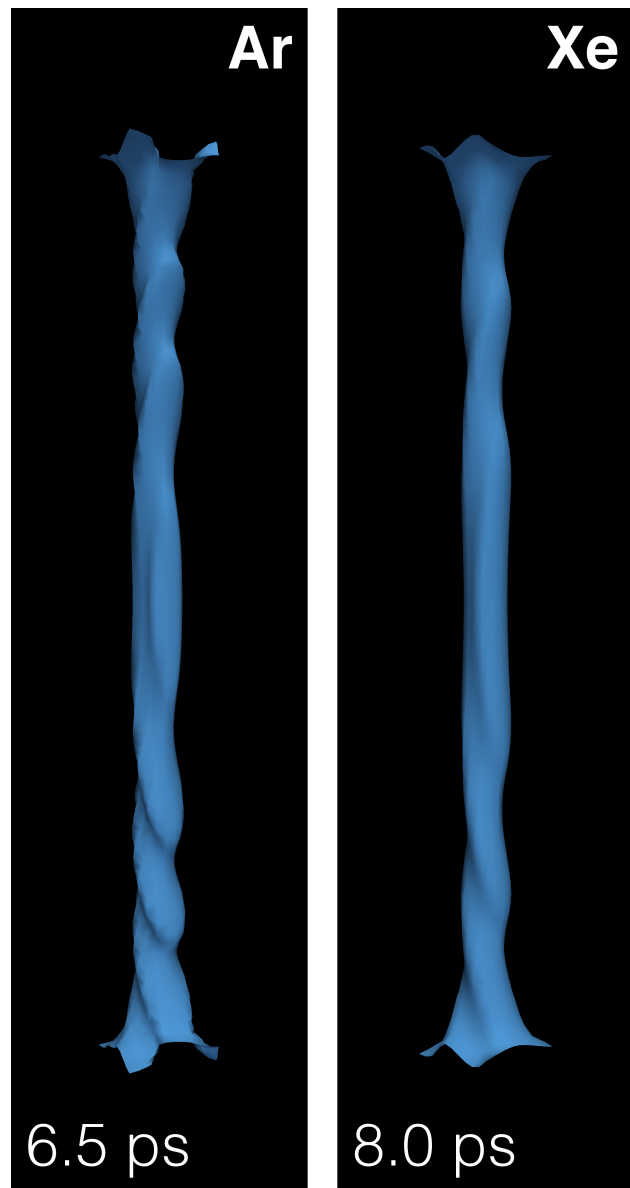


Figure 7.11: Core structure of the vortex line in a ${}^4\text{He}_{1000}$ droplet after colliding with Xe at $v_0=200$ m/s (right panel, $t = 8$ ps) and Ar at 360 m/s (left panel, $t=6.5$ ps). The full structure of the droplet is shown in Figs. 7.9 and 7.10.

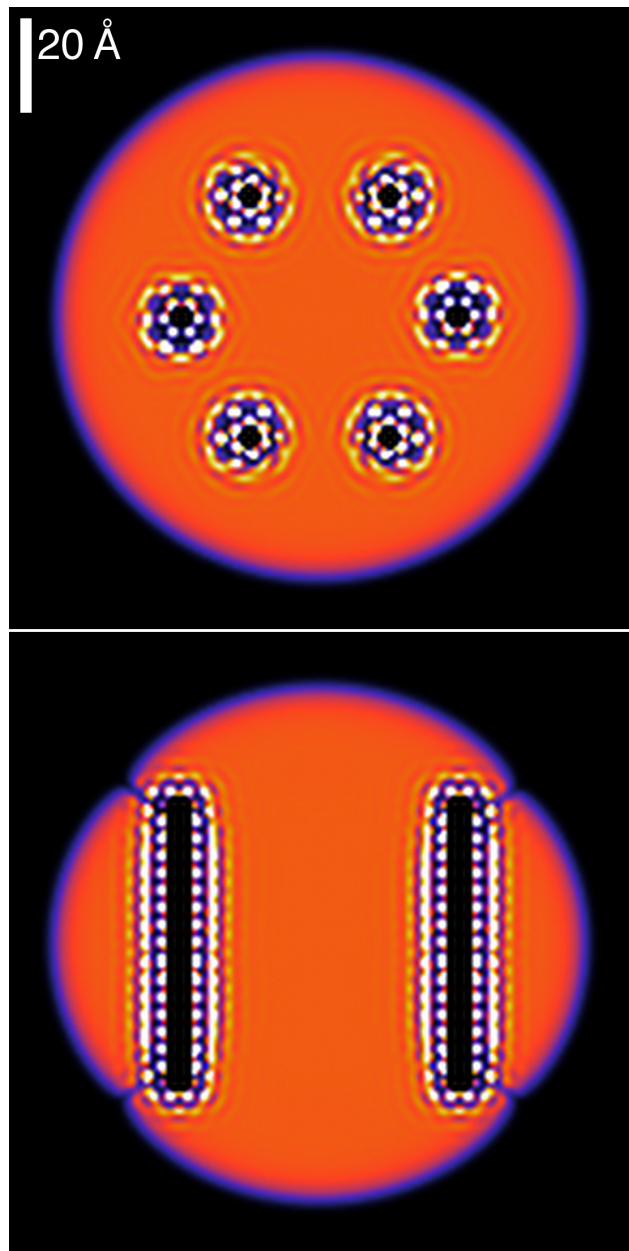


Figure 7.12: Helium droplet configuration hosting six vortices, each doped with a line of regularly spaced Ar atoms (not represented). The top figure shows the density in the $x - y$ symmetry plane (top view), while the bottom figure shows a side view corresponding to the $y - z$ plane. As in some of the previous figures, the bright spots are high density blobs appearing around the impurity atoms.

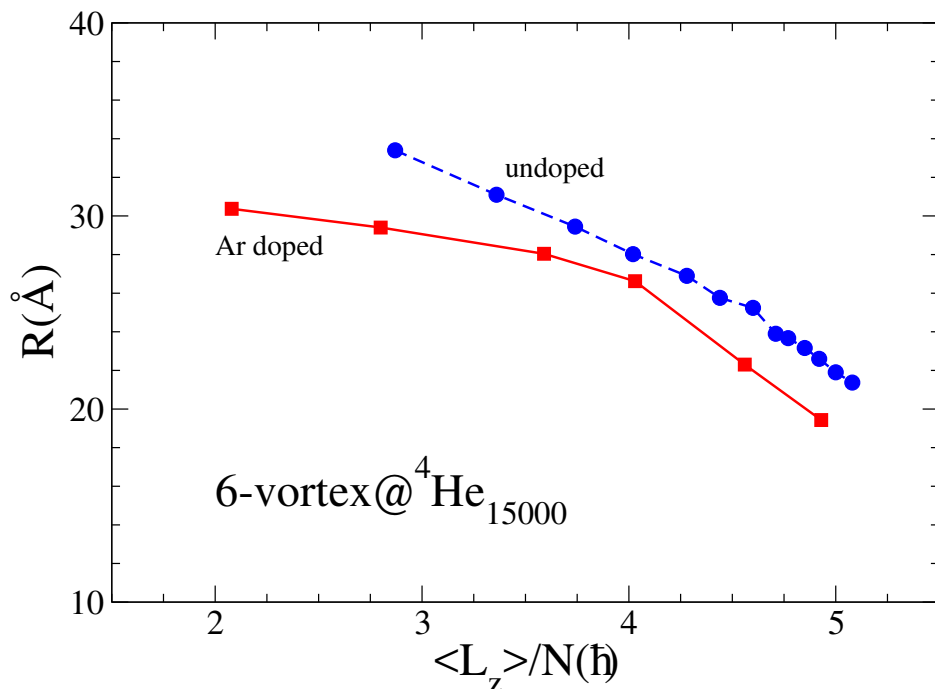


Figure 7.13: Calculated equilibrium distance of the 6-vortex ring from the droplet center as a function of the angular momentum per He atom in units of \hbar . The dots represent the results for undoped vortices, while the squares are the results for Ar-doped vortices. The lines are drawn as a guide to the eye.

Chapter 8

Conclusions & Outlook

8.1 Head-on collisions

In conclusion, head-on collisions of xenon, a heliophilic atom, involve a kinetic energy exchange of the same order of magnitude as cesium, a heliophobic atom with similar mass. In both cases, this energy is largely dissipated by producing energetic waves in the droplet or it is carried away by promptly emitted helium atoms. The difference is that it takes a much higher velocity for xenon to go through the droplet and escape than for cesium, as could be expected. Also, density builds up around the xenon during the dynamics, whereas a bubble is created around cesium.

8.2 Capture

We have shown that Xe and Ar atoms at thermal velocities are readily captured by helium droplets, with a capture cross section similar to the geometric cross section of the droplet. Crucially for the subsequent capture of impurities by vortex lines, we have also shown that most of the kinetic energy of the impinging impurity is lost in the capture process during the first tens of picoseconds. This happens either by the ejection of prompt-emitted He atoms, or by the production of sound waves and large deformations in the droplet.

If the droplet hosts a vortex, slowly moving impurities are readily captured by the vortex line. Rather than being trapped inside the vortex core, the impurity is bound to move at a close distance around it. Besides the crucial energy loss when the impurity hits the droplet, the capture by the vortex is favored by a further energy transfer from the impurity to the droplet: large amplitude displacements of the vortex line – as shown in

the ESI \dagger accompanying this work – take place, constituting another source of the kinetic energy loss in the final stages of the capture. A related issue is the appearance of Kelvin modes in the vortex line, that is not only bent, but also twisted in the course of the collision.

If the kinematic conditions of the collision (kinetic energy and impact parameter) lead to the capture of the impurity by the droplet, the pinball effect caused by the droplet surface can induce the meeting of the Xe/Ar atom and the vortex line – and the possible capture of the atom by the vortex –, since both have a tendency to remain in the inner region of the droplet. We have shown this in the case of Xe at $v_0 = 200$ m/s: Xe is captured during its second transit across the droplet, whereas this could not have happened in bulk liquid helium.^[85]

The capabilities of the He-DFT approach might help elucidate processes of experimental interest, such as the capture of one or several impurities by large droplets hosting a vortex array and how several atomic impurities, impinging upon a rotating droplet hosting vortices, react to form small clusters, eventually being trapped within the vortex cores as it appears in the experiments.

Appendix A

Angular velocity and angular momentum

In this Appendix we discuss the relationship between angular velocity and angular momentum of a deformed droplet below the critical angular frequency for vortex nucleation.

Let us consider an ellipsoidal vessel filled with liquid ${}^4\text{He}$ uniformly rotating around the z axis, $\omega = \omega \hat{\mathbf{k}}$. The ellipsoid has the equation

$$F(x, y, z) = \frac{x^2}{R_1^2} + \frac{y^2}{R_2^2} + \frac{z^2}{R_3^2} - 1 = 0$$

If \mathbf{v} is the irrotational velocity of a point in the laboratory, \mathbf{v}' the velocity of the same point in the vessel (corotating frame), and $\mathbf{V} = \omega \times \mathbf{r}$, one has

$$\mathbf{v}' = \mathbf{v} - \mathbf{V} = \frac{\hbar}{m_4} \nabla S - \omega \times \mathbf{r}$$

where S is the velocity potential defined here so as that

$$\mathbf{v} = \frac{\hbar}{m_4} \nabla S(x, y, z)$$

Its existence is granted by irrotationality; we also have $\mathbf{V} = \omega \times \mathbf{r} = \omega(-y, x, 0)$. A vector perpendicular to the ellipsoid surface is $\mathbf{n} = \nabla F(x, y, z)$. From the stationarity condition $(\mathbf{v}' \cdot \mathbf{n})|_{surf} = 0$ one obtains

$$\begin{aligned} \mathbf{v}' \cdot \mathbf{n} = 0 &= \left(\frac{\hbar}{m_4} \frac{\partial S}{\partial x} + \omega y \right) \frac{x}{R_1^2} \\ &+ \left(\frac{\hbar}{m_4} \frac{\partial S}{\partial y} - \omega x \right) \frac{y}{R_2^2} + \left(\frac{\hbar}{m_4} \frac{\partial S}{\partial z} \right) \frac{z}{R_3^2} \Big|_{surf} \end{aligned}$$

It can be checked that $\mathcal{S} = \alpha xy$ is a solution to this equation provided that

$$\frac{\hbar}{m_4} \left(\frac{1}{R_1^2} + \frac{1}{R_2^2} \right) \alpha = \left(\frac{1}{R_2^2} - \frac{1}{R_1^2} \right) \omega$$

Hence,

$$\alpha = \frac{m_4}{\hbar} \left(\frac{R_2^2 - R_1^2}{R_1^2 + R_2^2} \right) \omega$$

and

$$\mathcal{S} = \frac{m_4}{\hbar} \left(\frac{R_2^2 - R_1^2}{R_1^2 + R_2^2} \right) \omega xy$$

The velocity in the laboratory is $\mathbf{v} = (\hbar/m_4)\nabla\mathcal{S} = (\hbar/m_4)\alpha(y, x, 0)$, and in the vessel (corotating frame) is $\mathbf{v}' = \beta(R_1^2y, -R_2^2x, 0)$, where $\beta \equiv 2\omega/(R_1^2 + R_2^2)$. Once they have been determined, their circulation lines are straightforwardly obtained. In the laboratory frame they are

$$x^2 - y^2 = c ,$$

which is the appearance of the circulation lines displayed in Fig. 7.8. In the vessel frame, they are

$$\frac{x^2}{(\xi R_1)^2} + \frac{y^2}{(\xi R_2)^2} = 1 .$$

These lines are “parallel” to the ellipsoidal surface.

We define the deformation parameter ϵ

$$\epsilon = \frac{\langle x^2 \rangle - \langle y^2 \rangle}{\langle x^2 \rangle + \langle y^2 \rangle}$$

where e.g.,

$$\langle x^2 \rangle = \frac{1}{N} \int d\mathbf{r} x^2 \Psi(\mathbf{r})$$

For the sharp surface ellipsoid above,

$$\alpha = \frac{m_4}{\hbar} \epsilon \omega \quad (A.1)$$

This relationship is not general but can be used as a guide for our more general approach. Let us now discuss the angular momentum and moment of inertia of the irrotational fluid droplet. Recalling that

$$L_z = -i \hbar \left(x \frac{\partial}{\partial y} - y \frac{\partial}{\partial x} \right)$$

if we write

$$\Psi(\mathbf{r}) = \Phi(\mathbf{r}) e^{i\alpha xy}$$

with $\Phi(\mathbf{r})$ a real function,

$$\langle L_z \rangle = \hbar \alpha \int d\mathbf{r} (x^2 - y^2) \Phi^2(\mathbf{r})$$

If Eq. (A.1) holds,

$$\begin{aligned} \langle L_z \rangle &= \epsilon m_4 N [\langle x^2 \rangle - \langle y^2 \rangle] \omega \\ &= m_4 N \left(\frac{[\langle x^2 \rangle - \langle y^2 \rangle]^2}{\langle x^2 \rangle + \langle y^2 \rangle} \right) \omega \equiv I_{irr} \omega \end{aligned} \quad (\text{A.2})$$

where

$$I_{irr} = m_4 N \left(\frac{[\langle x^2 \rangle - \langle y^2 \rangle]^2}{\langle x^2 \rangle + \langle y^2 \rangle} \right)$$

is the irrotational moment of inertia. For a rigid solid,

$$I_{rig} = m_4 \int d\mathbf{r} (x^2 + y^2) \Phi^2(\mathbf{r}) = m_4 N [\langle x^2 \rangle + \langle y^2 \rangle]$$

Hence,

$$\frac{I_{irr}}{I_{rig}} = \left[\frac{\langle x^2 \rangle - \langle y^2 \rangle}{\langle x^2 \rangle + \langle y^2 \rangle} \right]^2 \rightarrow 0 \quad \text{if } \epsilon \rightarrow 0$$

Finally, we discuss the kinetic energy of the droplet

$$E_{kin} = \frac{\hbar^2}{2m_4} \int d\mathbf{r} |\nabla \Psi(\mathbf{r})|^2$$

From the above $\Psi(\mathbf{r})$,

$$\begin{aligned} E_{kin} &= \frac{\hbar^2}{2m_4} \int d\mathbf{r} |\nabla \Phi(\mathbf{r})|^2 \\ &+ \frac{\hbar^2}{2m_4} \alpha^2 \int d\mathbf{r} (x^2 + y^2) \Phi^2(\mathbf{r}) = E_{intr} + E_{coll} \end{aligned}$$

where the first term is the “intrinsic” kinetic energy and the second term arises from the irrotational velocity field

$$\begin{aligned} E_{coll} &= \frac{\hbar^2}{2m_4} \alpha^2 \int d\mathbf{r} (x^2 + y^2) \Phi^2(\mathbf{r}) = \\ &\frac{1}{2} \left\{ m_4 \epsilon^2 \int d\mathbf{r} (x^2 + y^2) \Phi^2(\mathbf{r}) \right\} \omega^2 = \frac{1}{2} I_{irr} \omega^2 \end{aligned}$$

These expressions may be used to obtain some estimates from the actual DFT calculations. For a ${}^4\text{He}_{1000}$ droplet and $\omega=0.10 \text{ K}/\hbar$ we have obtained $\langle x^2 \rangle = 100.82 \text{ \AA}^2$ and $\langle y^2 \rangle = 101.82 \text{ \AA}^2$; hence, $\epsilon \sim -1/200$. Since $\hbar^2/m_4 = 12.12 \text{ K \AA}^2$, from Eq. (A.1) one has $\alpha \sim -4.2 \times 10^{-5} \text{ \AA}^{-2}$. From Eq. (A.2) we obtain $\langle L_z \rangle \sim 4 \times 10^{-2} \hbar$.

In a Bose-Einstein condensate the deformation ϵ is a control parameter that can be set to a very large value (close to unity). For a self-bound ${}^4\text{He}$ droplet deformation comes from “rotation” itself and it turns out to be minute even for angular frequencies close to the critical frequency for one-vortex nucleation; the conclusion is that the droplet “does not rotate”; in other words, it is unable to store an appreciable amount of angular momentum before vortex nucleation.

Bibliography

- [1] P. Kapitza, *Nature* **141**, 74 (1938), URL <http://dx.doi.org/10.1038/141074a0>.
- [2] B. Rollin and F. Simon, *Physica* **6**, 219 (1939), ISSN 0031-8914, URL <http://www.sciencedirect.com/science/article/pii/S0031891439800131>.
- [3] W. Keesom and M. A. Keesom, *Physica* **3**, 359 (1936), ISSN 0031-8914, URL <http://www.sciencedirect.com/science/article/pii/S0031891436803127>.
- [4] L. Tisza, *Comptes rendus hebdomadaires des séances de l'Académie des sciences* **207**, 1035 (1938), URL <http://gallica.bnf.fr/ark:/12148/bpt6k31590/f1035.item>.
- [5] L. Tisza, *Comptes rendus hebdomadaires des séances de l'Académie des sciences* **207**, 1186 (1938), URL <http://gallica.bnf.fr/ark:/12148/bpt6k31590/f1186.item>.
- [6] L. Tisza, *J. Phys. Radium* **1**, 164 (1940), URL <https://doi.org/10.1051/jphysrad:0194000105016400>.
- [7] L. Tisza, *J. Phys. Radium* **1**, 350 (1940), URL <https://doi.org/10.1051/jphysrad:0194000108035000>.
- [8] P. Lebrun, *Cryogenics* **34**, 1 (1994), ISSN 0011-2275, fifteenth International Cryogenic Engineering Conference, URL <http://www.sciencedirect.com/science/article/pii/S0011227505800037>.
- [9] W. Keesom and M. A. Keesom, *KNAW, Proceedings* **35**, 736 (1932), URL <http://www.dwc.knaw.nl/DL/publications/PU00016277.pdf>.
- [10] R. J. Donnelly, *Physics Today* **62**, 34 (2009), <https://doi.org/10.1063/1.3248499>, URL <https://doi.org/10.1063/1.3248499>.

- [11] H. Kamerlingh Onnes, KNAW, Proceedings **10**, 744 (1908), URL <http://www.dwc.knaw.nl/toegangen/digital-library-knaw/?pagetype=publDetail&pId=PU00013699>.
- [12] H. Kamerlingh Onnes, KNAW, Proceedings **11**, 168 (1909), URL <http://www.dwc.knaw.nl/toegangen/digital-library-knaw/?pagetype=publDetail&pId=PU00013525>.
- [13] P. J. McLennan, H. Smith, and J. Wilhelm, The London, Edinburgh, and Dublin Philosophical Magazine and Journal of Science **14**, 161 (1932), <https://doi.org/10.1080/14786443209462044>, URL <https://doi.org/10.1080/14786443209462044>.
- [14] E. F. Burton, Nature **135**, 265 (1935), URL <http://dx.doi.org/10.1038/135265a0>.
- [15] M. v. Laue, F. London, and H. London, Zeitschrift für Physik **96**, 359 (1935), ISSN 0044-3328, URL <https://doi.org/10.1007/BF01343868>.
- [16] F. Simon, Nature **133**, 529 (1934), URL <http://dx.doi.org/10.1038/133529a0>.
- [17] F. London, Proceedings of the Royal Society of London A: Mathematical, Physical and Engineering Sciences **153**, 576 (1936), ISSN 0080-4630, <http://rspa.royalsocietypublishing.org/content/153/880/576.full.pdf>, URL <http://rspa.royalsocietypublishing.org/content/153/880/576>.
- [18] J. F. Allen, R. Peierls, and M. Zaki Uddin, Nature **140**, 62 (1937), URL <http://dx.doi.org/10.1038/140062a0>.
- [19] J. F. Allen and A. D. Misener, Nature **141**, 75 (1938), URL <http://dx.doi.org/10.1038/141075a0>.
- [20] F. London, Nature **141**, 643 (1938), URL <http://dx.doi.org/10.1038/141643a0>.
- [21] L. Tisza, Nature **141**, 913 (1938), URL <http://dx.doi.org/10.1038/141913a0>.
- [22] L. Landau, Phys. Rev. **60**, 356 (1941), URL <https://link.aps.org/doi/10.1103/PhysRev.60.356>.

- [23] L. Landau, Phys. Rev. **75**, 884 (1949), URL <https://link.aps.org/doi/10.1103/PhysRev.75.884>.
- [24] N. N. Bogolyubov, J. Phys. (USSR) **11**, 23 (1947), [Izv. Akad. Nauk Ser. Fiz. 11, 77 (1947)], URL <https://ufn.ru/ru/articles/1967/11/o/>.
- [25] E. A. Cornell and C. E. Wieman, Rev. Mod. Phys. **74**, 875 (2002), URL <https://link.aps.org/doi/10.1103/RevModPhys.74.875>.
- [26] W. Ketterle, Rev. Mod. Phys. **74**, 1131 (2002), URL <https://link.aps.org/doi/10.1103/RevModPhys.74.1131>.
- [27] D. Mateo, M. Barranco, and J. Navarro, Phys. Rev. B **82**, 134529 (2010).
- [28] R. J. Donnelly, J. A. Donnelly, and R. N. Hills, J. Low Temp. Phys. **44**, 471 (1981).
- [29] F. Ancilotto, P. B. Lerner, and M. W. Cole, J. Low Temp. Phys. **101**, 1123 (1995).
- [30] E. Krotscheck and J. Navarro, eds., *Microscopic approaches to quantum liquids in confined geometries*, vol. 4 of *Series on Advances in Quantum Many-Body Theory* (World Scientific, Singapore, 2002).
- [31] M. P. de Lara-Castells, G. Delgado-Barrio, P. Villarreal, and A. O. Mitrushchenkov, J. Chem. Phys. **125**, 221101 (2006).
- [32] M. P. de Lara-Castells, N. F. Aguirre, P. Villarreal, G. Delgado-Barrio, and A. O. Mitrushchenkov, J. Chem. Phys. **132**, 194313 (2010).
- [33] N. F. Aguirre, P. Villarreal, G. Delgado-Barrio, A. O. Mitrushchenkov, and M. P. de Lara-Castells, Phys. Chem. Chem. Phys. **15**, 10126 (2013).
- [34] S. Stringari and J. Treiner, Phys. Rev. B **36**, 8369 (1987).
- [35] S. Stringari and J. Treiner, J. Chem. Phys. **87**, 5021 (1987).
- [36] F. Dalfovo, A. Lastri, L. Pricaupenko, S. Stringari, and J. Treiner, Phys. Rev. B **52**, 1193 (1995).
- [37] P. Hohenberg and W. Kohn, Phys. Rev. **136**, B864 (1964), URL <https://link.aps.org/doi/10.1103/PhysRev.136.B864>.
- [38] W. Kohn and L. J. Sham, Phys. Rev. **140**, A1133 (1965), URL <https://link.aps.org/doi/10.1103/PhysRev.140.A1133>.

- [39] E. Runge and E. K. U. Gross, Phys. Rev. Lett. **52**, 997 (1984).
- [40] F. Dalfovo, A. Lastri, L. Pricaupenko, S. Stringari, and J. Treiner, Phys. Rev. B **52**, 1193 (1995), URL <https://link.aps.org/doi/10.1103/PhysRevB.52.1193>.
- [41] Z. J. Jakubek, Q. Hui, and M. Takami, Phys. Rev. Lett. **79**, 629 (1997).
- [42] A. Nakayama and K. Yamashita, J. Chem. Phys. **114**, 780 (2001).
- [43] M. Barranco, F. Coppens, N. Halberstadt, A. Hernando, A. Leal, D. Mateo, R. Mayol, and M. Pi ((2017)), <https://github.com/bcngls2016/DFT-Guide/blob/master/dft-guide.pdf>.
- [44] A. Griffin and S. Stringari, Phys. Rev. Lett. **76**, 259 (1996), URL <https://link.aps.org/doi/10.1103/PhysRevLett.76.259>.
- [45] P. Carrick, ed., *Theoretical Performance of Atomic and Molecular HEDM Additives to Solid H₂*, p. 412 (Proceedings of the High Energy Density Matter (HEDM) Contractor's Conference, Woods Hole, MA.; Edwards Air Force Base, CA, 1993), URL <http://www.dtic.mil/docs/citations/ADA274452>.
- [46] C. P. Schulz, P. Claas, and F. Stienkemeier, Phys. Rev. Lett. **87**, 153401 (2001), URL <https://link.aps.org/doi/10.1103/PhysRevLett.87.153401>.
- [47] J. Reho, J. Higgins, K. K. Lehmann, and G. Scoles, The Journal of Chemical Physics **113**, 9694 (2000), <https://doi.org/10.1063/1.1321034>, URL <https://doi.org/10.1063/1.1321034>.
- [48] J. Reho, J. Higgins, C. Callegari, K. K. Lehmann, and G. Scoles, The Journal of Chemical Physics **113**, 9686 (2000), <https://doi.org/10.1063/1.1321033>, URL <https://doi.org/10.1063/1.1321033>.
- [49] M. Martinez, Master's thesis, Université Toulouse III Paul Sabatier (2017), URL <https://github.com/bcngls2016/M2Report-MMartinez/blob/master/report/report.pdf>.
- [50] A. Scheidemann, J. P. Toennies, and J. A. Northby, Phys. Rev. Lett. **64**, 1899 (1990).
- [51] J. P. Toennies and A. F. Vilesov, Angew. Chem. Phys. **43**, 2622 (2004).

- [52] J. Harms, J. P. Toennies, and F. Dalfovo, Phys. Rev. B **58**, 3341 (1998).
- [53] J. Harms, J. P. Toennies, M. Barranco, and M. Pi, Phys. Rev. B **63**, 184513 (2001).
- [54] E. Krotscheck and R. E. Zillich, Eur. Phys. J. D **43**, 113 (2007).
- [55] E. Krotscheck and R. E. Zillich, Phys. Rev. B **77**, 094507 (2008).
- [56] D. Eichenauer, A. Scheidemann, and J. P. Toennies, Z. Phys. D **8**, 295 (1988).
- [57] L. F. Gomez, K. R. Ferguson, J. P. Cryan, C. Bacellar, R. M. P. Tanyag, C. Jones, S. Schorb, D. Anielski, A. Belkacem, C. Bernando, et al., Science **345**, 906 (2014).
- [58] C. F. Jones, C. Bernardo, R. M. P. Tanyag, C. Bacellar, K. R. Ferguson, L. F. Gomez, D. Anielski, A. Belkacem, R. Boll, J. Bozek, et al., Phys. Rev. B **93**, 180510(R) (2016).
- [59] F. Ancilotto, M. Pi, and M. Barranco, Phys. Rev. B **90**, 174512 (2014).
- [60] F. Ancilotto, M. Pi, and M. Barranco, Phys. Rev. B **91**, 100503(R) (2015).
- [61] L. F. Gomez, E. Loginov, R. Sliter, and A. F. Vilesov, J. Chem. Phys. **135**, 154201 (2011).
- [62] A. Leal, X. Zhang, M. Barranco, F. Cargnoni, A. Hernando, D. Mateo, M. Mella, M. Drabbels, and M. Pi, J. Chem. Phys. **144**, 094302 (2016).
- [63] D. Mateo, A. Leal, A. Hernando, M. Barranco, M. Pi, F. Cargnoni, M. Mella, X. Zhang, and M. Drabbels, J. Chem. Phys. **140**, 131101 (2014).
- [64] F. Stienkemeier, J. Higgins, C. Callegari, S. I. Kanorsky, W. E. Ernst, and G. Scoles, Z. Phys. D **38**, 253 (1996).
- [65] A. Hernando, R. Mayol, M. Pi, M. Barranco, F. Ancilotto, O. Bünermann, and F. Stienkemeier, J. Phys. Chem. A **111**, 7303 (2007).
- [66] F. Stienkemeier and K. K. Lehmann, J. Phys. B **39**, R127 (2006).
- [67] J. Tiggesbäumker and F. Stienkemeier, Phys. Chem. Chem. Phys. **9**, 4748 (2007).

- [68] C. Callegari and W. E. Ernst, in *Handbook of High Resolution Spectroscopy* (Wiley, New York, 2011), vol. 3, p. 1551.
- [69] M. Mudrich and F. Stienkemeier, *Int. Rev. Phys. Chem.* **33**, 301 (2014).
- [70] M. Lewerenz, B. Schilling, and J. P. Toennies, *J. Chem. Phys.* **102**, 8191 (1995).
- [71] R. M. P. Tanyag, C. F. Jones, C. Bernando, S. M. O. O'Connell, D. Verma, and A. F. Vilesov, *Experiments with large superfluid helium nanodroplets* (Royal Society of Chemistry, Cambridge, UK, 2017), chap. 8, (to be published).
- [72] L. F. Gomez, E. Loginov, and A. F. Vilesov, *Phys. Rev. Lett.* **108**, 155302 (2012).
- [73] E. Latimer, D. Spence, C. Feng, A. Boatwright, A. M. Ellis, and S. Yang, *Nano Lett.* **14**, 2902 (2014).
- [74] P. Thaler, A. Volk, F. Lackner, J. Steurer, D. Knez, W. Grogger, F. Hofer, and W. E. Ernst, *Phys. Rev. B* **90**, 155442 (2014).
- [75] A. Leal, D. Mateo, A. Hernando, M. Pi, and M. Barranco, *Phys. Chem. Chem. Phys.* **16**, 23206 (2014).
- [76] A. Vilà, M. González, and R. Mayol, *Phys. Chem. Chem. Phys.* **18**, 2006 (2016).
- [77] A. Hernando, M. Barranco, M. Pi, E. Loginov, M. Langlet, and M. Drabbels, *Phys. Chem. Chem. Phys.* **14**, 3996 (2012).
- [78] F. Coppens, A. Leal, M. Barranco, N. Halberstadt, and M. Pi, *J. Low Temp. Phys.* (2016).
- [79] A. Leal, D. Mateo, A. Hernando, M. Pi, M. Barranco, A. Ponti, F. Cargnoni, and M. Drabbels, *Phys. Rev. B* **90**, 224518 (2014).
- [80] M. Pi, R. Mayol, A. Hernando, M. Barranco, and F. Ancilotto, *J. Chem. Phys.* **126**, 244502 (2007).
- [81] F. Dalfovo, R. Mayol, M. Pi, and M. Barranco, *Phys. Rev. Lett.* **85**, 1028 (2000).
- [82] F. Ancilotto, M. Barranco, F. Caupin, R. Mayol, and M. Pi, *Phys. Rev. B* **72**, 214522 (2005).

- [83] G. A. Williams and R. E. Packard, Phys. Rev. Lett. **33**, 280 (1974).
- [84] C. Bernando, R. Mayro, P. Tanyag, C. Jones, C. Bacellar, M. Bucher, K. R. Ferguson, D. Rupp, M. P. Ziemkiewicz, L. F. Gomez, et al., Phys. Rev. B **95**, 064510 (2017).
- [85] I. A. Pshenichnyuk and N. G. Berloff, Phys. Rev. B **94**, 184505 (2016).